

Advances in Intense Femtosecond Laser Filamentation in Air¹

S. L. Chin^a, T.-J. Wang^a, C. Marceau^a, J. Wu^b, J. S. Liu^c, O. Kosareva^{d,*}, N. Panov^d,
Y. P. Chen^a, J.-F. Daigle^a, S. Yuan^a, A. Azarm^a, W. W. Liu^e, T. Seideman^f,
H. P. Zeng^b, M. Richardson^g, R. Li^c, and Z. Z. Xu^c

^a Center for Optics, Photonics and Laser (COPL), Laval University, Quebec City, Qc G1V 0A6, Canada

^b State Key Laboratory of Precision Spectroscopy, East China Normal University, Shanghai 200062, China

^c Shanghai Institute of Optics and Fine Mechanics (SIOM), Chinese Academy of Sciences, Jiading, Shanghai, China

^d International Laser Center, Dept. of Physics, Moscow State University, Moscow, Russia

^e Institute of Modern Optics, Nankai University, Tianjin, China

^f Department of Chemistry, Northwestern University, 2145 Sheridan Road, Evanston, Illinois 60208-3113, USA

^g Townes Laser Institute, CREOL College of Optics and Photonics, University of Central Florida, Orlando, FL, USA

*e-mail: kosareva@physics.msu.ru

Received April 12, 2011; in final form, April 26, 2011; published online September 2, 2011

Abstract—This is a review of some recent development in femtosecond filamentation science with emphasis on our collective work. Previously reviewed work in the field will not be discussed. We thus start with a very brief description of the fundamental physics of single filamentation of powerful femtosecond laser pulses in air. Intensity clamping is emphasized. One consequence is that the peak intensity inside one or more filaments would not increase significantly even if one focuses the pulse at very high peak power even up to the peta-watt level. Another is that the clamped intensity is independent of pressure. One interesting outcome of the high intensity inside a filament is filament fusion which comes from the nonlinear change of index of refraction inside the filament leading to cross beam focusing. Because of the high intensity inside the filament, one can envisage nonlinear phenomena taking place inside a filament such as a new type of Raman red shift and the generation of very broad band supercontinuum into the infrared through four-wave-mixing. This is what we call by filamentation nonlinear optics. It includes also terahertz generation from inside the filament. The latter is discussed separately because of its special importance to those working in the field of safety and security in recent years. When the filamenting pulse is linearly polarized, the isotropic nature of air becomes birefringent both electronically (instantaneous) and through molecular wave packet rotation and revival (delayed). Such birefringence is discussed in detailed. Because, in principle, a filament can be projected to a long distance in air, applications to pollution measurement as well as other atmospheric science could be earned out. We call this filamentation atmospheric science. Thus, the following subjects are discussed briefly, namely, lightning control, rain making, remote measurement of electric field, microwave guidance and remote sensing of pollutants. A discussion on the higher order Kerr effect on the physics of filamentation is also given. This is a new hot subject of current debate. This review ends on giving our view of the prospect of progress of this field of filamentation in the future. We believe it hinges upon the development of the laser technology based upon the physical understanding of filamentation and on the reduction in price of the laser system.

DOI: 10.1134/S1054660X11190054

CONTENT

Section	page
1. Introduction	2
2. The physics of filamentation	3
3. Limitation to reaching very high intensity inside a filament zone	7
4. Nonlinear interaction of intense femtosecond filaments in air	10
5. Filamentation nonlinear optics: Raman spectral shift, four-wave-mixing and supercontinuum	20
6. Terahertz pulse generation in filaments	22
7. Birefringence inside a filament in air.	29
8. Molecular alignment in a filament and revival	30
9. Filamentation atmospheric science	40
10. Non-ionizing filament and higher order Kerr contribution	44
11. Challenges ahead	47

¹ The article is published in the original.

List of abbreviations/special terms

4WM: four-wave-mixing
 CEP: carrier envelope phase
 CPA: chirped pulse amplification
 CPM: cross-phase-modulation
 EOS: electro-optical sampling
 FIB: femtosecond laser induced breakdown spectroscopy
 FIR: far infrared
 fs: femtosecond (10^{-15} s)
 FW: fundamental wave
 GVD: group velocity dispersion
 GW: gigawatt (10^9 W)
 I_c : clamped intensity
 ICCD: intensified CCD detector
 LIBS: laser induced breakdown spectroscopy
 LIDAR: light detection and ranging
 MW: megawatt (10^6 W)
 NIR: near infrared
 ns: nanosecond (10^{-9} s)
 P_c : critical power for self-focusing
 ps: picoseconds (10^{-12} s)
 PW: petawatt (10^{15} W)
 SC: supercontinuum
 SH: second harmonic
 SHW: second harmonic wave
 SPM: self-phase-modulation
 Teramobile: terawatt laser in a mobile unit, a French-German consortium.
 TH: third harmonic
 THG: third harmonic generation
 THz: terahertz (10^{12} Hz)
 TW: terawatt (10^{12} W)
 UV: ultraviolet
 XPM: cross phase modulation
 X-Kerr effect: cross Kerr effect

1. INTRODUCTION

Filamentation of an intense laser pulse is a phenomenon arising from self-focusing. The latter was discovered in the mid-sixties [1, 2] following the invention of the laser. Since then, it was studied extensively for a decade or so using nanosecond laser pulses [3]. In those years, nanosecond pulses were considered to be very short, but compared to modern-day femtosecond (10^{-15} s) and attosecond (10^{-18} s) time scale, nanosecond is now considered to be very long. It is precisely because a nanosecond laser pulse is so long compared to the interaction time scale with matters that optical breakdown occurs and masks the clear and easy observation of filamentation for about twenty

years. In 1995, in the Center for Ultrafast Optical Science (CUOS) of University of Michigan under the leadership of Gerard Mourou, an “accident” took place in the laboratory. In the beam path of the femtosecond Ti-sapphire laser pulses, damaged spots on mirrors led to the first manifestation of filamentation by an intense femtosecond laser pulse [4]. Since then, there have been a lot of activities in this new-found area of frontier optical research. The fundamentals of filamentation and some of its applications are by now well-known. Several review papers and books [5–11] have already been published. It is not the intention of the current paper to review everything in the field. Instead, we shall focus on some recent experimental progress with emphasis on our collective work and discuss some challenges in the field. Thus, many interesting subjects which have been reviewed are not discussed. One example is x -wave [12, 13] where an excellent review has been given by Couairon et al. [14].

We shall thus only give a very brief description in Section 2 of the fundamental physics of single filamentation, intensity clamping, self-pulse compression, multiple filamentation, filaments competition and the independence of the clamped intensity on air (gas) pressure. One important consequence of intensity clamping is immediately discussed in detail in Section 3. It pertains to the question of significantly increasing the intensity inside a bundle of filaments in air using, for example, the highest power available (petawatt (PW) level) lasers. A natural physical idea is to fuse together these filaments in the focal region of an externally focusing element. This idea is tested in experiments and simulations. Common sense physics would predict that through mutual interference of the many fusing filaments, the intensity would be greatly increased. Intensity clamping simply sets a limit. So far, experiments in air show that the increase is less than 50% of the clamped intensity of a single filament using up to 70 TW pulses.

Although filament fusion cannot give rise to very high intensity, it still has a lot of new physical consequences. So, following Section 3, we present recent advances in filament fusion and interaction in Section 4. Filament fusion and interaction have been studied extensively in the past few years. We shall thus discuss this problem in more detail. This section includes new advances in harmonic generation which partially belong to the next section (5) on the advances in filamentation nonlinear optics. Section 5 includes a new type of Raman red shift inside the filament and the generation of very broad band supercontinuum into the infrared through four-wave-mixing. One branch of filamentation nonlinear optics, namely, THz generation from inside the filament, is discussed separately in Section 6 because of its special importance to those working in the field of safety and security in recent years.

In the high intensity zone of the filament of a linearly polarized pump pulse, the isotropic air medium becomes birefringent. Section 7 discusses the electronic birefringence effect in air induced by the pump and sampled by a linearly polarized probe pulse through cross phase modulation. The probe pulse becomes elliptically polarized and rotates as it propagates through the filament.

Since air is a molecular medium, the high intensity inside the filament will induce yet another type of birefringence, namely, delayed alignment of molecular wave packets of nitrogen and oxygen molecules which later de-phase and revive rotationally over a long time (more than 100 ps), long after the pump pulse is gone. The physics of this molecular phenomenon is analyzed by a probe pulse and is discussed in Section 8. Although intense laser induced molecular alignment, de-phasing and rotational revival were known for a number of years, we believe that the general readers interested in filamentation might not be very familiar with the phenomenon. We thus take an extra effort to describe in more detail the physics of laser induced molecular alignment before presenting the phenomenon of filament induced alignment and revival.

Some applications in air are discussed in Section 9 which we call filamentation atmospheric science. They are lightning control, rain making and remote measurement of electric field, microwave guidance and remote sensing. A renewed debate of non-ionizing filamentation has arisen in the past year. The higher order terms of the nonlinear Kerr index were measured and were found to be very large and effectively negative. Simulation suggested that even without the plasma, these higher order Kerr terms would be sufficient to balance the initial Kerr self-focusing. Plasma generation is then considered to be a by-product. However, this point of view is not unanimous. There are questions and arguments about this finding. We try to confront this problem in Section 10.

This review ends in Section 11 in which we give our view on the prospect of progress of this field of filamentation in the future. We believe it hinges upon the development of the laser technology which should give a much better beam quality to minimize multiple filaments' competition. Commercialization of some of the practical applications depends very much on the reduction in price of the laser system.

At this point, we would like to mention that a full bibliography on filamentation has been nicely documented by Stelios Tzortzakis of the Institute of Electronic Structure and Laser (IESL), Foundation for Research and Technology—Hellas (FORTH), Heraklion, Greece in the following freely accessible website: <http://www.filmamentation.org/Publications.aspx/>. Those who need to have more references should consult this website.

2. THE PHYSICS OF FILAMENTATION

In this section, a brief qualitative description of the physical mechanism of generating filaments in air will be given in Subsections 2.1 to 2.5, from single filamentation to multiple filaments and their competition for energy from the reservoir. For details, the readers are referred to references [5–11]. This is followed by a description of self-pulse compression (Subsection 2.6) and the independence of intensity clamping on pressure (Subsection 2.7). This latter phenomenon might have an important consequence of opening up a way to increase the energy content inside a filament at high altitude.

2.1. Single Filamentation

The first question one would ask would be what could have been unknown or still hidden in self-focusing in 1995 when the first sign of filamentation was observed? The answer is “nothing” except for the tool, the femtosecond (fs) laser pulses. In particular, self-focusing in air needs to have a laser peak power higher than the high critical power so that the pulse will collapse. In air, the critical power for self-focusing is of the order of a few gigawatts (GW). In the olden days, using nanosecond laser pulses, the threshold for laser induced air-breakdown was at a much lower power, a few megawatts (MW) followed by focusing by a relatively short focal length lens (about 10 cm). Using nanosecond pulses, laser induced breakdown is due to the “three-step-processes” all occurring in the laser field; namely, multiphoton ionization of impurities in the gas, inverse Bremsstrahlung and electron cascade/avalanche ionization [15]. The latter two are collisional processes and they take time (many ps to ns time scale) to accomplish the work. Using nanosecond pulses, even if the peak power is higher than the critical power for self-focusing, the breakdown threshold is reached at the rising part of the pulse before GW level is reached. Thus, a plasma in the focal volume is created that further absorbs and reflects the laser radiation. Self-focusing is thus prohibited. With the use of the fs laser pulse (10 to a few hundred fs), the pulse duration is even shorter than the time it takes for a single inverse Bremsstrahlung process to occur (acceleration of a free electron in the laser field while colliding with another heavy particle (ion or atom or molecule). The mean free time of an electron in one atmospheric air is of the order of 1 picosecond (ps). Thus, even at a peak power higher than the critical power for self-focusing, breakdown would not occur. This leaves the “playground” open to other processes.

From now on, we shall assume that a Ti-sapphire laser pulse is used because it is currently the most popular high power fs laser used in almost all the intense fs laser laboratories in the world. Most of these systems are based upon the CPA (chirped pulse amplification) technique [16]. Assume that the peak power of the

laser is many times higher than the critical power for self-focusing, P_c [3]

$$P_c = \frac{3.77\lambda^2}{8\pi n_0 n_2}. \quad (1)$$

Its duration is of the order of a few tens of fs to a few hundred fs at a central wavelength of 800 nm. The laser pulse will undergo the so-called slice-by-slice self-focusing process. Each slice has an intensity distribution, say Gaussian; i.e., high intensity at the center and low at the edge. The higher index of refraction at the center of the slice due to the Kerr nonlinearity is $(n_0 + n_2 I)$, where n_0 is the linear index of refraction, n_2 , the nonlinear Kerr coefficient, and I , the intensity. The nonlinear index of refraction, $n_2 I$, is positive in most normal transparent medium. The index of refraction at the edge of the slice is the linear one, n_0 . This intensity distribution would lead to self-focusing because the central part will propagate slower than the edge. The thickness of each slice could be conceptually considered to be at least $c\tau$, where c is the speed of light and τ , the period of the light wave. This is because we consider the distribution of intensity across each slice while intensity is defined as the Poynting vector averaged over at least one cycle of oscillation of the field, τ . When the power of a slice is higher than P_c , the self-focusing will overcome natural linear diffraction and collapse resulting in tunnel/multiphoton ionization of air molecules. The position at which the collapse occurs is given by [3]

$$z_f = \frac{0.367ka^2}{\left\{ \left[\left(\frac{P}{P_{\text{crit}}} \right)^{1/2} - 0.852 \right]^2 - 0.0219 \right\}^{1/2}}, \quad (2)$$

where k and a_0 are the wave number and the radius of the beam profile at $1/e^2$ level of intensity, respectively, and P is the peak power. Successive slices at the front part of the pulse will self-focus at different position giving rise to the perception of a filament. Each slice, after the collapse and ionization, will be de-focused by the self-created plasma into the background reservoir [5, 10, 17]. The background reservoir plays an important role in supporting the continuous generation of the self-foci slice after slice. Conceptually, a filament is the perception of a series of self-foci. Each self-focus comes from the collapse of one slice of the reservoir of the pulse. A filament does not correspond to a ‘‘light bullet’’ piercing through the medium.

Interestingly, Eq. (2) which was derived for a long pulse or a continuous wave laser beam works also for femtosecond laser pulses [5]. The peak power is independent of the chirp in the pulse; i.e., it could be that of a chirped pulse or a transform limited pulse. Eq. (2.1) can be coupled to the following ‘‘Talenov equation’’ when a focusing/defocusing element with focal length f is used

$$1/z_f + 1/f = 1/z_f'. \quad (3)$$

Here, z_f' is the new self focusing distance. Based on this principle, the self-focusing distance of intense laser pulses in the atmosphere can be experimentally controlled with a simple double-lens setup [18].

In practice, the short laser pulse will suffer group velocity dispersion (GVD) because of the large bandwidth of the fs laser pulse. That is to say, as the pulse propagates in an optical medium it will become longer so that the peak power becomes lower. This will have an impact on the collapse of the pulse at the self-focus. Slightly higher power than P_c is necessary to overcome GVD as well as diffraction so as to have a collapse.

2.2. Intensity Clamping

Equations (2) and (3) give rise to the confidence that z_f' , (and z_f) could be varied at will to any long distance. Let's see how it could be done. We look at z_f first (Eq. (2)). Given a certain beam radius a_0 , one can change the peak power P to change the self-focusing position z_f . This could be easily done by changing the chirp of the pulse, both positively and negatively [5]. The lengthening of the pulse by the chirp would decrease the peak power P hence lengthening the self-focusing position z_f . One can also change the self-focusing position by increasing the beam radius a_0 according to Eq. (2). These manipulations would result in moving the filament to a longer distance. The addition of a focusing element (Eq. (3)) will further control the self-focusing distance. Thus, in principle, any distance up to infinity is possible [10].

Moreover, common sense would say that if one could keep increasing the laser pulse's energy, the intensity in the self-focus would be increased accordingly. Since in principle there is no limit to increasing the laser pulse energy, one would expect that a very high intensity could be delivered onto a remote target generating even a relativistic interaction. Such optimism could lead to disastrous consequences if one were to immediately jump this conclusion and invest resources, financial and otherwise, into an ambitious research program. That ever increasing intensity does not happen is because of intensity clamping.

Equations (2) and (3) predict only the position of the mathematical collapse of the pulse. Such a collapse leading to a singularity does not happen in reality. This is because, as the self-focal size becomes smaller and smaller, the intensity becomes higher and higher. Soon, multiphoton/tunnel ionization takes place (with femtosecond laser pulses, there is no collisional ionization [15]) resulting in a defocusing plasma. It is exactly the plasma and not the higher-order Kerr nonlinearity that stops self-focusing collapse in femtosecond laser filamentation in air [19]. The local intensity is thus clamped at this balancing

point of self-focusing and self-defocusing by the self-generated plasma. The clamped intensity of a free propagating beam (no external focusing) is of the order of $5 \times 10^{13} \text{ W/cm}^2$ [20–22]. This phenomenon of intensity clamping is very profound and will impact many new phenomena and applications.

Recently, a theoretical work has studied the subcycle spatiotemporal dynamics of the laser transformation during filamentation by retaining the full electric-field of the laser pulse. The result predicts a sub-fs intensity spike, having intensity exceeding the clamping intensity by a factor of 3, can last for a short propagation distance in the filamentation process [23].

2.3. Self-Spatial Filtering

Normally, in many experiments, the laser pulse contains a lot of spatial modes. The fundamental mode having the smallest diameter would self-focus and reach the ionization stage first according to the dependence of z_f on the diameter $2a_0$ in Eq. (2); i.e., z_f is shortest. Higher order modes having larger diameters would have a longer z_f during their individual self-focusing process. Before they reach the point of high intensity ionization, they will have to pass through the plasma zone created by the fundamental mode and be diffracted out into the reservoir. Thus only the fundamental spatial mode would keep on self-focusing into a series of self-foci which constitute the perfectly round filament core. We call this phenomenon self-mode-cleaning or self-spatial filtering [10, 24, and references therein]. The self-filtered laser pulse by filamentation can be applied to improve the outcome of nonlinear optical process, such as the four-wave mixing [25] and second harmonic generation [26].

2.4. Multiple Filamentation

So what would happen to the intensity inside the filament if we keep increasing the energy or peak power in the pulse? Let's say we start at a power level that gives rise to one filament. We now increase the power/energy of the pulse. Intensity clamping would stop any further increase in intensity. The extra energy coming into the filament zone would be "spilled over" resulting in a filament with a larger diameter [27]. However, further increase of the energy would lead to multiple filamentation in practice because all practical high power fs Ti-sapphire laser pulses do not have a homogeneous beam pattern. Hot zones are plentiful across the beam cross section. Each hot zone will self-focus into a filament if the intensity and power are high enough. Each of the multiple filaments will have a core intensity clamped down to that of a single filament. Thus, no increase of intensity is possible with multiple filamentation.

2.5. Multiple Filaments Competition

With multiple filamentation comes an unexpected phenomenon called filament competition [10]. This arises from the basic mechanism of a single filament formation; i.e., slice-by-slice self-focusing. Each self-focal spot comes from the surrounding energy reservoir. For each slice that self-focuses toward the central axis, it is as if energy is sucked from the reservoir towards the center and then, due to plasma generation, diverges out into the reservoir. Thus, if there are two or more well separated hot zones in the pulse each having a tendency to self-focus, they will each suck energy from the same reservoir thus competing for energy. Depending on the relative distances among the hot zones, sometimes one or two very strong (larger in diameter) probably fused filaments occur. However, most of the time, in a currently available TW level laser pulse, there are many hot zones. If we let a large diameter TW level beam to propagate freely without using a lens, the competition among the various filamenting hot zones results in no winner; i.e., very few filaments occur [28–32]. But if the beam diameter of the same TW level beam is reduced by a few times, filament cooperation takes place. That is to say, along the propagation direction, consistently strong filaments are generated [29–32].

Physically, these are due to the interference between neighboring filaments and the reservoir. Assume a free propagating fs pulse with a plane wave front and with two hot zones each having a Gaussian intensity distribution across the hot front. Let's say each hot zone has a local peak power higher than the critical power for self-focusing. Thus each hot zone will start to self-focus by itself. After the generation of a plasma, the focusing wave front will be de-focused by the plasma. The two de-focusing (diverging) spherical waves would interfere with the now distorted wave front of the reservoir. If the distance between the two hot zones is large, the interference would not result in a strong local field so that further self-focusing of the interfering zone is not possible. But if the two hot zones are close to each other, the interfering field would be large; i.e., another hot zone is created. This new hot zone will further self-focus into a new "child" filament. If there are many hot zones in the initial wave front of the pulse each with a different peak power, they will again undergo interference. If they are all far apart from one another, the interference fringes would be too weak to generate further filamentation. But if they are close to one another, strong local interference fields will give rise to many more "child" filaments downstream in the propagation [5, 32].

According to this multiple filaments competition scenario, when every individual filament is displaced from each other sufficiently, thus avoiding strong interference, each of them will propagate as if it were a single stationary filament. By using adaptive optics, this kind of two-dimensional organization of multiple

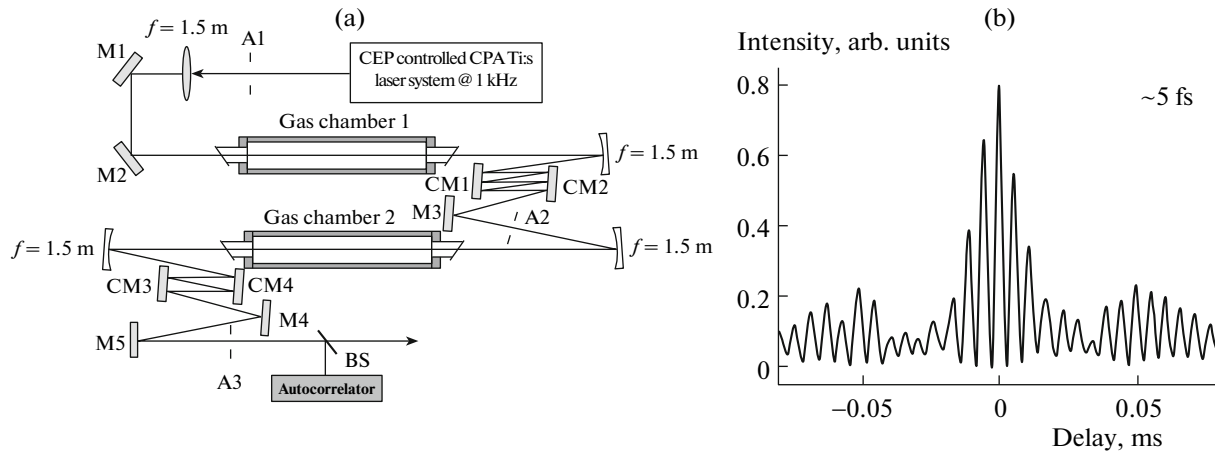


Fig. 1. (a) Experimental setup: Ti:s, Ti:sapphire; A1–A3, softaperture; CM1–CM4, chirped mirrors; M1–M5, silvercoated high-reflection mirrors; BS, beam splitter. (b) Autocorrelation signal of the final compressed 5 fs pulses.

filaments has been experimentally demonstrated [33, 34]. The key is indeed to generate such an initial laser pattern with multiple hot spots well separated.

2.6. Self-Compression of Femtosecond Laser Pulses

The effect of self-compression of femtosecond laser pulse during filamentation has received extensive attention owing to the far-ranging application of few-cycle pulses in attosecond physics [35, 36]. In order to producing intense few-cycle infrared laser pulses, several compression schemes have already been proposed. One well-established technique for pulse shortening makes use of spectral broadening of laser pulses by cascaded filamentation in gases as well as self-phase modulation in a rare gas-filled hollow fiber followed by chirp compensation with suitable dispersive elements such as chirp mirrors [37, 38]. Chen et al. have demonstrated the generation of two-cycle optical pulses with duration of 5 fs and energy of 0.7 mJ at 1 kHz by compressing a 38 fs laser pulse from a carrier-envelope phase (CEP) controlled Ti:sapphire laser system through a cascade filamentation compression scheme [39].

The physics of the self-compression arises from the slice-by-slice self-focusing mechanism of filamentation. The central and front part of the pulse undergo slice-by-slice self focusing leaving behind a series of plasma “dots” in such a way that the front part becomes narrower and narrower. The back part of the pulse would interact with the plasma zone (filament) dispersing the energy of this part of the pulse into the back ground reservoir. Thus, the pulse becomes a structure sharp at the front part and “flat” at the back part. This means self-compression. Later in the propagation, pulse splitting occurs followed by a higher peak at the back part of the pulse while the front part runs out of steam to self-focus and generate a plasma.

A detailed analysis is given in [40]. We describe a typical experiment in what follows.

The experimental setup is illustrated in Fig. 1. The laser source is a conventional chirped pulse amplification (CPA) Ti:sapphire laser system operating at 1 kHz repetition rate, with the oscillator CEP stabilized. This system can provide 4.5 mJ intense pulses with duration of 38 fs (full width at half maximum (FWHM)), but only 2 mJ is exploited in the experiment. The laser pulses are attenuated to 1.4 mJ after passing through a circular soft aperture, A1, the diameter of which is 6 mm, and the aperture edge is irregularly toothed with a modulation depth of 1 mm and anomalous modulation period of 0.5 mm. Then the beam is loosely focused by a thin $f = 1.5$ m lens into the first argon-filled chamber at a pressure of 900 mbar, where a 15-cm-long single filament is generated. The broadened spectrum is dispersion compensated by chirped mirrors -200 fs², delivering stable 9.7 fs pulses and retaining 93% of the input energy. By using another soft aperture, A2 (of the same size as A1), to remove the peripheral low-intensity beam energy, the remaining 1.2 mJ, 9.7 fs pulses are refocused by a silvercoated $f = 1.5$ m concave mirror into the second argon-filled chamber at a pressure of 434 mbar, where a 20-cm-long filament is formed. The output beam after the second chamber comprises an intense white-light core and a low-intensity energy reservoir during filamentation. After several bounces on a pair of chirped mirrors -160 fs², the recompressed pulse of the inner core turns out to be 5 fs (FWHM), which is shown in Fig. 1b. The diameter (at $1/e^2$ of the peak intensity) of this intense central core is about 5.5 mm, which carries an energy of more than 0.7 mJ and contains 67% of the total beam energy. This corresponds to an effective energy efficiency of 50% for the whole compression system. Moreover, a simple and effective method is developed in this work to suppress multiple filament formation and stabilize a single filament by

inserting a soft aperture with an appropriate diameter into the driving laser beam prior to focusing, resulting in an excellent compressed beam quality [39]. The accessible wavelengths of this new type of compression technique have been extended to deep ultraviolet [41] and infrared [42].

2.7. Pressure Independence of Clamped Intensity

What would be the clamped intensity in air (or any gas) when the pressure is changed? An intuitive reaction to this question is naturally that it should depend on the pressure, be it linear or nonlinear. It turns out that it is independent of pressure simply because of the very short laser pulse duration which could not induce any collisional ionization during electron/plasma generation in the self-focusing collapse of the pulse. Theoretical analysis and experimental observation has justified this unexpected result [43]. A quick observation is the following. When the intensity is clamped, the Kerr nonlinear index of refraction for self-focusing ($n_2 I$) is balanced by the index of refraction of the self-generated electron/plasma ($-N_e(I)/2N_{\text{crit}}$). Here, $N_e(I)$ is the electron/plasma density generated at the laser intensity I and N_{crit} is the critical density. In mathematical form, the balance of the change of index of refraction Δn is given by (the \approx sign implies that so far other higher order Kerr terms are neglected in the description of filamentation; we shall come back to this question at the end of this review)

$$\Delta n_{\text{Kerr}}(\text{neutral}) \approx n(\text{plasma}) \quad (4)$$

which becomes

$$n_2 I_c \approx N_e(I_c)/2N_{\text{crit}}, \quad (5)$$

where

$$I_c \approx N_e(I_c)/(2N_{\text{crit}}n_2). \quad (6)$$

Equation (6) can be solved to obtain the clamped intensity I_c . It is a function of N_{crit} , n_2 and N_e . The critical density is given by

$$N_{\text{crit}} = \epsilon_0 m \omega^2 / e^2, \quad (7)$$

with e , m , and ω being the elementary charge, the electron mass and the central frequency of the laser field, respectively. This term is independent of the pressure. n_2 , a material property, is related to the nonlinear susceptibility of the gas medium and is linearly proportional to the pressure. The electron/plasma density N_e depends on the physical process of its generation. In the case of fs laser pulses, only multiphoton/tunnel ionization of the gas is relevant. There is no collisional ionization such as inverse Bremsstrahlung or cascade ionization [15] because the pulse duration is too short, shorter than the mean free time of an electron in one atmospheric pressure of air (~ 1 ps). That means that it depends linearly on the pressure. From Eq. (6), the linear dependences on pressure of the two

terms, one in the nominator (N_e) and one in the denominator (n_2), cancel each other out leaving behind an equation for the clamped intensity independent of pressure. (For the detail of the analysis and experimental verification, see [43].)

Thus, if one sends a very powerful fs laser pulse vertically through the atmosphere in which the pressure decreases with the altitude and assuming that one can control at will the filament position, the intensity in the filament will be clamped to the same value inside the filament at any height. However, the diameter of the filament will increase at higher altitude. This is because the critical power for self-focusing (Eq. (1)) is inversely proportional to n_2 . The latter is proportional to pressure. Hence, the critical power is inversely proportional to pressure or directly proportional to the altitude; i.e., the higher the altitude is, the lower the pressure is and the higher the critical power is. Thus, one needs to deliver more power in the fs laser pulse to high altitudes than at sea level in order to have filamentation. Note that the clamped intensity is

$$I \propto P_c/A, \quad (8)$$

where P_c is the critical power for self-focusing and A , the cross sectional area of the filament core. At high altitude, according to Eq. (8), I_c being unchanged (clamped) while P_c has to be higher, the area A of the filament should be larger. Roughly speaking, since P_c is directly proportional to the altitude, A should also be proportional to the altitude (Eq. (8)) or inversely proportional to the pressure. A consequence of this is that the filament diameter is larger at higher altitude. Thus, since the air pressure or air density is inversely proportional to the altitude, the total number of air molecules inside a filament is roughly independent of the altitude but is proportional to the filament length L . For a filament with a constant length L , the nitrogen fluorescence signal emitted from inside the filament is constant whatever the altitude is so long as there is filamentation.

Another consequence of this phenomenon (see Eq. (8)) is that at higher altitude, there will be more energy inside the larger diameter filament. This could be important from the point of view of remote sensing because the interaction volume would be larger; hence there would be more return signal with respect to the signal from a lower altitude assuming a constant pollutant density.

3. LIMITATION TO REACHING VERY HIGH INTENSITY INSIDE A FILAMENT ZONE

One can use an external focusing element to focus a fs laser pulse and obtain filamentation. In the case of single filamentation, the intensity inside the filament could be increased but not significantly. However, the increase in the plasma density inside the filament could be rather high because of the high order nonlin-

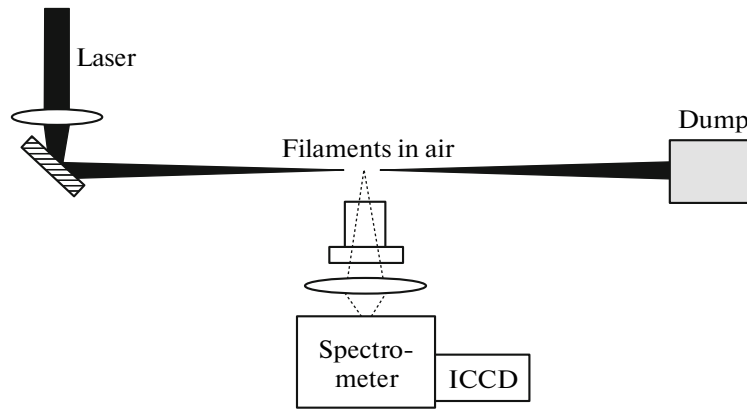


Fig. 2. Experimental set up to measure the fluorescence from the filament zone in air.

ear generation process (multiphoton and/or tunneling ionization) that depends nonlinearly on the intensity. The reason for the insignificant increase in intensity is intensity clamping even if external focusing helps in reducing the focal spot size [27]. Could we then reach a very high intensity by focusing many filaments together into the geometrical focus using an external lens or focusing element?

Let us analyze this problem. If two filaments could be fused into one simultaneously in space and time, the overlap of the two filament cores would in principle give rise to interference zones [5]. One would expect that in the constructive interference zone, the intensity would be four times higher than a single filament would give. This could be done by external focusing one single pulse with two hot zones or by crossing two pulses at a very small angle. In the case of multiple filaments, one could focus the pulse such that all the filament cores would overlap near the geometrical focus. The interference zone would give rise to intensity as high as $2^n I$, where n is the number of overlapping filaments and I , the clamped intensity of one filament. If

we were to focus a large diameter petawatt (PW, 10^{15} W) laser pulse in air, hundreds or more filaments would be created. (Note that the critical power for self-focusing of the Ti-sapphire laser pulse in air is between 5 and 10 GW, depending on the pulse length [44].) Thus interference would result in an enormous intensity. This, unfortunately, would not happen because of intensity clamping as the following shows.

A series of experiments have been performed [45, 46] by focusing 50 fs Ti-sapphire laser pulses in air and argon at power levels ranging from 0.1 to 70 TW (P_c in air of 50 fs pulses is about 10 GW [44]). These pulses did not have a good beam quality and hence multiple filaments naturally occurred. Figure 2 shows an experimental set up.

Ti-sapphire laser pulses of nearly 1.5 TW (47 fs, 70 mJ, 10 Hz, diameter ~ 2.5 cm) were focused by a short 20 cm focal length lens in air. The spectral broadening of atomic oxygen O I (777.4 nm) triplets from

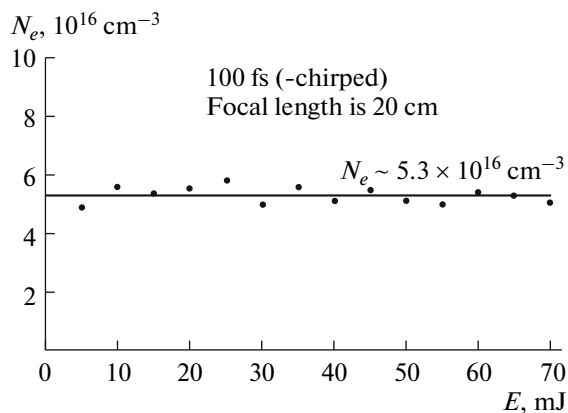


Fig. 3. Measured electron density in the focal region of a 100 fs, negatively chirped pulse in air by varying the pulse energy from 5–70 mJ. The focal length is 20 cm.

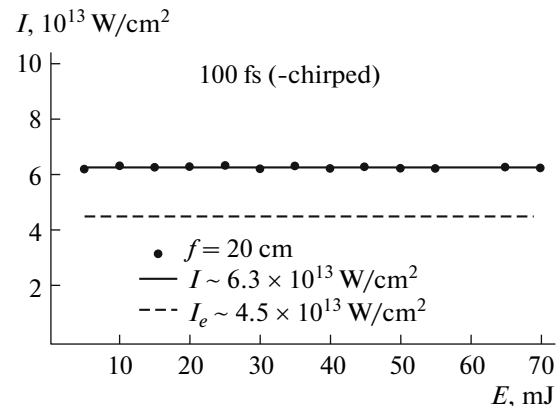


Fig. 4. Measured intensity (dots) in the focal region of a 100 fs, negatively chirped pulse in air by varying the pulse energy from 5–70 mJ. The focal length is 20 cm. The intensity stays the same and is slightly higher than the single free propagating filament's clamped intensity (dashed line).

inside the filament zone was measured from the side. This broadening is proportional to the plasma density and is calibrated [47]. Figure 3 gives the plasma density as a function of the laser pulse energy. It is constant over the whole range of energy used.

Since the intensity dependence of the ionization probability of air molecules (nitrogen and oxygen) can be calculated using the S-matrix theory [45, 46], one can estimate the intensity at which the measured plasma density is produced assuming that the ionization process is purely uni-molecular (i.e., no collisional ionization is involved). Figure 4 (black dots) shows the corresponding calculated intensity inside the filament as a function of laser pulse energy.

This result shows that the intensity inside the filament does not change even if the energy per pulse is changed by more than 10 times. The highest energy used was 70 mJ using 100 fs negatively chirped pulses. The peak intensity was 0.7 TW while the critical power for self-focusing at this pulse length is around 5 GW [44]. Many filaments would have been created near the geometrical focus. At least some overlap is expected. Yet, the measured intensity is unchanged and is ~40% higher than the clamped intensity of a single filament at free propagation (no external focusing) condition (dash line, Fig. 4).

Another experiment was done by tightly focusing 60 fs, 4 J (67 TW) Ti-sapphire laser pulses in air by Ji et al. [46]. The beam diameter was ~15 cm and the focal length of the lens was 1 m. In this experiment, the total nitrogen fluorescence was measured from the side similar to the set up in Fig. 2. Two pulse energies, 4 J and 50 mJ (ratio is 80), of the same duration (60 fs) were used. The ratio of the two peak fluorescence was measured to be about $420/41 = 10.24$. Considering that the nitrogen fluorescence [50, 51] is the result of tunnel/multiphoton ionization [52] and depends on the plasma density inside the ionization zone, one could write down an over simplified empirical relation between the (measured) fluorescence strength, I_f , and the laser intensity, I_{laser} [46] which is that the fluorescence strength is proportional to the ionization rate of nitrogen

$$I_f \propto \text{ionization rate of nitrogen} \propto I_{\text{laser}}^\alpha. \quad (9)$$

The value of α ($\cong 8$) comes from the experimentally measured slope of the ion yield vs intensity curve during ionization of nitrogen molecules by a fs Ti-sapphire laser pulse [4, 53].

This analysis gives an order-of-magnitude type of argument but it is enough to give a physical feeling. The ratio of the intensities inside the filaments is given by

$$\frac{I_{4\text{ J}}}{I_{50\text{ mJ}}} < \left(\frac{I_{f(4\text{ J})}}{I_{f(50\text{ mJ})}} \right)^{1/\alpha} = \left(\frac{420}{41} \right)^{1/8} \approx 1.34, \quad (10)$$

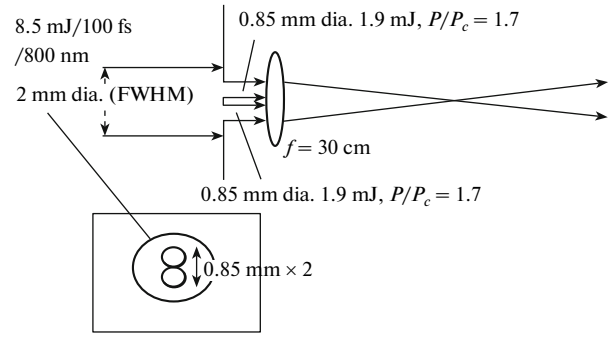


Fig. 5. A theoretical scheme to focus two fs laser pulses towards the geometrical focus of a lens. A screen with two apertures transmits two symmetrically spaced beams from a Gaussian fs laser beam. They pass through a lens and cross at the focus. The dimensions are given in the figure.

where $I_{4\text{ J}}$, $I_{50\text{ mJ}}$ are laser intensities with pulse energy 4 J and 50 mJ, respectively. Since more filaments are produced when a laser energy of 4 J is used, it is reasonable that the fluorescence arising from the 4 J pulse is higher than that from the 50 mJ pulse. However, what is interesting is that from Eq. (10), the fluorescence intensity was increased by only about 34% inside the tight focal region while the energy (power) was increased by 80. Let us make another rough estimation with the previous experiment using 0.7 TW pulses. The f -number of the lens used to focus the 50 mJ pulses is $20/2.5 = 8$ while that of the present lens is $100/15 \approx 7$. Let us say they are roughly equal. Then, as in the case of the previous 70 mJ/100 fs pulse, the intensity in the filament of the current 50 mJ pulse would be roughly equal to that of the previous 70 mJ/100 fs pulse; i.e., $I_{50\text{ mJ}}$ in Eq. (10) would be ~40% higher than the single filament's clamped intensity I_c

$$\begin{aligned} I_{4\text{ J}} &\approx 1.34 I_{50\text{ mJ}} \quad (\text{from Eq. (10)}) \\ &\approx 1.34 \times 1.40 I_c \quad (\text{from Fig. 4}) \\ &\cong 1.88 I_c. \end{aligned} \quad (11)$$

Thus, the intensity inside the tightly focused filament zone of the 67 TW pulse is roughly less than twice that of a single filament in air generated normally by a pulse of ~1 mJ/50 fs = 20 GW. That is, while the initial power ratio of the two pulses is $67/0.02 = 3350$, the ratio of the intensity in the filament zones is less than 2. Even though the estimation is rough, it conveys the principal idea that multiple filaments could not be forced into multiple interference to produce very high intensity.

However, using the argument given above, it is expected that the intensity at the focal zones in both sets of experiments be significantly increased because there would be many filaments fusing together near the focus. This seemingly counter intuitive observation can be explained by the physical process during inten-

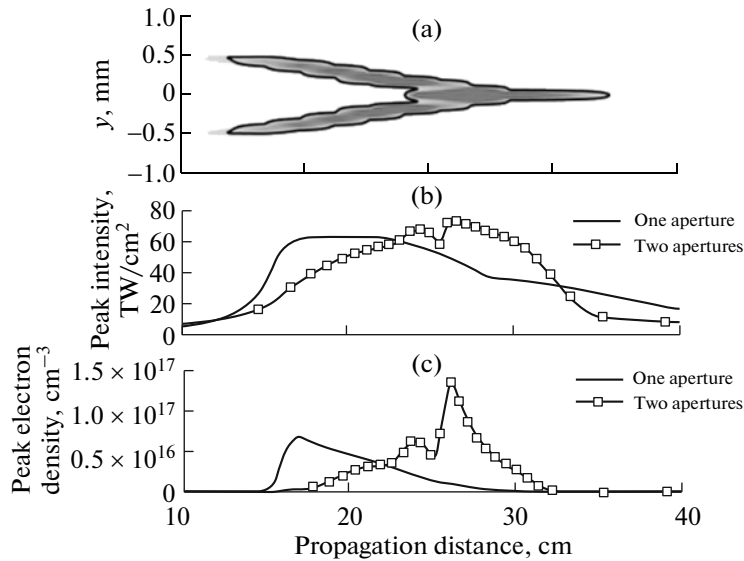


Fig. 6. The simulation results of the interaction scheme in Fig. 5: (a) fusion of two beams; (b) peak intensity distribution along the propagation axis where 30 cm is the geometrical focus; (c) peak electron density distribution.

sity clamping. Kosareva et al. [45] have calculated the fusion of two filaments by passing a fs laser beam with a Gaussian cross section through two adjacent circular apertures before being focused by a lens as shown in Fig. 5.

Figure 6a shows the crossing/fusion of the two filaments generated from the two parts of the beam symmetrically going through the same lens. The fusion position is before the geometrical focus at 30 cm. The two filaments cross and merge into one as they propagate. However, the calculated peak intensity in the crossing region is only increased by 30% as compared to the single filament case coming from one aperture (Fig. 6b). The peak electron density (Fig. 6c) increases by roughly two times. This is again due to the balancing act between the plasma generated by the two pulses and their simultaneous self-focusing act similar to the balance in the single filament case.

Two recent experiments trying to observe the enhancement of intensity inside multiple filaments crossing/fusion and the conclusion again is negative [54, 55].

4. NONLINEAR INTERACTION OF INTENSE FEMTOSECOND FILAMENTS IN AIR

4.1. Introduction

As two or more intense light filaments spatio-temporally approach one another, there would be strong interaction. This has attracted much attention for many potentially important applications and for its distinctive features of particle-like repulsion, attraction, fusion, collision, and spiraling [56–60].

It was recently demonstrated that the strong coupling between two noncollinear filaments could result

in the energy exchange between them [61, 62], which could be further controlled by tuning the frequency chirp of the incident pulses. Such kind of the energy exchange is partly based on the dynamic plasma grating [63] created by the intense noncollinear filaments. Furthermore, it was demonstrated that the third-harmonic generation from the filaments could be dramatically enhanced based on the noncollinear filament interaction [64, 65]. The filament interaction also was demonstrated to be very useful for the nonlinear frequency conversion of ultrashort laser pulses [25] including the efficient generation of ultraviolet pulses [66, 67]. By optimizing the relative phases of the filaments, the interaction among multiple filaments was demonstrated to be controllable [68].

In air, the filament interaction can be induced by the instantaneous Kerr effect, the long lifetime plasma effect, and the recently revealed field-free molecular alignments and revivals. (The physics of molecular alignment by a laser field and the revival of a molecular wave packet will be discussed in detail in Section 8.)

The instantaneous Kerr effect is raised by the pure electronic response which exists within the laser pulse duration, as shown in Fig. 7 (black solid curve). This kind of filament interaction occurs only when the filament pulses are temporally and spatially overlapped. It has been the most popular kind of filament interaction that was studied in the recent past. Laser ionization induced plasma which counterbalances the Kerr effect also participates in the filament interaction. The plasma influences the filament interaction as it is generated by the laser pulse and slowly decays with a typical lifetime of the order of several hundred picoseconds to a few nanoseconds, as shown in Fig. 7 (grey dashed curve). Filament interaction can also be

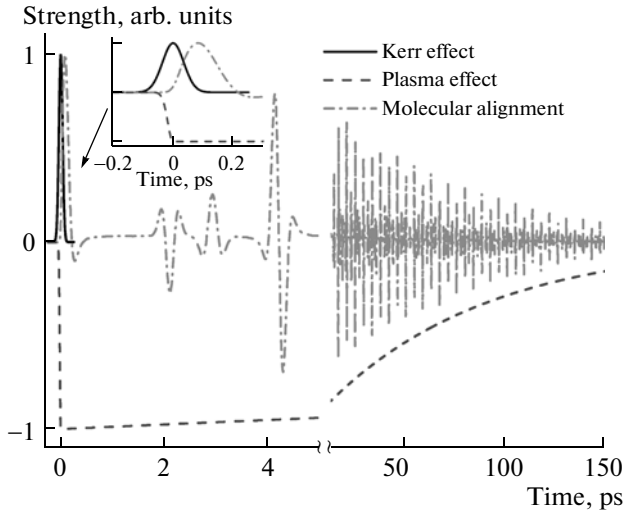


Fig. 7. Different temporal ranges of the Kerr, plasma, and molecular alignment effects for filament interaction in air. The word “strength” along the vertical coordinate has different meanings for different processes. It will be clear later in this section and in Section 8. The inset shows that there is a time delay of ~ 80 fs for the molecular alignment effect with respect to the instantaneous Kerr effect, and the plasma effect participates in the filament interaction since its generation during the pulse duration. The zero time corresponds to the location of the pulse peak.

induced by the non-instantaneous rotational Raman effects related to molecular alignment of diatomic molecules in air, as shown by the grey dash-dotted curve in Fig. 7. The molecules are impulsively aligned by the ultrashort laser pulses through rotational Raman excitation [69], which later dephase and revive periodically after the extinction of the pump pulse. (See Section 8 for detail.) Depending on the relative orientation of the linear molecules with respect to the field polarization, the refractive index experienced by a second properly matched ultrashort filamenting probe pulse is changed by following the molecular alignment and revivals. This index of refraction modification hence dominates the succeeding filament interaction and is indeed field-free achievable. The strength of the molecular alignment and revivals decreases gradually due to the time-dependent decay of the excited coherent rotational states of the molecules and shows a typical lifetime of a hundred picoseconds for air at room temperature as indicated in Fig. 7.

4.2. Filament Interaction due to Kerr Effect

Proportional to the field intensity, the strength of the electronic Kerr effect is described by $\delta n_{\text{Kerr}} \sim n_2 I$, where n_2 is the Kerr nonlinear coefficient related to the third order susceptibility $\chi^{(3)}$ and I is the laser field intensity. When two light filaments, named pump and probe in the following, are spatiotemporally

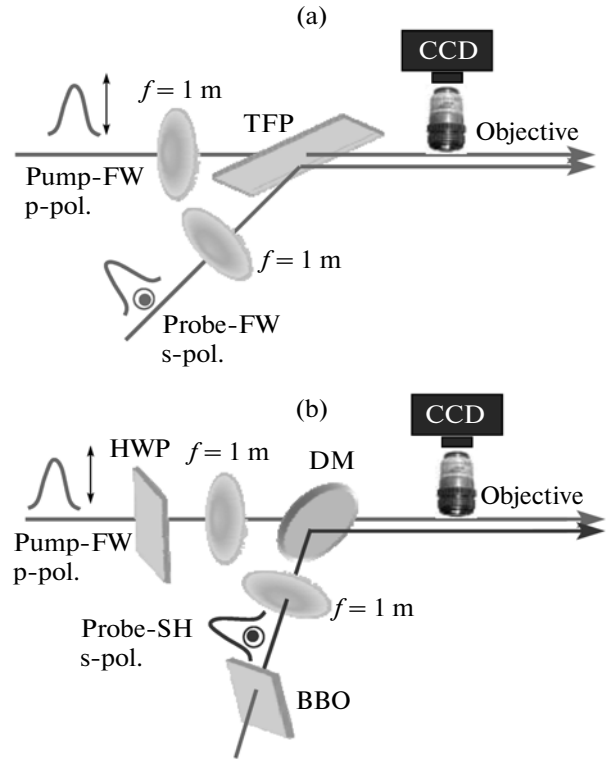


Fig. 8. The experimental setup for interaction between filaments launched in the same direction in air. The wavelengths of the pump and probe pulses are (a) both at 800 nm, and (b) at 800 and 400 nm, respectively. TFP: thin film polarizer; HWP: half wave plate at 800 nm; DM: dichromatic mirror: HR at 400 nm and AR at 800 nm; FW: fundamental wave; SH: second harmonic wave.

approached, the refractive index experienced by each filament increases due to the Kerr effect. The local refractive index changes owing to the Kerr effect are given by [70] $\delta n_{\text{Kerr_pump}}(r) = n_2 I_{\text{pump}} + n_2^{\text{XPM}} I_{\text{probe}}$ and $\delta n_{\text{Kerr_probe}}(r) = n_2 I_{\text{probe}} + n_2^{\text{XPM}} I_{\text{pump}}$, respectively, in the pump and probe filaments, where the n_2^{XPM} is the Kerr nonlinear coefficient induced by the cross-phase modulation (XPM) of the pump (or probe) pulse. The n_2^{XPM} of the parallel field component is 3 times larger than the n_2^{XPM} of the orthogonal field component [10, 70, 71]. (See also Subsection 7.1.) Therefore, the pump and probe pulses experience increased refractive indices when they are temporally overlapped due to the instantaneous XPM (X-Kerr) effect.

4.2.1. Fusion of parallel filaments. The X-Kerr effect based interaction can occur between filaments of different polarizations and wavelengths. As a demonstration, the interaction of two filaments launched in the same direction in air was studied as shown in Fig. 8a.

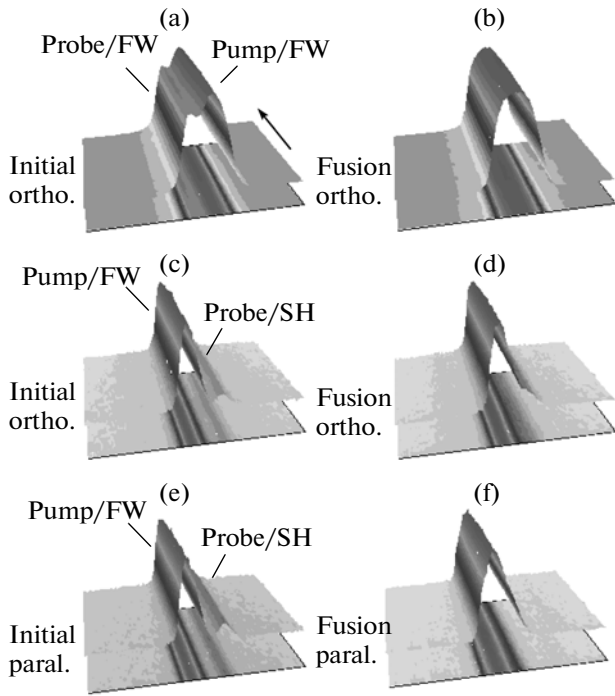


Fig. 9. The fusion between two parallel-launched femtosecond filaments of the same wavelength and orthogonal polarizations [(a) and (b)], different wavelengths and orthogonal polarizations [(c) and (d)], and different wavelengths and parallel polarizations [(e) and (f)] around the zero time delay due to the X-Kerr effect. The filaments propagate along the z direction as indicated by the arrow. The bottom sheets are the projections of the filaments. The initially launched pump and probe filaments merged into one as the fusion occurred.

The filament interaction was characterized by imaging the ionization-induced fluorescence of the nitrogen molecules (see Section 9) in the filament wake to a monochrome digital charge coupled device (CCD) with a microscope objective ($10\times$). The filament separation is defined by the distance between the fluorescence peaks of the filaments. A more detailed description of the experimental setup can be found in [70, 72, 73]. As shown in Fig. 9a, two parallel pump and probe filaments (~ 5 cm in length) at 800 nm with an initial separation of $106\ \mu\text{m}$ were generated by focusing the 1.6 mJ pump and 0.8 mJ probe pulses with two separated fused-silica lenses ($f = 1$ m) before a thin-film polarizer (see Fig. 8a).

The polarizations of the pump and probe filaments were orthogonal to each other. As shown in Figs. 9a and 9b, filament attraction and even fusion were observed as a result of the X-Kerr effect around the zero time delay [70, 72]. Furthermore, filament interaction due to the X-Kerr effect could be observed for filaments at different wavelengths, such as for the fundamental wave (FW) at 800 nm and its second harmonic (SH) at 400 nm. As shown in Fig. 8b, a SH

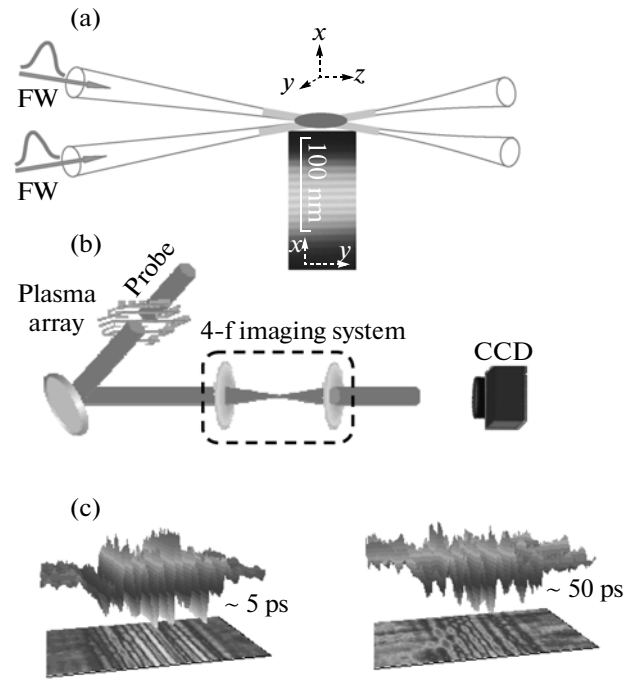


Fig. 10. (a) The one-dimensional plasma array created by non-collinear interaction of two filaments. (b) The probe system for the plasma array imaging. (c) The measured 1D plasma array at different time delays after its generation. The bottom sheets in (c) are the projections of plasma arrays.

pulse was generated by using a $200\text{-}\mu\text{m}$ -thick β -BBO crystal, and the polarization of the FW pulse could be rotated with a half-wave plate. The energies of the FW and SH pulses were measured to be ~ 1.00 and 0.25 mJ after the combining dichromatic mirror, which led to two $100\text{-}\mu\text{m}$ -separated parallel filaments of ~ 6.5 and 14.0 cm, respectively. As shown in Figs. 9c and 9d, attraction and fusion of the FW and SH filaments [73] could be ensured by the X-Kerr effect as they were temporally overlapped. Since the Kerr nonlinear coefficient n_2^{XPM} induced by the XPM was larger for the parallel polarizations than that of the orthogonal polarizations, as shown in Figs. 9e and 9f, the filament attraction and fusion were much stronger for the parallel polarized filaments with more fluorescence intensity as compared to the orthogonally polarized filaments. As a result, for the same pulse duration and intensity, the time ranges (the relative time delay between the pump and probe pulses) for filament attraction and fusion were much larger for parallel polarized filaments than that of orthogonally polarized ones as demonstrated in detail in [73].

For parallel polarized filaments of the same wavelength, interference is involved which affects the filament interaction. The Kerr effect induced refractive index in the interaction region is increased and

decreased for the constructive and destructive interference, respectively. Therefore, by controlling the relative phase of the filamenting pulses, the Kerr effect can steer the filaments to be attracted or fused for in-phase filaments and repulsed for out-of-phase filaments, respectively. This interesting filament interaction was numerically predicted [74] and was very recently experimentally confirmed [75].

4.2.2. Two crossing filaments. The filament interaction becomes more interesting for crossed filaments when they are temporally synchronized. As shown in Fig. 10a, two femtosecond laser pulses (50 fs, 1 mJ, 800 nm) were focused in air with two separated lenses ($f = 1$ m), and crossed at an angle of $\sim 7^\circ$.

The constructive interference between the filamenting pulses increased the field intensity in the interaction zone, where the local refractive indices were increased due to the Kerr effect. Correspondingly, more energy was attracted into the interference peaks which further increased the field intensities. On the other hand, the increase of the field intensities was limited by the correspondingly increased local plasma densities that defocused the interference peaks. Consequently, self-channeled parallel sub-filaments were formed along the interference peaks. The inset of Fig. 10a shows the one-dimensional plasma waveguide array could be created by means of interference-assisted coalescence of the noncollinear filaments, which featured wavelength-scale periodic modulation of the plasma density and could guide the input pulses equivalently as a photonic crystal plasma waveguide [63]. As shown in Fig. 10b, the plasma array with periodically modulated refractive index could also be probed by a time-delayed pulse crossed at a right angle. The imaging system in 4-f configuration composed of two lenses enabled us to have the real spatial distribution of the plasma array. The measured plasma arrays at various time delays after its creation are shown in Fig. 4c, indicating quite a long lifetime of the plasma array. Such a plasma array could be adjusted by changing the intensity ratios, crossing angles, and field polarizations of the generating pulses [63]. A maximal modulation depth of the plasma array was achieved for filaments with parallel polarization with an intensity ratio of 1:1, whose transverse period was determined by the noncollinear crossing angle of the incident beams.

Beyond the one-dimensional plasma arrays, two-dimensional plasma arrays could be created by the noncollinear interaction between three filaments. The noncollinear filament interaction induced photonic-crystal plasma waveguides could be used to guide high-intensity pulses over long lengths in gases benefiting from the periodically modulated plasma density.

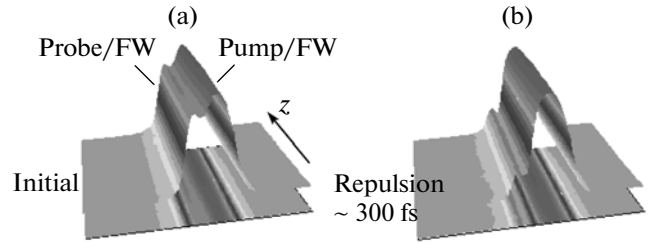


Fig. 11. The repulsion of the parallel probe filament by plasma generated by the advancing pump for two parallel-launched femtosecond filaments. The probe pulse was ~ 300 fs delayed with respect to the pump pulse in (b) as compared to that in (a). The filaments propagated along the z direction as indicated by the arrow.

4.3. Filament Interaction due to Plasma Effect

The multi-photon ionization induced plasma also participates in the filament interaction due to the negative contribution of the refractive index change, proportional to $\delta n_{\text{plas}}(r) = -0.5\rho(r)/\rho_c$, where ρ is the electron density and ρ_c ($\sim 1.7 \times 10^{21} \text{ cm}^{-3}$ at 800 nm) is the critical plasma density. As shown in Fig. 7, the plasma is generated within the pulse duration and decays gradually after the extinction of the laser pulse with a typical lifetime of the order of a few hundred picoseconds depending on its initial density. As it is well established for single filaments, the multi-photon ionization induced plasma acts as a defocusing lens against the Kerr self-focusing to support long distance propagation of light filament (see Section 2). For two parallel launched filaments propagating closely in space, the plasma of sufficient density in one filament wake that acts as a negative optical potential also influences the propagation of the other filament. For femtosecond filaments of orthogonal polarization at 800 nm launched in the same direction in air [see Fig. 8a for the experimental setup, the pump and probe pulse of 1.6 and 0.8 mJ were focused with two separated fused-silica lenses ($f = 1$ m) before the thin-film polarizer], filament repulsion by the plasma effect was clearly observed [70, 72] at a time delay of ~ 300 fs as shown in Fig. 11b, resulting in a larger filament separation as compared to Fig. 11a. Such filament repulsion could also be observed for a wide range of time delay until significant decay of the plasma density.

4.4. Filament Interaction due to Molecular Alignment

For a typical light filamentation in air, most of the molecules survive in the filament wake due to weak molecular ionization. These neutral molecules are impulsively aligned by the intense ultrashort filament pulse through rotational Raman excitation. In general, as shown in Fig. 12a, the molecular alignment is characterized by the statistical term $\langle\langle \cos^2\theta \rangle\rangle$ [69], where θ is the crossing angle between the laser field

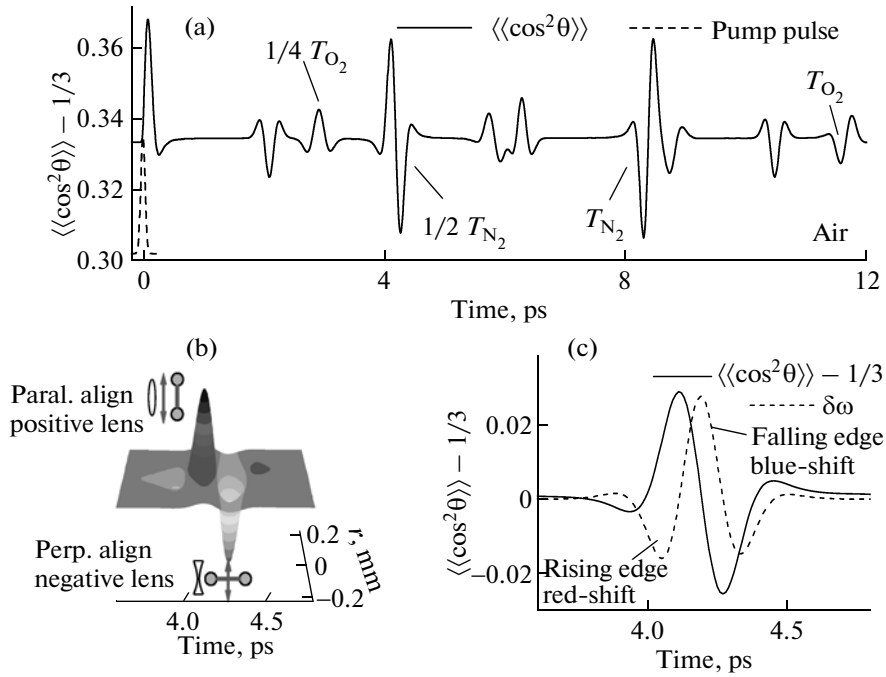


Fig. 12. (a) The simulated molecular alignment metric $\langle\langle\cos^2\theta\rangle\rangle$ of the N_2 and O_2 molecules in air as a function of time delay. The black-dashed curve stands for the envelope of the pump pulse. (b) The spatiotemporal profile of the refractive index change experienced by a linearly polarized ultrashort laser pulse (marked with arrows) at the half revival time of N_2 as its time delay is tuned to match the molecular alignment revival. (c) The time-dependent phase modulation induced by the rapid evolution of the molecular alignment revival.

polarization and molecular axis (see Section 8 for the detailed physics of alignment and revival).

4.4.1. Principle of molecular alignment effect. The impulsive kick of the ultrashort laser pulse leaves the molecules aligned into an excited rotational wave packet parallel to the laser's linear polarization. Periodic de-phasing and revivals of the impulsive molecular alignment follow due to the quantum beatings of the excited rotational states in the wave packet. For molecular N_2 and O_2 in air, the revival periods, determined by the molecular rotational constants, are $T_{N_2} = 8.3$ ps and $T_{O_2} = 11.6$ ps, respectively, as shown in Fig. 12a. The in-phase (positive peak value of $\langle\langle\cos^2\theta\rangle\rangle$) and anti-phase (negative peak value of $\langle\langle\cos^2\theta\rangle\rangle$) beatings of the molecular wave packets correspond to the parallel and perpendicular alignment of the molecules, respectively.

The great interest of the molecular alignment in filament interaction originates from the orientation-dependent refractive index of the molecules, which is controllable and modulates the spatiotemporal phase of the properly matched filamenting probe pulse [76, 77]. The additional refractive index change induced by the molecular alignment is $\delta n_{\text{mol}}(r, t) = 2\pi(\rho_0\Delta\alpha/n_0)[\langle\langle\cos^2\theta(r, t)\rangle\rangle - 1/3]$, where $\Delta\alpha = \alpha_{\parallel} - \alpha_{\perp}$, ρ_0 , and n_0 denote the molecular polarizability difference between the components parallel and perpen-

dicular to the molecular axis, initial molecular density, and linear refractive index of randomly orientated molecules, respectively. For molecular alignment parallel or perpendicular to the field polarization with $\langle\langle\cos^2\theta\rangle\rangle$ greater or less than $1/3$, the refractive index is increased or decreased, respectively, as compared to the randomly orientated molecules. Since the degree of molecular alignment is proportional to the field intensity before its saturation [78] and evolves rapidly in the time domain, it will introduce an additional spatiotemporal phase modulation to the properly matched ultrashort probe laser pulse [76]. This modulation becomes easily observable around the revival periods as alignment-induced change of the refractive index follows the ultrafast evolution of the molecular rotational states in the typical time scale of a few hundreds fs.

Excited by a femtosecond pulse of Gaussian-shaped transverse profile, Fig. 12b shows the numerical simulation of the alignment-induced refractive index change $\delta n_{\text{mol}}(r, t)$ for room-temperature air around the half-revival time of molecular N_2 . The refractive index change at the beam center is larger than that at its periphery due to the larger molecular alignment degree at the beam center. The parallel and perpendicular molecular alignments with increased and decreased refractive index change then account for additional effects of cross-focusing (positive lens)

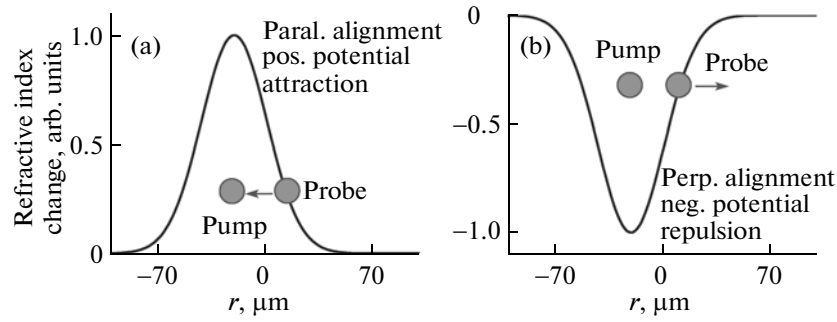


Fig. 13. Schematic illustrations of (a) the positive refractive index potential and (b) the negative refractive index potential created by the pump pulse induced parallel and perpendicular molecular alignment revivals, respectively. The properly matched probe pulse propagates nearby the positive and negative refractive index potentials is attracted and repulsed by the pump pulse, respectively.

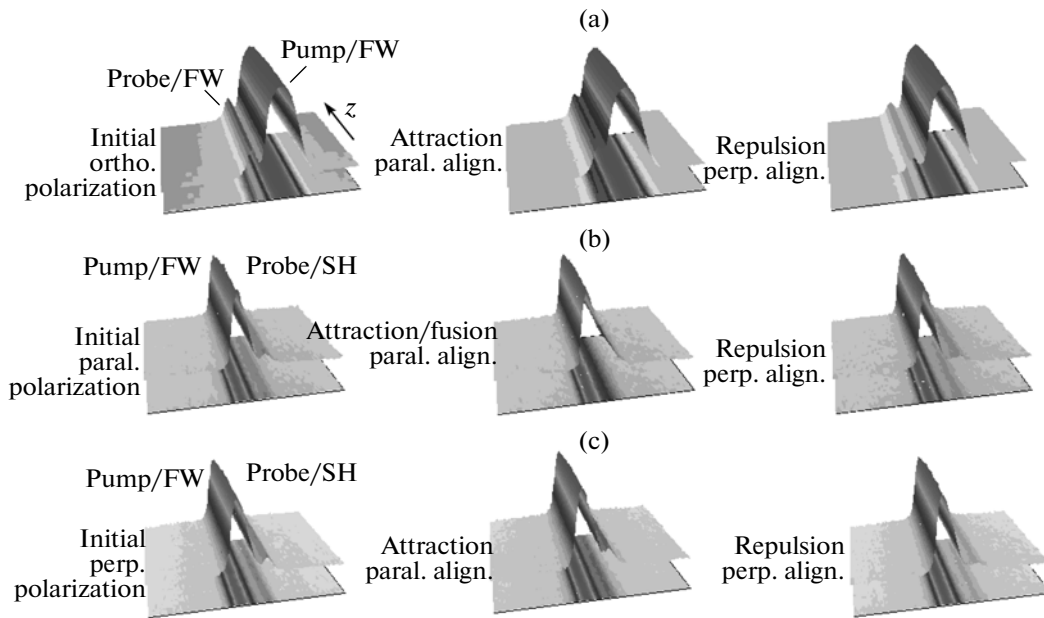


Fig. 14. The controllable attraction, fusion, and repulsion between two parallel launched femtosecond filaments by the field-free molecular alignment revivals. The pump and probe filaments are set to have (a) perpendicular polarizations of the same wavelength at 800 nm, (b) parallel polarizations of different wavelengths at 800 and 400 nm, and (c) perpendicular polarizations of different wavelengths at 800 and 400 nm, respectively. The filaments propagate along the z direction as indicated by the arrow. The bottom sheets are the projections of the filaments.

and cross-defocusing (negative lens), respectively, as shown in Fig. 12b. Such a cross-defocusing effect has been used to characterize the field-free molecular alignment [79] by measuring the molecular alignment induced diffraction of a probe pulse.

Similar to the self-phase modulation induced by the intensity-dependent Kerr effect, the time-dependent revival of the molecular alignment introduces an additional nonlinear phase shift φ_{mol} to a properly matched ultrashort probe pulse, corresponding to a spectral phase modulation given by $\delta\omega_{\text{mol}}(t) = -\partial\varphi_{\text{mol}}/\partial t \sim -\partial\delta n_{\text{mol}}(t)/\partial t$ as shown by the black dashed curve in Fig. 12c. Hence, the rising and falling

edges of the molecular alignment revival account for red and blue shifts of the properly matched ultrashort laser pulse, respectively. This controllable spectral modulation of a time delayed femtosecond laser pulse propagating in pre-aligned molecules was demonstrated in [80], where additional red- and blue-shifted frequency components were generated when its time delay was tuned to match the rising and falling edges of the molecular alignment revival. More details of spectral shifts will be given in Section 8.

4.4.2. Filament attraction and repulsion by molecular alignment. It is clear that based on the orientation-dependent refractive index change of the molecules,

controllable optical potentials with modulated refractive index can be created by the molecular alignment. For a general spatially Gaussian-shaped excitation pulse with higher field intensity at the beam center than its periphery, the refractive index optical potential gradually decreases with the distance away from the beam center. For an ultrashort laser pulse propagating nearby the optical potential, as shown in Fig. 13, it is attracted or repulsed by the positive or negative refractive index potentials [70, 72], respectively.

Since pump-excited molecular alignment and revival could induce a change of index of refraction in a probe pulse, filament attraction and repulsion would occur in a way similar to the effect of XPM demonstrated in Fig. 9. This is shown in Fig. 14. An advancing ultrafast pulse aligns molecules and a second time-delayed probe filamenting pulse experiences the refractive index change in the molecular rotational revivals, typically a few (or tens) picoseconds delay from the aligning pulse. For two orthogonally polarized pump and probe femtosecond filaments at 800 nm launched in the same direction (see Fig. 8a for the experimental setup), the parallel launched probe filament (initially separated by $\sim 106 \mu\text{m}$) could be attracted by the pump for parallel molecular alignment revival, resulting in a decreased filament separation of $\sim 94 \mu\text{m}$ as shown in Fig. 14a around the half revival of molecular N_2 in air.

Furthermore, using pump and probe of different wavelengths (800 and 400 nm) with either parallel or perpendicular polarization, fusion or repulsion of filaments was observed at the full revival time of N_2 molecule in air, as shown in Figs. 14b and 14c. More detailed discussions can be found in [70, 72, 73].

4.4.3. Some consequences of molecular alignment.

Recently, a cross-(de)focusing assisted polarization spectroscopic technique [81] was demonstrated to measure the transient alignment of the molecules, where both the spatial and polarization modulation of the probe pulse by the molecular alignment are considered. By detecting only a small part at the center of the probe pulse, the cross-defocusing assisted polarization spectroscopy measurements show us whether the molecules are transiently parallel or perpendicularly aligned. Meanwhile, the orientation-dependent ionization of the molecules during the pump pulse excitation could be extracted from the measured molecular alignment signal [81], which could therefore be used to reveal the involved ionization during the impulsive molecular alignment and might be extended to characterize the weakly ionized filaments in molecular gases.

For the low dispersion of the gaseous molecules, the molecular alignment was recently proposed to tune the central wavelength of few-cycle laser pulses [82]. The few-cycle laser pulse was accurately put in an advancing femtosecond filament channel in a molecular gas, such as air, where the molecules were impul-

sively aligned. The central wavelength of the time delayed few-cycle pulse could be effectively tuned with desired red or blue shifts, while keeping the temporal duration almost unchanged. Traditionally, wavelength tunable few-cycle laser pulses can be obtained by means of noncollinear optical parametric amplification, where a specially-cut, thin nonlinear crystal is required and the spectral bandwidth is critically limited by the phase matching condition. Nevertheless, the time-dependent molecular alignment revivals break these limits for few-cycle pulses of tunable central wavelengths. By using the XPM of the molecular alignment revivals, similar spectral modulations of the time-delayed femtosecond laser pulses were also observed [73, 83, 84].

Because of its advantages of controllable dynamics and non-interference influence on the succeeding processes, field-free molecular alignment has been extensively studied for molecular orbital reconstruction [85], ultrashort laser pulse generation [86–89], high harmonic generation [89, 90], and so forth. It was recently demonstrated that the propagation dynamics of a time-delayed ultrashort probe pulse could be significantly influenced by properly matching it to the molecular alignment wakes in an advancing femtosecond filament wake [83], where periodical trapping and diffraction of the probe filamenting pulse were observed for the parallel and perpendicular revivals, respectively. Similar trapping and destruction of intense femtosecond filament were reported [84]. The molecular alignment in the femtosecond filament wake was also demonstrated as a polarization separator [91] for a time-delayed ultrashort laser pulse.

The propagation of ultrashort laser pulses in pre-aligned gaseous molecules is dominated by several effects in the addition to spatiotemporal XPM: the spatial confinement or diffraction by the cross-(de)focusing of the parallel or perpendicular molecular alignment which functions as a positive or negative lens; the time-dependent phase accumulations that induces red or blue shifts for the rising or falling edge of the molecular alignment revivals; the enhanced or weakened self-phase modulation, self-steepening, and other high order nonlinear processes that contribute to the spectral modulation. Assisted with the molecular alignment, it was proposed [87] that a femtosecond light filament could be dramatically enhanced with an increased filament length and a significantly broadened spectrum, leading to the generation of a self-compressed few-cycle pulse. For the cross-(de)focusing effect of the molecular alignment, the collapse distance of a given incident laser pulse was increased and decreased for the perpendicularly and parallel aligned molecules, respectively. The effective nonlinearity of the molecules is equivalently increased for the cross-focusing effect, which correspondingly decreases the threshold for filamentation. For instance, in air, X-wave light bullets can be generated along the intense filament with input ultrashort laser pulses of several mJ

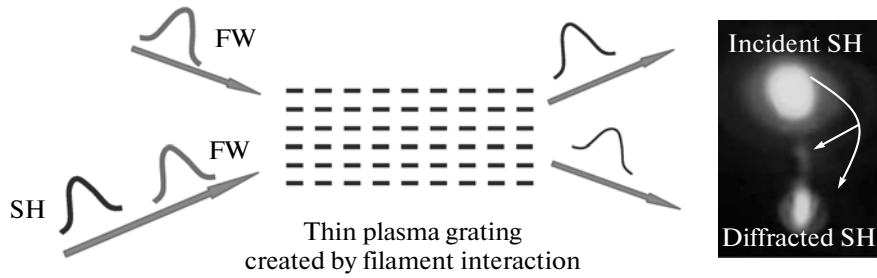


Fig. 15. The energy transfer of a time-delayed (delay time = 1 ps) second-harmonic pulse from the pump arm to the probe arm by the pump-probe filament interaction induced one-dimensional plasma array.

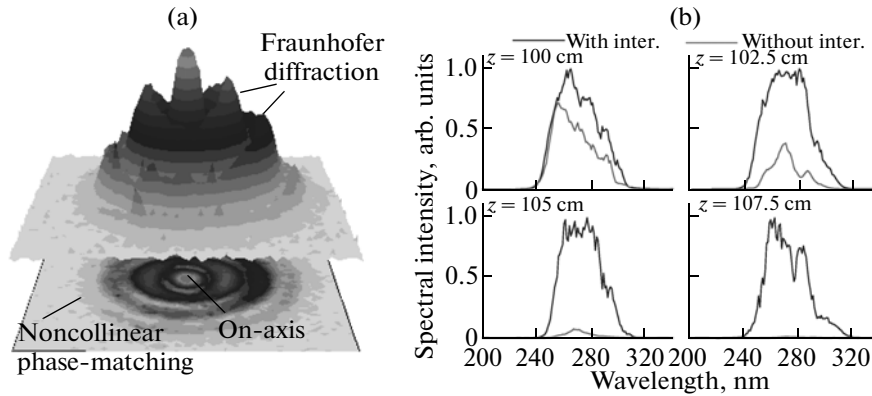


Fig. 16. (a) The measured beam profile of the generated third-harmonic pulse from the filament. The bottom sheet is the projection of the beam profile. (b) The measured spectra of the generated third-harmonic pulse from the probe filament at various propagation distances. $z = 0$ is located at the focusing lens and along the propagation direction of the FW pulse. The grey solid and light grey dashed curves account for the cases when the noncollinear interaction with the pump filament is turned on and off, respectively.

in energy [92], which is much higher than those in the quadratic nonlinear media [93, 94]. However, by using molecular alignment, it was shown [88] that X -waves could be generated in air for modest input pulse power and temporal duration. Much more details on the few-cycle shocked X -wave with controllable rising or falling edges can be found in [88].

4.5. Applications of Filament Interaction

4.5.1. Spatial transfer of probe energy. As mentioned above, plasma arrays or waveguides could be generated by noncollinear interaction of femtosecond filaments ensured with the interference Kerr effect (see Fig. 10). As demonstrated in [63], self-guiding of the interacting pulses by the plasma waveguides could result during their generations where the input femtosecond pulses were partly guided by the periodically modulated plasma waveguide and emitted from the bisector. For the small crossing angle (few degrees) of the noncollinear filaments, a thin plasma grating is generated as shown in Fig. 15, which could be used to diffract a time-delayed ultrashort pulse.

The diffraction angle of the SH pulse (seeded along the pump FW pulse) was governed by $\varphi_m = m\lambda_d/\Lambda$ (under the approximation of $\sin\varphi_m \cong \varphi_m$) ($m = 0, \pm 1, \pm 2, \dots$), where φ_m denotes the m th-order diffraction angle, λ_d is the wavelength of the SH light wave, and Λ is the spatial period of the generated thin plasma grating. As shown in Fig. 15, by propagating a time-delayed SH pulse (delay time is 1 ps) along one of the FW filament, the first and second orders of the diffracted SH pulses locate along the bisector and propagation direction of another FW filament were observed, respectively. A maximum energy transfer efficiency of $\sim 2.3\%$ was observed due to the second-order diffraction of the created plasma grating by two noncollinear FW filaments at a crossing angle of $\sim 3^\circ$. The energy transfer efficiency decreased gradually as the time delay was increased due to the expansion and decay of the created plasma array. Therefore, efficient energy transfer from one filament to another could be ensured by the filament interaction assisted plasma array [95], which functioned as a plasma grating to diffract the time-delayed ultrashort laser pulses.

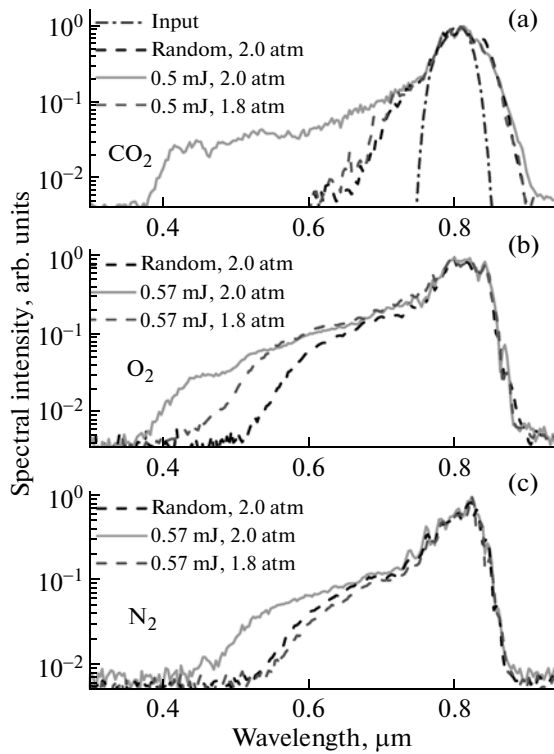


Fig. 17. The measured supercontinuum spectra at the output of the probe filament as its time delay was tuned to match the parallel molecular alignment revivals of molecular (a) CO_2 , (b) O_2 , and (c) N_2 . The energy in each figure indicates the 35-fs pump pulse's energy.

4.5.2. Efficient third harmonic generation. The self-guided filament was demonstrated to be a suitable channel for nonlinear frequency conversion, such as third-harmonic generation (THG) whose phase is nonlinearly locked to the FW filament pulse over a distance much longer than the characteristic coherent length [66, 96]. However, the energy conversion efficiency is still limited. As compared with a single femtosecond filament in air, it was recently demonstrated that the THG could be significantly enhanced by noncollinear filament interaction [97], which was critically dependent on the crossing angle, intensity ratio, and relative polarization between the incident pulses. For example, two non-collinearly crossed FW pulses (0.85 mJ for each pulse, 50 fs) are focused by using two separate lenses of the same focal length of $f = 100$ cm. We measured the TH generation from one of the FW pulses by changing the relative time delay, polarization, and energy of the other incident FW pulse. Two fused silica prisms were used to separate the generated TH pulse from the FW. The beam profile of the generated TH was taken by CCD. As shown in Fig. 16a, the generated third-harmonic (TH) pulse from the intense self-guided filament shows a well-defined on-axis core surrounded by multiple off-axis rings.

The on-axis TH core could be understood to have originated from the FW filament with nonlinearly modulated refractive index. The off-axis multi-rings came from the off-axis noncollinear phase matching between the on-axis FW and off-axis TH pulses as well as the Fraunhofer diffraction of the generated on-axis TH pulse [98]. For a single filament, the energy and multiringed beam profile of the generated TH pulse decreased rapidly and eventually disappeared with the termination of the FW filament. However, in the presence of filament interaction, the generated TH pulse showed almost constant energy and a multi-ringed beam profile over a much longer distance. Figure 16b shows the measured spectra of the generated TH pulse from the probe FW filament when its noncollinear interaction with the pump FW filament was on and off, respectively. The maximum enhancement factor of the THG was achieved when the intensities of the two pulses were approximately equal for the maximum modulation depth of the field interference induced grating. By adjusting the relative polarization of the FW pulses from parallel to orthogonal, the THG decreased rapidly as the field interference induced grating was switched off. For an optimal crossing angle of $\sim 13^\circ$, a maximal THG enhancement factor of ~ 174 in energy was achieved for parallel polarized input FW pulses with an intensity ratio of one. Here, the enhancement of the generated TH pulse was measured by focusing in a photomultiplier tube (PMT). The observed THG enhancement is understood to be a consequence of the elongated filamentation due to the noncollinear filament interaction [97].

4.5.3. Molecular alignment enhanced supercontinuum generation. Usually, broadband supercontinuum (SC) spectrum can be generated by intense filament in air [98] but needs very high power pulses with multiple filaments. Interestingly, it was recently demonstrated [99, 100] that the SC generation by a time-delayed femtosecond laser pulse with modest energy could be readily controlled/enhanced by collinear interaction with another advancing femtosecond filament through the impulsive molecular alignment. At the parallel revival of the molecular alignment created by an advancing pump filament, the SC generation by the time-delayed femtosecond probe pulse could be turned on gradually with extended blue-shifted frequency components as the degree of molecular alignment increased. The parallel molecular alignment induced cross-focusing effect and the consequently promoted self-phase modulation as well as self-steepening effect played important roles for the observed control of the SC generation. For a 35-fs probe pulse with an input energy of 1.5 mJ focused in a gas cell with a lens of $f = 60$ cm, Fig. 17 shows the dependence of the output spectra of the collinearly propagating probe pulse on the pump pulse energy and gas pressure when its time delay was tuned to properly match the parallel half-revivals of the molecular CO_2 , O_2 , and N_2 created by an advancing pump filament, respectively.

Among them, the molecular CO_2 is the most suitable molecule for broadband SC pulse generation using molecular alignment, since its polarizability $\Delta\alpha$ is larger than those of the O_2 and N_2 molecules.

Meanwhile, the beam breakup of the probe pulse due to the multi-filamentation was suppressed as the spectral energy was redistributed to the SC frequency components. Eventually, a linearly polarized ultra-broadband SC pulse with the pulse energy of 1.2 mJ was generated in a single filament core. The impulsive molecular alignment in the wake of an advancing pump filament provides us an additional tool to effectively control the SC generation from another time-delayed intense femtosecond filament in molecular gases.

As the input energy of the time-delayed femtosecond filament further increased, high-order nonlinear processes such as multi-filamentation and multiphoton ionization were much stronger to compete with the SC generation [101]. This makes the high-energy SC pulse generation different from the low-energy case. As very recently demonstrated [102], a stable SC pulse of 1.8 mJ in a single core with the spectrum ranging from 400 to 900 nm can be generated when the time delay of the 35-fs probe pulse with the pulse energy of 2.7 mJ (focused with a lens of $f = 2$ m) was tuned to match the perpendicular molecular alignment revival. It was quite different from the case when the low-energy probe pulse was used for the SC generation by the parallel molecular alignment revivals [99, 100]. The cross-defocusing effect loosened the focusing condition of the high-energy probe laser pulse, which increased the filament length. The elongation of the filament length was indeed observed [87]. The ionization loss was also decreased due to the reduced ionization probability for the perpendicularly aligned molecules [103]. The SC generation was therefore enhanced, and a linearly polarized ultra-broadband SC pulse with the pulse energy of 1.8 mJ was eventually generated.

Since for most filament-based applications, a long filament length is desired, the above observation of filament elongation is important. An example is shown in Fig. 18. By propagating a probe filamenting pulse with an input pulse duration of 35 fs and energy of 2.26 mJ in the perpendicularly aligned molecules created with an advancing pump filament, the probe filament length were controllably increased from 27 to 51 cm as the input pump energy was increased [104].

Meanwhile, as compared with the case of randomly orientated molecules, the onset position of the probe filament moved backward due to the cross-defocusing effect by the perpendicular molecular alignment revival. Consistent with the high-energy SC generation [102], the length of high-energy femtosecond filament was elongated at the perpendicular molecular alignment revival with the cross-defocusing effect. However, for a low-energy probe filament, as pre-

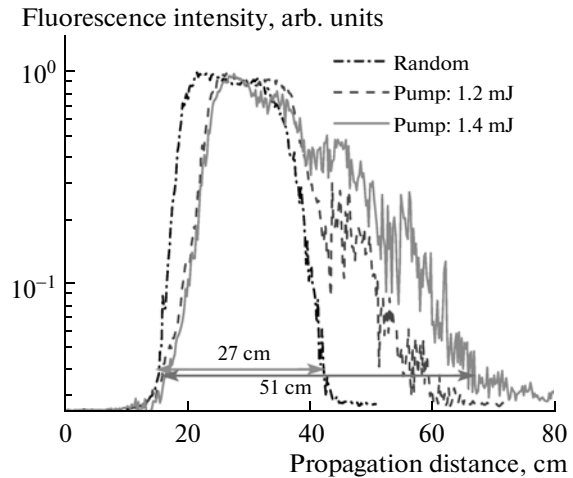


Fig. 18. The dependence of the probe filament length on the input energy of the pump filament, which accounts for the degree of the molecular alignment. The filament length is characterized by measuring the fluorescence of the photon ionized N_2 . In order to eliminate the influence of the input pulse and supercontinuum emission, a dielectric mirror (HR 800 nm @ 0°) and a bandpass filter (UG11, transmission 200–400 nm) were placed in front of the detector.

dicted in [87], filament length increase was observed at the parallel revival of the molecular alignment with the cross-focusing effect which enhanced the filament dynamics.

4.5.4. Broadband energetic UV pulse generation.

Apart from the filaments in the near infrared range, molecular alignment assisted filament interaction can also be extended to the ultraviolet region. High-energy ultrashort ultraviolet pulses are significant for precision spectroscopy measurements. The spectral bandwidth of the generated ultraviolet pulses is usually limited by the phase matching condition of the frequency conversion processes in nonlinear crystals, and the energy conversion efficiency was influenced by the group velocity mismatch between the ultrashort laser pulses. These limits can be broken by using the molecular alignment assisted filament interaction, leading to broadband high-energy ultraviolet pulse generation. As shown in Fig. 19, based on group velocity compensated cascaded second-order nonlinear frequency mixing processes in BBO crystals with input FW pulse at 800 nm (13.8 mJ/70 fs), a high energy TH pulse of ~ 1.1 mJ per pulse at 267 nm was generated with a spectral bandwidth of ~ 2 nm.

The spectrum of the UV pulse was then ~ 6.5 times broadened by interacting with the molecular alignment revivals in the intense filament wake of a FW pulse (7.0 mJ/70 fs). The FW pulse used for molecular alignment was actually the residual part of the FW pulse after the TH generation, which separated from the TH pulse by using dichroic mirror. The filamentation of the UV pulse was enhanced by the parallel half-

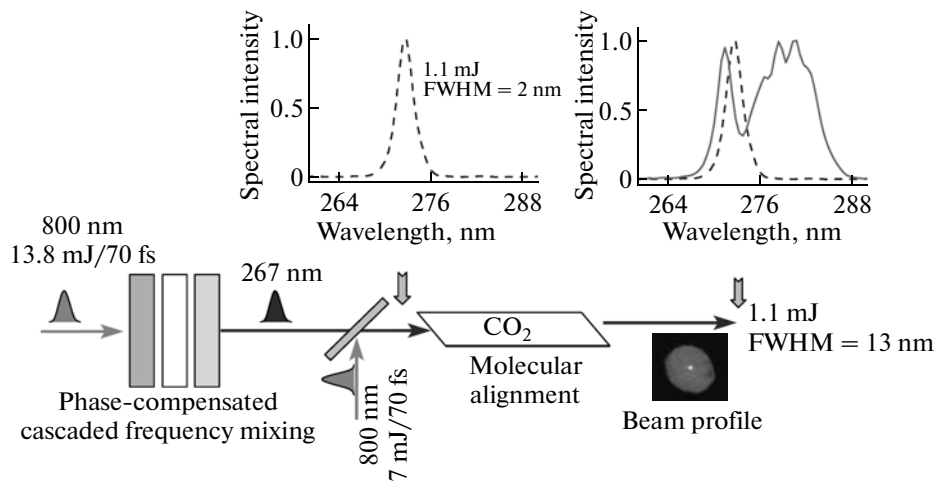


Fig. 19. Schematic illustration of the experimental setup for high-energy broadband third harmonic generation by cascaded frequency mixing and subsequent molecular alignment based filament interaction. The pulse energies of the 70-fs FW pulses used for TH generation (left) and molecular alignment (bottom) were 13.8 and 7.0 mJ, respectively.

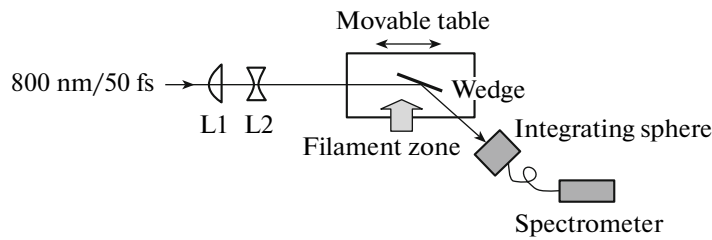


Fig. 20. Measuring the spectra in the forward direction of a filament. L1: plano-convex lens ($f = 50$ cm); L2: biconcave lens ($f = -25$ cm); beam diameter: 2.75 mm (after L2). The beam is collimated after L2 at low energy. Distance in Fig. 21 is measured from lens L2.

revival of the pre-aligned CO_2 molecules, which broadened the output spectrum of the UV pulse. As a result, energetic broadband UV laser pulse with pulse energy of ~ 1.1 mJ and spectral bandwidth of ~ 13 nm (full width at half maximum) could be generated as recently demonstrated in [105].

4.6. Summary of Filament Interaction

Filament interaction, either by the instantaneous Kerr effect, long lifetime plasma effect, or impulsive molecular alignment, definitely enriches the laser filament physics; it will bring much more promising applications in ultrafast optics in the near future.

5. FILAMENTATION NONLINEAR OPTICS: RAMAN SPECTRAL SHIFT, FOUR-WAVE-MIXING AND SUPERCONTINUUM

Filamentation nonlinear optics was proposed to be a new way to do high intensity nonlinear optics in gases [106] in relation to efficient third harmonic generation [107, 108] and four-wave-mixing (4WM) [25, 109].

Since then, efficient generation of UV through the same 4WM scheme as [25] was reported in gases [110, 111]. The UV pulse energy was much higher than that from the hollow core fiber method while the alignment was considerably simpler since no fiber was used. Recently, broad band infrared supercontinuum generation through 4WM was reported [112, 113]. Terahertz (THz) pulses are generated and will be discussed in a separate section below. Also, a Raman type of spectral red shift of the pump wavelength (800 nm) was observed in air [114]. A brief description of these new developments (apart from THz) is given below.

5.1. Raman Type Spectral Shift

The spectra from inside the filament of a fs Ti-sapphire laser pulse in air was measured in the forward direction as shown in Fig. 20. The collimated laser pulse underwent free propagation and filamentation. The wedge was set at a near grazing angle on a movable table and partially reflected the pulse towards the integrating sphere followed by a spectrometer.

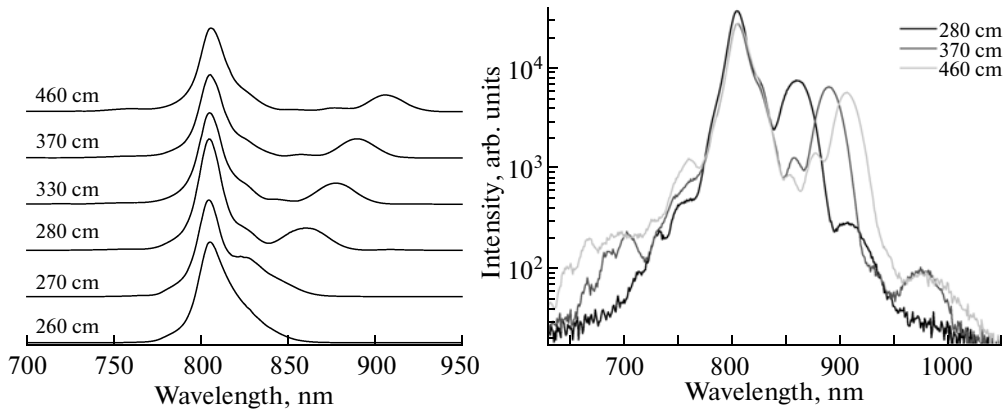


Fig. 21. Spectral red and blue shifts of a filamenting fs laser pulse as a function of the position inside the filament. The distances were measured from lens L2 in Fig. 20.

It was discovered [114] that the spectrum underwent strong continuous self-frequency red shift in air as the filament length increased. The filament started at 260 cm and ended at around 500 cm from L2. Before the filament is formed, there is no spectral shift. Figure 21 (left) shows the spectral shifts with a linear scale in the vertical axis. There is a new spectrum moving out from the peak spectral position towards the red side as the position of the detector (wedge + integrating sphere + spectrometer) moves through the filament in the propagation direction. Figure 21 (right) shows three spectra at three different positions in the filament using a log vertical scale. Both the Stokes (red) shift and anti-Stokes (blue) shift are evident.

When using argon gas, such shifts disappeared indicating that the shifts pertained to molecular gas. This suggests that the Raman effect would be the reason. Also, the measured continuous self frequency downshift during filamentation in air has a strong dependence on the length of the filament. It was explained in [114] that this phenomenon is similar to the observation of continuous Raman self-frequency down shifts in a fiber [115–118].

The first Stokes shift is due to rotational effect from N_2 (12 cm^{-1}) and O_2 (8.4 cm^{-1}) corresponds approximately to a wavelength shift of 1.5 and 1.1 nm, respectively. These Stokes shifts are much smaller than the initial spectral bandwidth of the laser pulse, and thus, we cannot resolve them. During filamentation, the cascaded Stokes shift occurred and the generated IR pulse is continuously shifted towards longer wavelength. Because the spectral bandwidth of the newly generated IR pulse is much wider than the first Stokes shift due to rotational effects from N_2 and O_2 , the low-frequency spectral components of the pulse, acting as a seed, can be amplified by Raman gain while the high-frequency spectral components of the same pulse work as a pump. This results in continuous self fre-

quency down shift along the propagation of the pulse inside the filament zone. In the case of a fiber, all pulses are confined inside the fiber core. In the present case of filamentation, we suspect that the Raman pulse, once created inside the filament, is phase-

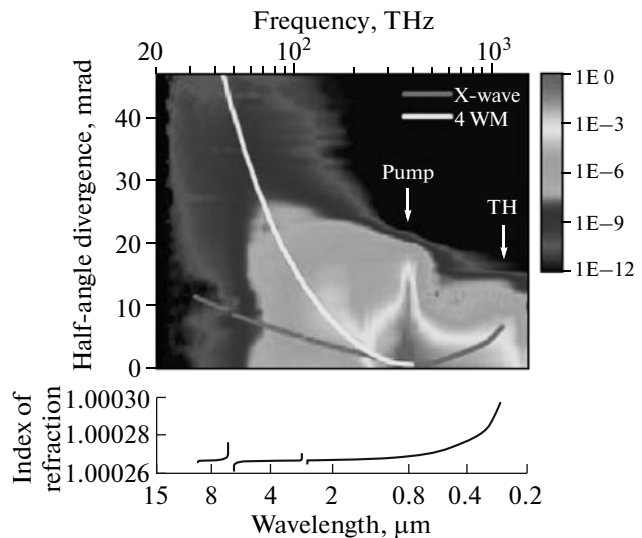


Fig. 22. (a) Angularly resolved spectrum generated during the filamentation in air by laser pulses having an energy of 60 mJ and a pulse duration of 42 fs. The horizontal axis is a logarithmic scale for the frequency. The false colors associated with the spectrum are related to the relative spectral intensity. The gray curve is the angular position of the CE according to the X-wave dispersion equation, and the white curve is the angular position of the infrared CE according to the off-axis 4WM process. The white arrows point out the central frequency of the pump pulse and its TH. (b) Linear refractive index of air calculated using a Sellmeier-type model for a pressure of 1 atm, a temperature of 15°C , and a relative humidity of 40%. Adapted with permission from [112] (© 2008 OSA), image courtesy of Théberge, Defence Research and Development Canada Valcartier.

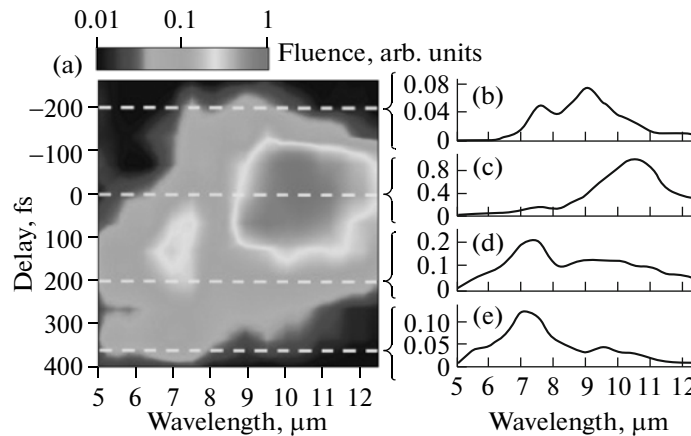


Fig. 23. (a) FIR spectrum generated during the cofilamentation in air of a 20-mJ NIR laser pulse and a 1-mJ SH laser pulses. The vertical axis is the relative delay between the pump pulses. A positive delay corresponds to the SH pulse in front of the NIR pulse and vice-versa for the negative delay. The zero delay was arbitrarily set to the optimum FIR energy. The false colors associated with the spectrum are related to the relative spectral fluence. The white dashed lines indicate the delay of the measured spectrum for (b) -200 , (c) 0 , (d) $+200$, and (e) $+365$ fs. Adapted with permission from [113] (© 2010 APS), image courtesy of Th  berge, Defence Research and Development Canada Valcartier.

locked to the pump pulse. Thus, the Raman pulse stays inside the filament (i.e., propagates together with the pump pulse inside the filament core) while undergoing cascaded Stokes shift. Once outside the filament core, linear diffraction would make the pulse intensity too weak to undergo further cascaded Stokes shift.

5.2. Ultra-Broad Band Supercontinuum Generation

Focusing the 800 nm pump pulse at 1.4 TW (60 mJ/42 fs) in air with a 4 m focal length concave mirror generating multiple filaments, ultra-broad band conical supercontinuum from ~ 200 nm to ~ 14 μm in the infrared was observed by Th  berge et al. [112]. The band width was so broad that five different types of spectrometers had to be used in different wavelength ranges. Longer wavelengths in the infrared have larger divergence at the Stokes side of the 800 nm pump while shorter wavelengths in the UV at the anti-Stokes side also have larger divergence, though not as large as that of the infrared. Figure 22 shows the measured angular resolved spectrum.

There are two principal physical processes responsible for the spectrum according to the authors. Towards the anti-Stokes side of the pump wavelength, normal conical emission or the so-called X-wave model [119] could explain the observation. In the Stokes side of the pump wavelength of up to 14 μm , a 4WM model involving 2 pump photons and one blue shifted photon at the anti-Stokes side of the pump explains well the large divergence.

5.3. Two-Color Filament Generation of Broadband Infrared Pulses

A special scheme [113] was designed in which an initially ~ 800 nm/38 fs laser pulse (diameter ~ 2.5 cm FWHM) was spectrally split into two pulses centered at around 795 and 813 nm by using a dichroic mirror. The latter had a smooth cutoff reflectivity at 805 nm. Thus, this mirror reflected a pulse centered at 795 nm while the transmitted a pulse centered at 813 nm. The transmitted 813 nm beam passed through a KDP doubling crystal. The resulting second harmonic (SH) pulse was focused collinearly with the reflected 795 nm near infrared (NIR) beam by a silver coated concave mirror (focal length: 1.5 m). The 795 nm pulse generated a filament in air. Before the filament, the pulse duration of the 20 mJ, 795 nm pulse was 50 fs at FWHM (transform limited), while the 1 mJ, SH pulse was positively chirped to 130 fs (transform-limited pulse duration was 70 fs). By changing the delay between the two pulses, pulses whose spectrum spanned from 5 μm in the infrared to beyond 12 μm in the far infrared (FIR) were generated. The spectral content varied with the delay time. Figure 23 shows the results.

The physical mechanism of generating these infrared pulses was analyzed using both the 4WM model and the photocurrent model. It was found that the 4WM model was the dominant physical process responsible for the above observation [113].

6. TERAHERTZ PULSE GENERATION IN FILAMENTS

This is another example of filamentation nonlinear optics. Very broadband THz pulses can be generated from filaments in air or other gases. Because of its

potential practical use in remote sensing of materials such as explosives, it is a popular subject of scientific and technical investigation.

6.1. General

Generation of intense terahertz (THz) pulses with large bandwidth from inside the filament in air is an active area of current research on THz science. Such broadband and rather powerful THz pulses would provide a new prospective tool for remote THz nonlinear optics and spectroscopy. THz pulses have the potential to combine safe-to-use high-resolution imaging and identification through spectroscopy; however, conventionally generated THz pulses from emitters such as semiconductor antennae or nonlinear crystals cannot propagate over a long distance in the atmosphere because of beam diffraction and strong attenuation due to water vapor. THz generation from femtosecond laser remote filamentation in gases, especially in air, is a promising alternative.

Single-cycle THz generation from a photo-induced plasma was first demonstrated by Hamster et al. in 1993 by focusing laser pulses with a power of 1 TW and a duration of 100 fs into He gas [120]. Since the emitter target is a gas, which is endlessly replenishable for each laser shot, there is no damage threshold limit at high intensities. The THz emission mechanism in their experiments was based on the space charge separation by the ponderomotive force generated by the optical beam [121], leading to a conical THz emission. Since then, other techniques have been used to generate stronger THz emission. Löffler et al. [122, 123] applied a DC bias to the plasma region that resulted in an order-of-magnitude increase in the THz field. At the same time, Cook and Hochstrasser [124] demonstrated a four-wave rectification method by focusing the fundamental wave (FW) and second-harmonic wave (SHW) of an amplified Ti:sapphire laser into air. More than 3 orders stronger THz signal has been recorded compared with only fundamental wave pump.

Since then, intense THz generations by the two-color pump have been investigated extensively [125–141]. THz electric field as high as 400 kV/cm [126] and a super-broadband THz spectrum up to 75 THz ($\lambda = 4 \mu\text{m}$) with μJ pulse energy [135] have been reported. Dai et al. [129] reported that THz emission from a two-color plasma filament could be amplified by another two-color filament in nitrogen gas through four-wave-mixing parametric processes during the plasma formation. Later, Chen et al. [130] demonstrated that the intensity of the terahertz wave increased as the number of two-color air plasmas increased. It was explained as the coherent superposition of the THz waves generated by each individual air plasma. The terahertz wave amplitudes from two-color filament can also be enhanced by more than eight times with an optimal aperture-limited pump

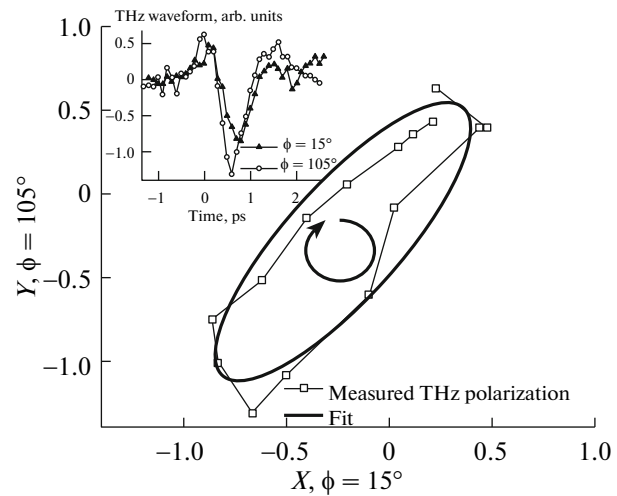


Fig. 24. THz polarization from single-color filament. Solid squares and solid curve are experimental data and simulation, respectively. The arrow indicated the rotating direction of the THz electric field vector. The inset shows typical experimental THz electric field waveforms obtained at two orthogonal directions (solid triangles: $\phi = 15^\circ$ and solid circles: $\phi = 105^\circ$).

laser beam [136]. Blanchard et al. reported more than 2 times increase in THz generation efficiency from two-color plasma by replacing the focusing lens with a gold off-axis parabolic mirror [140]. More recently, by using a converging lens followed by an axicon resulting in a tailored two-color laser filament in air, Manceau et al. reported significant THz pulse shortening from the uniform plasma strings [141]. For the physical mechanism of the generation of the THz pulses in a gas filament, two theoretical models have been reported. The first model frequently used to explain the THz emission is four-wave mixing [124–127] based on the third order nonlinearity. The second is the microscopic polarization model [134, 135], which has been suggested to interpret the underlying dynamics, attributing the THz emission to the free-electron drifting current driven by the combined field of the FW and its SHW. We call this photo-current model. Recently, Karpowicz and Zhang [137] interpreted the terahertz radiation in two steps based on the photo-current quantum mechanical model. First, terahertz photons are emitted due to the acceleration of the electron wave packet which is given a net dipole moment through the asymmetry introduced by the two-color field. Next, when these wave packets collide with neighboring atoms, they emit bremsstrahlung in the THz range. The theory can explain the single-cycle (broad-band) electric field and the following “echo” in the THz waveform. The polarization properties of THz emission have also been extensively investigated. The FWM model describes them reasonably well [127, 131–133]. Typical focal lengths used above for intense THz emission from two-color scheme are from 5 cm to 25 cm.

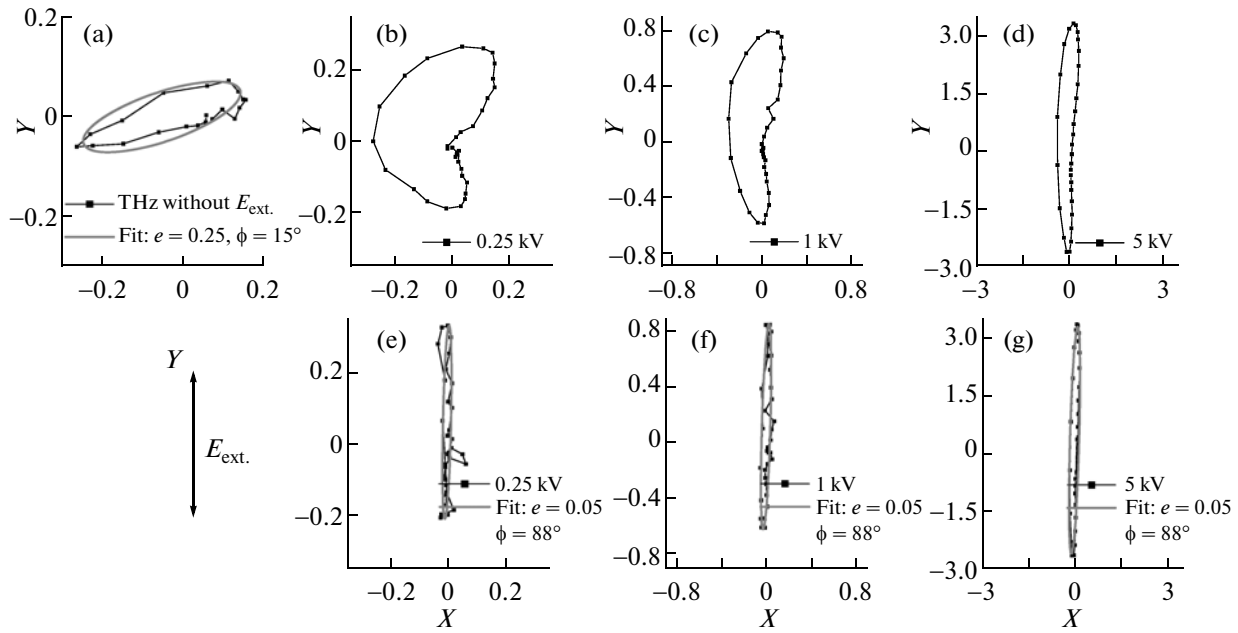


Fig. 25. Polarization trajectories of THz emission from a filament with a DC field of (a) 0, (b) 0.25, (c) 1, and (d) 5 kV/cm. THz polarizations in (e, f, g) were obtained at 0.25, 1, and 5 kV/cm by subtracting the waveforms without DC field, respectively.

The other important reason why THz generation from femtosecond laser induced plasma filaments in air recently attracts much attention [142–159] is that THz emission can be generated close to a remote target. This is because the onset of the filament to remote distances can be controlled, in principle, by the initial laser parameters: beam diameter, divergence and pulse duration, etc. Remote THz generation minimizes the importance of propagation issues as mentioned above. D’Amico et al. reported the first remote THz generation from the filaments induced by the FW of a Ti:sapphire based laser system at a distance of 30 m from the laser in 2007 [142]. A radially polarized forward conical emission was observed whose origin they attribute to a Cherenkov-type mechanism from the laser-pulse induced plasma wake. Their conclusion was based on the measurement obtained with a heterodyne detector (sensitive only to 0.1 THz with a bandwidth of 4 GHz).

Later, by using an electro-optic sampling (EOS) technique (sensitive to frequencies below 4 THz), it was demonstrated that the THz pulses in the forward direction of a filament are elliptically polarized [143, 144] as shown in Fig. 24. The physical mechanism is that filament induced birefringence in gases provides a phase delay between the two orthogonal components of the THz field, leading to an elliptically polarized THz emission.

6.2. External DC Electric Field Effect on THz from Single-Color Filaments

External electric fields were applied transversely [145, 146] and longitudinally [147] to single-color fil-

aments, leading to 3 orders enhancement of THz amplitude with 10 kV/cm external electric field [145]. In the case of transverse external electric field, the polarization of this enhanced terahertz signal was found to be collinear with the external DC field. The physical origin is that the external electric field separates the electrons and ions in the plasma filament, which results in a transverse current responsible for terahertz emission with polarization parallel to the direction of the applied external electric field [146]. Typical THz polarization trajectories are depicted in Fig. 25. Without external electric field, an elliptical THz polarization trajectory similar to the results in [143] was observed (Fig. 25a). In the presence of the external electric field, the THz emission changed its polarization trajectory with the increase of the applied electric field, Figs. 25b–25d. When the THz electric field obtained without external electric field was subtracted from the corresponding ones obtained with external electric field, the re-composed THz polarization trajectories were surprisingly uniform: linearly polarized along the orientation of the external electric field, as shown in Figs. 25e–25g. The total THz emission from a DC-biased single-color laser-induced filament could be decomposed into two independent processes: THz generation by the neutrals in the strong laser field inside the filament which is elliptically polarized [143] and THz induced by the externally applied electric field through acceleration of the free electrons from inside the filament which corresponds to a linearly polarized THz source [146].

By taking the Fourier transform of the THz fields, it is found that the central frequency of this linearly

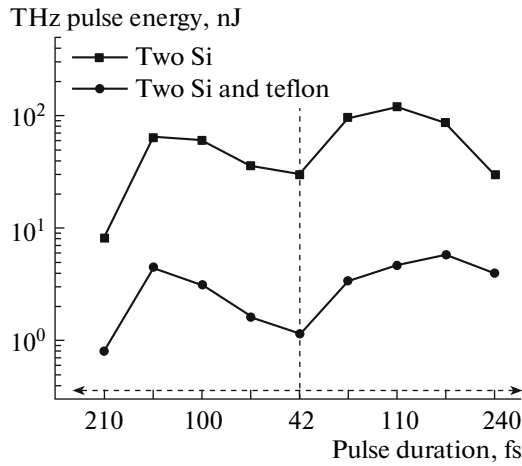


Fig. 26. Pump pulse duration dependence of THz emission with different filters in air. The vertical dashed line denotes the Fourier transform-limited pump pulse duration. Different filters indicate the different THz spectra measured.

800 nm separated by less than 3 ns, forming two overlapping filaments in air (so called bifilamentation) can generate 1 order of magnitude more intense THz emission than transient-Cherenkov THz emission [142] from the plasma filaments. The origin is attributed to the emission from a bimodal transmission line created by a pair of neighboring plasma filaments.

Two-color (FW and SHW) femtosecond laser filamentation in air was also investigated to generate high energy THz emission under loose focusing condition. Under a *fixed* high energy pump of 24 mJ from a Ti-sapphire laser, Wang et al. [149] observed more than 4 times enhancement of THz pulse energy by chirping the 42 fs transform limited pump pulse either negatively or positively to around 150 fs as shown in Fig. 26. The reason why there is an increase of THz pulse energy when the pulse is chirped is because, at the same energy, the transform limited pulse has a higher peak power. Thus, initial hot spots in the beam profile will self-focus earlier during the propagation. In the focusing geometry, multiple filaments will occur closer to the focusing optic (farther from the geometrical focus) in a zone of larger diameter. Filament competition [28] would occur in this case because the filaments are “far” apart from each other and would reduce the effectiveness of generating strong filaments. With longer chirped pulses, the peak power being lower, multiple filaments occur nearer the geometrical focus where the diameter of the beam is smaller. This smaller diameter favors multiple filaments cooperation (stronger constructive interference) resulting in stronger child-filaments [150], and hence more THz emission. When the chirp becomes even larger, the pulse duration becomes so long that the peak power decreases to the extent that the number

polarized THz field is independent of the external voltage. This means that it is the weak plasma inside the filament that is set into motion at its own characteristic plasma frequency. Because of intensity clamping, the plasma density is constant and hence the plasma frequency is constant. Apparently, this latter observation does not support the claim of THz amplification in an external electric field [145]. Only the characteristic plasma frequency is amplified.

6.3. Enhancement of THz from Filaments

Liu et al. [148] demonstrated that by sending a sequence of two femtosecond IR laser pulses at

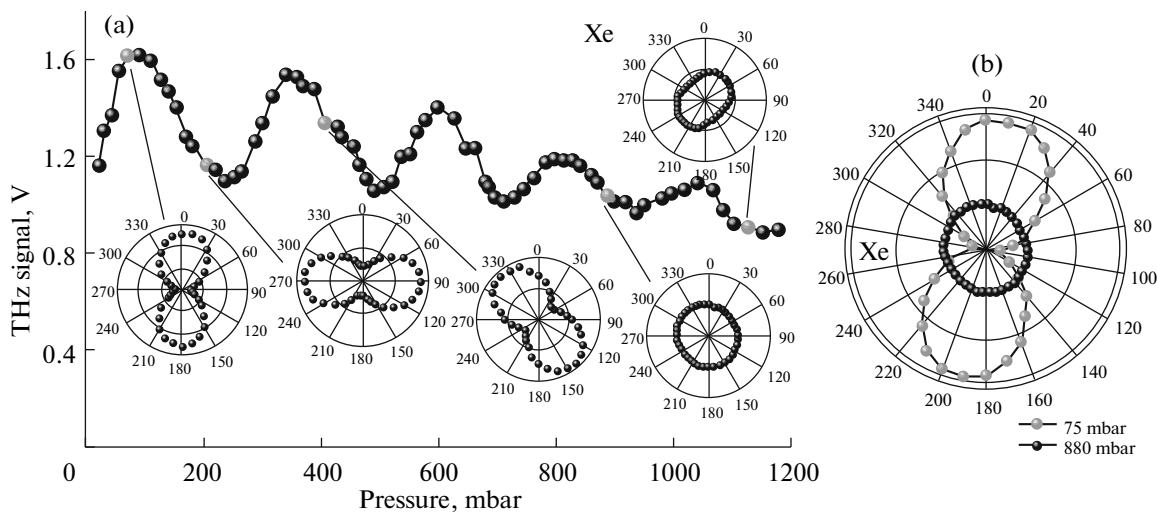


Fig. 27. THz power as a function of xenon gas pressure (a) and the linear polarization state of THz pulse at low pressure to the circular polarized THz at 880 mbar (b). The insets in (a) show the THz polarization states at different pressure levels. Adapted with permission from [151] (© 2010 OSA), image courtesy of J.-M. Manceau, Foundation for Research and Technology-Hellas (FORTH).

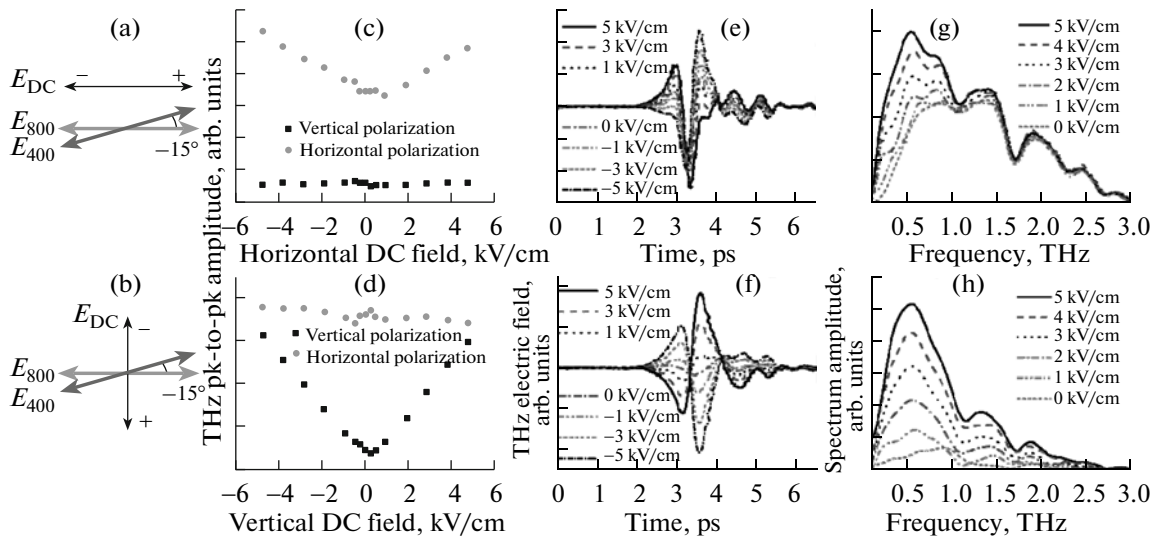


Fig. 28. THz peak-to-peak amplitude (c, d), waveform (e, f) and frequency spectra (g, h) from a two-color laser-induced filament in air with horizontal (a) and vertical (b) external DC field. The THz waveforms and frequency spectra are for the components polarized along to the direction of external DC field.

of strong filaments will reduce, and thus, decrease the THz signal.

6.4. Coherent Polarization Control of THz Pulses from Two-Color Filaments

By changing the optical phase between the FW and its SHW, the polarization of THz emission from two-color filaments in air can be coherently controlled when at least one of the optical pump pulses is elliptically polarized [138]. This phenomenon was simultaneously reported by Wen and Lindenberg [139] and Dai et al. [138] either through the positioning of the frequency doubling crystal along the laser propagation axis [139] or using an inline phase controller [138]. In particular, when both the FW and the SHW are circularly polarized, the THz polarization angle can be arbitrarily rotated by changing the phase between the FW and the SHW, with the THz amplitude kept constant [138]. More recently, Manceau et al. [151] demonstrated the THz polarization control via the accurate control of the surrounding gas pressure of two-color filaments. The change of gas pressure will induce a wavelength dependent change of refractive index, resulting in the relative phase change of the two laser fields. As expected, the polarization of the THz pulse is rotated as the pressure of the gas medium is changed in nitrogen gas. Beyond the rotation of the THz pulses' polarization, elliptically polarized THz pulses at different elliptical states and up to fully circular polarized THz pulses have been observed in xenon gas as shown in Fig. 27. Figure 27a shows the THz radiation as function of xenon gas pressure. The polarization rotation of THz pulse was observed by increasing the gas pressure. The linear polarization of THz pulse at low

pressure of 75 mbar was changed to circular polarization at high pressure of 880 mbar (Fig. 27b).

6.5. External DC Electric Field Effect on THz from Two-Color Filaments

More recently, the generation of THz emission from a DC-biased two-color femtosecond laser-induced filament in air was systematically investigated [152]. THz pulses were characterized using the EOS technique with the external DC field parallel (Fig. 28a) and perpendicular (Fig. 28b) to the FW polarization direction, respectively. THz peak-to-peak amplitudes as a function of the external DC field are shown in Figs. 28c and 28d. The external DC field could amplify only one THz component whose polarization is parallel to the direction of the external DC field. The higher the external DC field is, the stronger the THz emission is. The THz electric fields parallel to the DC field are depicted in Figs. 28e and 28f. The THz waveform can be modulated by controlling the external DC field. The corresponding Fourier spectra of THz emission are shown in Figs. 28g and 28h. Similar to the case of DC field biased single-color filament, the peak frequencies stay at around 0.54 THz when increasing the external DC field for both cases. The peak frequency without DC field is around 0.9 THz. These two different peak frequencies indicate two different generation processes, one induced by external DC field alone and the other only bichromatic excitation. Polarization plots similar to Fig. 25 were obtained which reconfirms the above claim [152]. Therefore, the total THz emission could be interpreted as a sum of two contributions. One is the linearly polarized THz component induced by the external DC field with polarization parallel to the

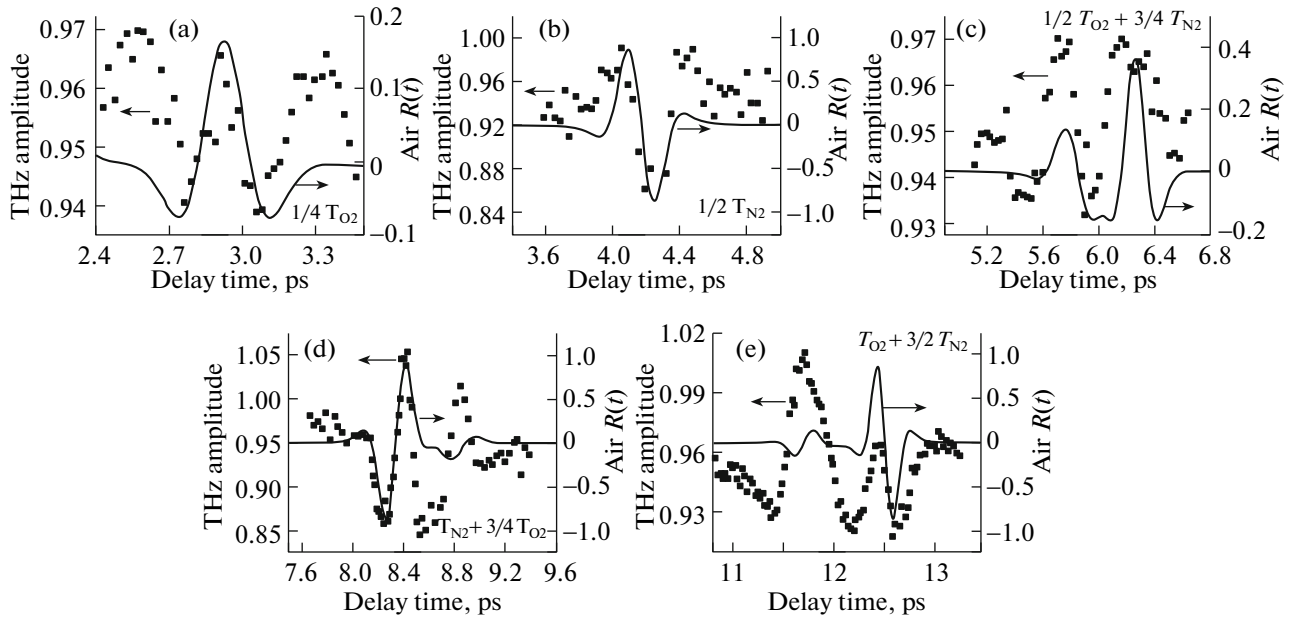


Fig. 29. Peak-to-peak: amplitude of THz electric field as a function of delay time around different air molecule revivals: (a) quarter revival of O_2 ; (b) half revival of N_2 ; (c) half revival of O_2 and three-quarter revival of N_2 ; (d) full revival of N_2 and three-quarter revival of O_2 ; (e) full revival of O_2 and one and a half revival of N_2 . Solid line in (a–e) is the calculated response function $R(t)$ of molecular Raman alignment in air (80% N_2 and 20% O_2).

direction of the DC field; it corresponds to the plasma frequency of the filament. The other is an emission from the two-color laser-induced filamentation due to the neutrals; i.e., 4WM.

However, depending on the external DC field polarity, the THz component parallel to the DC field was slightly asymmetric in Fig. 28c and a minimum was observed around +1 kV/cm. This small decrease of the THz amplitude, as compared to the case without DC field, could be attributed to partial destructive interference between the two THz sources. On the other hand, if the photocurrent [134] did partly contribute to the THz generation from the two-color pump pulses, the external DC field with positive polarity could cancel the free-electron drift at +1 kV/cm, and thus slightly decreases the total THz amplitude by leaving alone the contribution from the four-wave mixing. Since the THz emission from the electric current induced by an external DC field is mainly independent of the THz emission generated by the bichromatic excitation, it could be reasonably concluded that THz emission from the two-color filamentation is mostly due to the four-wave mixing process.

6.6. Molecular Alignment Effect on THz Emission from Filaments in Air

During the filamentation of femtosecond laser pulses in air, most of the molecules survive in the plasma filament due to weak molecular ionization

[27]. However, the laser pulses with clamped intensity of $\sim 5 \times 10^{13} \text{ W/cm}^2$ in the filaments are strong enough to align the neutral molecules through rotational Raman excitation, resulting in field-free periodic revivals. The typical revival periods of N_2 and O_2 molecules in air are 8.4 and 11.6 ps, respectively. Recently, a control of THz emission from bifilamentation of two FW pulses based on molecular lensing effect was characterized by a heterodyne THz detector, which is sensitive at 0.1 THz with a bandwidth of 4 GHz [153].

More recently, Wu et al. [154] and Wang et al. [155] reported the molecular alignment effect on THz emission from two-color filaments in air. Air molecules are pre-aligned by FW pulses [154] or a pair of two-color laser pulses [155]. In the latter case, the first pair of two-color pulses (800 nm/400 nm) prepared the filament. THz emission is generated by the second pair of two-color laser pulses. By tuning the delay time between the two pairs of two-color pulses, significant modulations of THz emission are observed around the air molecule revival time. Figure 29 show the peak-to-peak amplitudes of THz electric field as a function of delay time (dotted curves) and the calculated response function of rotational Raman process (solid curves). The delay times are set around the quarter revival of O_2 (Fig. 29a), the half revival of N_2 (Fig. 29b), the half revival of O_2 and the three-quarter revival of N_2 (Fig. 29c), the full revival of N_2 and three-quarter revival of O_2 (Fig. 29d), the full revival of O_2 and one and a half revival of N_2 (Fig. 29e).

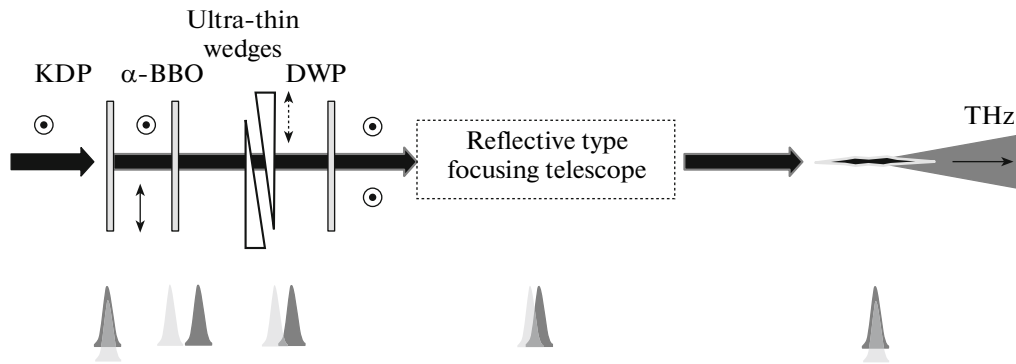


Fig. 30. Schematic setup for remote high energy THz generation. The bottom indicates the time sequence of the two color beams.

When the rotational Raman response function, $R(t)$, is >0 , the average molecular axis is parallel to the polarization of the exciting laser field and the refractive index change of the probe laser pulse and its SH is positive. When $R(t)$ is <0 , the average molecular axis is perpendicular to the polarization of the exciting laser field and the refractive index change of the probe laser pulse and its SH is negative. (See Section 8 for more discussion of such index change.) The refractive index change due to molecular alignment results in focusing or de-focusing of the probe beam and hence, in the changes of laser intensity and plasma density. For example, positive refractive index change corresponds to the increase of intensity and plasma density. Thus when $R(t) > 0$, the intensity of the FW and the SHW should slightly increase and the THz efficiency should increase and vice versa. Meanwhile, the positive refractive index change will increase the nonlinearity, $\chi^{(3)}$, and the negative refractive index change will decrease the nonlinearity. Generally, enhanced THz emission was observed when $R(t)$ is >0 and vice versa as depicted in Fig. 29. The observed phenomenon on the modulation of THz emission is attributed to molecular alignment induced refractive index change, resulting in the changes of the nonlinearity ($\chi^{(3)}$) in neutrals and laser intensities inside the filaments.

6.7. Remote High Energy THz Generation

For remote high energy THz generation, so far, two-color filamentation is strongly desired and is also challenging. Phase compensation between the two color beams is necessary and needs to be precisely controlled. One can simply set up a delay stage and a pair of ultra-thin wedges in one arm of the two-arm scheme (FW and SHW in each arm, respectively). However, fluctuation and mechanical instability is serious in the two-arm scheme especially for long distance experiments according to our experience. Recently, an inline phase compensation setup was reported by Zhang et al. [138, 156] to improve the stability. The setup in [138] together with a reflective-type telescope (Fig. 30) was used to remotely generate high

energy THz pulses in air [157] using high energy Ti-sapphire laser pulses.

In order to decrease the nonlinear effects inside the optics of the in-line setup and also considering the large pump beam size, optics with large aperture had to be used. For frequency doubling, a 0.5 mm thick KDP crystal with aperture >30 mm was chosen. When the FW and SHW with orthogonal polarizations pass through a birefringent crystal—X-cut α BBO, the FW will be delayed compared to the SHW (so-called negative delay). All the following optics and air will provide positive delays, which will result in the temporal overlap in the predetermined filament zone. A pair of ultra-thin wedges can precisely control the relative phase between the two color beams. A dual-wavelength wave plate (DWP) can rotate one of the polarizations by 90° and the other by 180° . The latter means that the polarization is un-affected. A reflective-type telescope can project the two-color filament at a long distance.

So far, a record of THz generation at a distance of 16 m is detected. Pulse energies more than 250 nJ in the frequency range below 5.5 THz are recorded using the current detection system with a pyroelectric energy meter by some of the authors of this review [157]. In the experiments, less than 30 mJ pump was used, which was limited by the self-focusing effect after the intense pump beam passes through the centimeter-thick α BBO crystal.

As an improvement, X-cut α BBO wedges combining the current α BBO crystal and ultra-thin wedges would be helpful. The current setup has a capability to generate THz radiation at few tens of meters away by carefully managing the delay between two color beams. In order to generate stronger THz emission at further distances, good pump beam quality, larger aperture optics and more sensitive detection will be more helpful. When an intense single-cycle THz pulse is applied on a plasma filament in air, THz radiation-enhanced emission of fluorescence (REEF) [160] from the nitrogen fluorescence from the filament was observed. The THz-enhanced fluorescence intensity

carries THz waveform information, which is ideal for standoff detection of THz pulse. For THz standoff detection, one can refer to some recent work [156, 161], which is out of the scope of this review.

7. BIREFRINGENCE INSIDE A FILAMENT IN AIR

7.1. Birefringence

When a linearly polarized fs laser pulse undergoes filamentation in air, the high intensity inside the filament will turn the normally isotropic medium into anisotropic during the short time when the filamenting laser pulse exists. If simultaneously, a second linearly polarized weak probe pulse propagates with the filament, it will experience this anisotropy through cross-phase-modulation (XPM). That is to say, in the “eyes” of the probe, the normally isotropic air medium becomes birefringent. The probe pulse would be guided by the filament, become elliptically polarized in general and would rotate inside the filament core [71, 10]. We explain this phenomenon as follows.

The anisotropy arises because inside the filament, the pump’s linear polarization induces a stronger polarization parallel to the field of the pump than that perpendicular to the pump field. The probe would experience this anisotropy through XPM. Thus, the probe would experience two different extra indices of refraction, Δn_{\parallel} and Δn_{\perp} , corresponding to the polarization components of the probe parallel and perpendicular to the pump polarization, respectively. From, for example, [10, 71],

$$\Delta n_{\parallel} = \frac{3\varepsilon_0}{4n_0} \operatorname{Re}(\chi_{xxxx}^{(3)}) |E_x^{\text{filament}}|^2, \quad (12)$$

$$\Delta n_{\perp} = \frac{3\varepsilon_0}{4n_0} \operatorname{Re}(\chi_{yyxx}^{(3)}) |E_x^{\text{filament}}|^2. \quad (13)$$

Here, x denotes the direction of the pump polarization and E_x^{filament} is the electric field of the pump inside the filament; y is the direction perpendicular to x , $\chi_{xxxx}^{(3)}$, $\chi_{yyxx}^{(3)}$ are the corresponding third order susceptibility tensors.

$$\chi_{ijkl}^{(3)} = \chi_{ijkl}^{(3)}(-\omega_i^{\text{probe}}; \omega_j^{\text{probe}}; \omega_k^{\text{filament}}; -\omega_l^{\text{filament}}), \quad (14)$$

$ijkl (= x, y)$ being directions of the electric fields of the corresponding frequencies ω . Since $\operatorname{Re}(\chi_{xxxx}^{(3)}) = 3\operatorname{Re}(\chi_{yyxx}^{(3)})$ in an isotropic medium [10, 78]

$$\Delta n_{\parallel} = 3\Delta n_{\perp}. \quad (15)$$

Thus, the parallel component of the probe propagates slower than the perpendicular component resulting in a phase difference between them. This phase difference is given by $(\Delta n_{\parallel} - \Delta n_{\perp})2\pi z/\lambda$, where λ is the probe

wavelength, z is the distance measured from the beginning of the filament whose length is l . It increases as the probe propagates through the filament’s length l . It is at the origin of changing the probe polarization from linear to elliptical with various degree of rotation in general.

Because both the extra indices Δn_{\parallel} and Δn_{\perp} are positive (Eqs. (12) and (13)), they give rise to the guiding of the probe by the filament in a way similar to the guiding by a fiber; however, it is more complicated because of the inequality of Δn_{\parallel} and Δn_{\perp} and because of the existence of plasma inside the filament. Consequently, the plasma part of the probe beam is guided and part of it is diffracted by the plasma [162]. This phenomenon was reviewed in [10].

7.2. Polarization Separator

Another result is what we call by polarization separator [91, 162] reviewed in [10]. It is related to initial molecular alignment (see next section) in air inside a filament after a delay of about 100 fs. By this time, the pump pulse is gone. The probe pulse would see only the aligned molecules. The parallel polarization component of the probe, being parallel also to the aligned molecular wave packet, would see an increase of index of refraction and would be guided inside the filament core even in the presence of the (weak) plasma. The perpendicular component would see a reduction in the index of refraction as well as the plasma. It would be diffracted out of the filament core into a ring pattern. The result is the separation of the initial full beam pattern into a central part with parallel polarization and an outer ring with perpendicular polarization.

7.3. Polarization Rotation

The rotation of the ellipse comes from the phase difference between the two orthogonal components. When the phase difference is π the effect is similar to a half-wave plate. Because the x - and y -components of the probe are generally not equal, the polarization is an ellipse rotated by twice the angle between the probe’s initial linear polarization axis and the pump’s linear polarization axis. The latter could be considered as the optic axis of the filament.

An experiment was done by setting the angle between a probe (400 nm/ \sim 50 fs/2.2 μ J) and the pump (800 nm/50 fs/0.85 mJ) polarizations at two arbitrary angles of 15° and 75° with respect to the pump polarization (defined as $\psi = 0^\circ$) in argon at one atmospheric pressure [163]. The reason for using argon was to look at only the electronic effect and avoid the molecular complications. The probe was superimposed on the pump; it passed through (hence sampling) only the filament core of the pump by collinearly focusing the two pulses into the gas. Using an analyzer to measure the polarization of the probe at the end of the filament, the result is shown in Fig. 31.

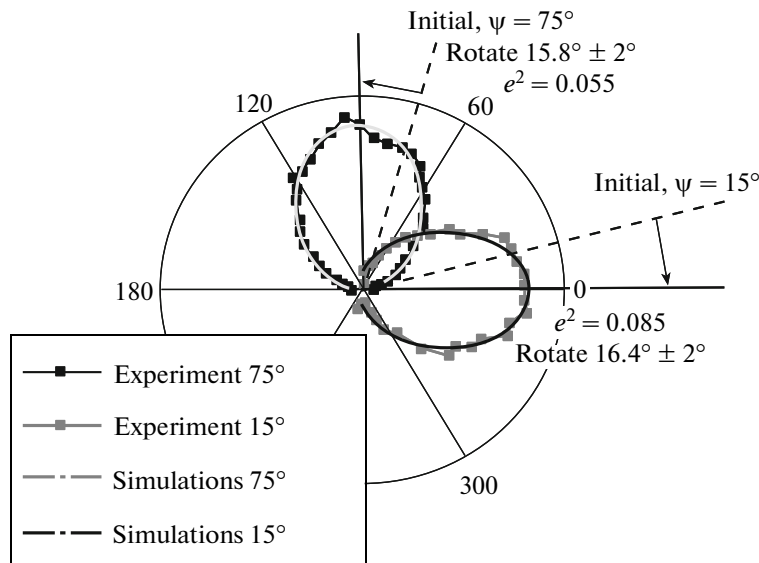


Fig. 31. Polarization analysis of the transmitted probe at the end of filament for a pair probe polarization angle ψ_{probe} at 75° (light grey circles, solid curve) and 15° (black circles, solid curve) with respect to the pump polarization defined as $\psi = 0^\circ$. Dash straight lines and solid straight lines correspond to probe polarization after the analyzer when the pump is turned off (initial) and on (final), respectively. XPM induced polarization rotations are marked by the blue arrows and characters.

The linear-to-elliptical transformation of a 400 nm fs-probe pulse in the birefringent filament in argon of an 800 nm linearly polarized fs-pump pulse was also studied numerically [164]. The rotation of the probe elliptical polarization was the largest in the high-intensity filament core. With propagation the rotated radiation diffracted outward by the pump-produced plasma. Figure 32 shows the numerical results of the rotation of the polarization of the probe.

An analyzer was used to measure the probe's polarization change. The transmission of the analyzer crossing the probe's polarization was a maximum at the pump-probe angle of 45° and gave equal values for each pair of angles symmetrically situated at both sides of the maximum. This prediction was confirmed experimentally as shown in Fig. 33.

8. MOLECULAR ALIGNMENT IN A FILAMENT AND REVIVAL

8.1. Preface

Recent experiments provide enticing evidence for the potential of alignment to introduce an intriguing range of novel applications of laser filamentation. Thus, for instance, it was experimentally found that alignment can increase the length of the plasma channel generated in the wake of the filament [104], modify the filament-generated supercontinuum [99], give rise to shock X-waves in the filament and tune their properties [88], control the wavelength of a few-cycle pulse [82], and, interestingly, modulate inter-filament interactions [73]. Equally inviting are the experiments of

[91], where it is shown that nonadiabatic alignment can serve as a polarization separator, the results of [162], where the ability of a filament in an aligned medium to affect ultrafast birefringence was illustrated, the work of [165], where the time-modulations of the refractive index caused by alignment was measured and computed, and the recent work of [166], where the interplay between laser alignment and population trapping in a filament was explored.

In order to understand, and hence also to control, these and other phenomena, it is important to first understand the concepts and mechanism responsible for nonadiabatic alignment. This is the goal of the present section. We begin in Subsection 8.2 with a discussion of the qualitative physics underlying intense laser alignment, noting the roles of the aligning field parameters and the material system properties. In Subsection 8.3 we briefly review the theoretical and experimental methods currently being used to quantify alignment, and in Subsection 8.4 we discuss nonadiabatic alignment and population trapping in the context of laser filamentation. We conclude in Subsection 8.5 with a discussion of opportunities and avenues for future research on filamentation from aligned media.

8.2. Basic Concepts

Essentially, the alignment of an ensemble of molecular rotational states by a light pulse is a phenomenon of the excitation of a wave packet. A rotational wavepacket is analogous in some respects to an electronic (Rydberg) wavepacket or a vibrational wavepacket.

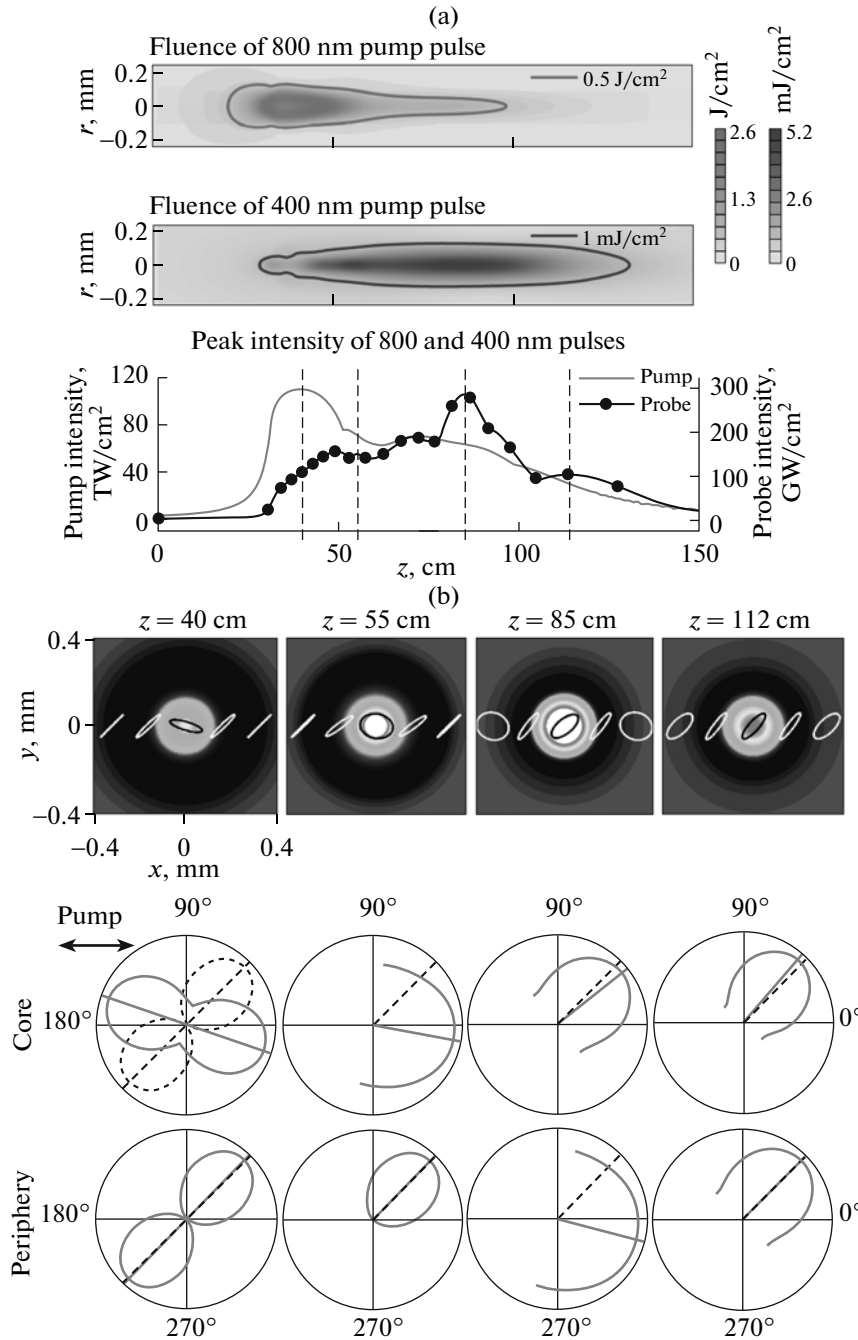


Fig. 32. (a) Simulated fluences and peak intensity of the pump and the probe pulses co-propagating in 1 bar argon. The initial pump-probe angle is $\psi = 45^\circ$, the pump direction is 0° . Dashed vertical lines on the intensity plot indicate the positions $z = 40, 55, 85, 112$ cm, where the polarization is analyzed in (b) (each of the four columns corresponds to one z -position). (b) The upper row shows the polarization ellipses at several radial positions across the beam plotted over the transverse fluence distribution. The polar plots show the probe fluence (solid curve) in the beam center (radius 100 μ m, the middle row) or the periphery ring (320–370 μ m, the lower row). The dashed line is the probe polarization direction at $z = 0$.

One gains localization in the coordinate space (here the angle) by populating a broad superposition in the conjugate quantum number space (here the angular momentum quantum number). The superposition is localized (here it is aligned) but it will dephase in the

course of time under field free conditions (even if coherence is maintained) because the energy level spacings are not equal.

In this section we provide a qualitative picture of coherent laser alignment. We start by discussing the

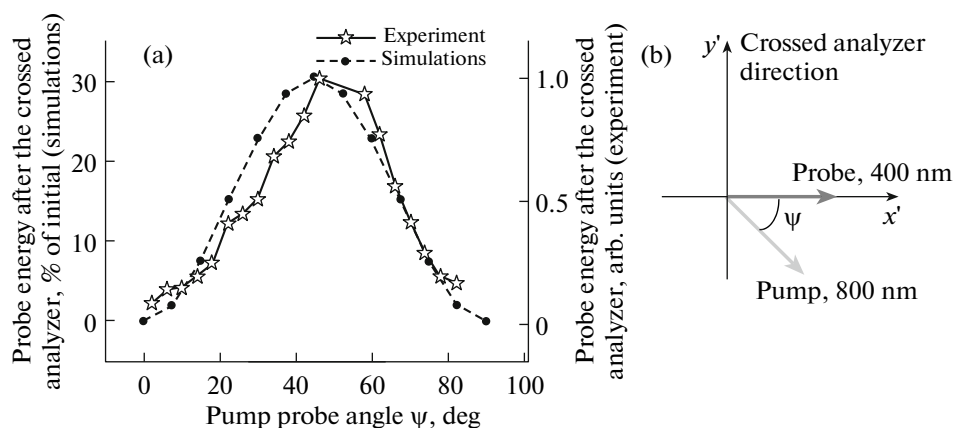


Fig. 33. (a) The experimentally obtained (stars) and simulated (dashed curve) energy of the overall probe beam transmitted by the crossed analyzer at the end of the filament for the pairs of pump-probe angles $\psi = (\alpha; 90^\circ - \alpha)$. (b) The initial pump and probe directions.

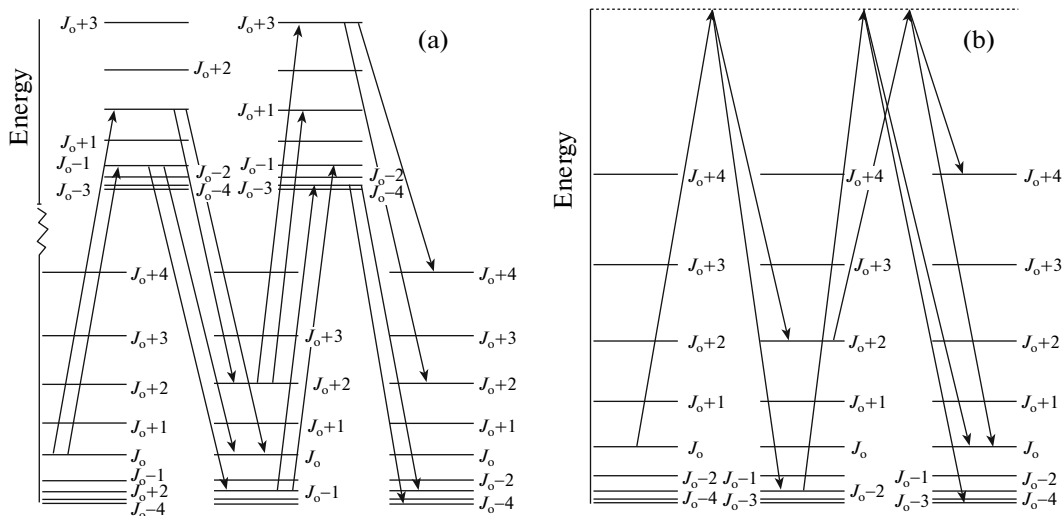


Fig. 34. (a) Rotational excitation in near-resonance laser fields. In the weak field limit, electric dipole selection rules restrict the degree of rotational excitation to $|\Delta J| = 0, 1$. In a moderately intense field, by contrast, Rabi-type sequential transitions between the two electronic manifolds are allowed, each of which is accompanied by the exchange of another unit of angular momentum between the molecule and the field, leading to the population of a rotationally broad wavepacket. (b) Rotational excitation in nonresonant laser fields. At far-off resonance frequencies, well below electronic transition frequencies, rotational excitation takes place via Raman type, $|\Delta J| = 0, 2$, transitions, resulting again in a population of a broad rotational wavepacket.

mechanism underlying laser alignment within a quantum mechanical framework (Subsection 8.2.1) and noting the role played by the field and system parameters (Subsection 8.2.2). To that end we focus on the simplest case scenario of a linear, isolated rigid rotor subject to a linearly polarized field. In Subsection 8.2.3 we discuss briefly the possibility of orienting molecules with intense pulses, and in the last subsection we consider the extension of alignment from isolated molecules to dissipative media.

8.2.1. Rotational excitation and coherent alignment. Consider a rigid, linear molecule subject to a linearly polarized laser field whose frequency is tuned

near resonance with a vibronic transition. In the weak field limit, if the system has been initially prepared in a rotational level J_0 , electric dipole selection rules allow transition to J_0 and $J_0 \pm 1$ in the excited state. The interference between these levels gives rise to a mildly aligned excited state population, depending on the type of the dipole transition, parallel or perpendicular to the laser's linear polarization. At nonperturbative intensities, the system undergoes Rabi-type oscillations between the two resonant rotational manifolds, exchanging one unit of angular momentum with the field on each transition. Consequently, a rotationally-broad wavepacket is produced in both states. The asso-

ciated alignment is considerably better than the weak-field distribution, as it arises from the interference of many levels [167, 168] (Fig. 1a). The degree of rotational excitation is determined by either the pulse duration or the balance between the Stark shift that depends on the laser intensity and the detuning from resonance. In the limit of a short, intense pulse, $\tau_{\text{pulse}}^2 < (B_e \Omega_R)^{-1}$, the number of levels that can be excited is roughly the number of cycles the system has undergone between the two states, $J_{\text{max}} \sim \tau_{\text{pulse}} / \Omega_R^{-1}$, where τ_{pulse} is the pulse duration, B_e is the rotational constant, Ω_R is the Rabi coupling and Ω_R^{-1} is the corresponding period. In the case of a long, or lower intensity pulse, $\tau_{\text{pulse}}^2 > (B_e \Omega_R)^{-1}$, the degree of rotational excitation J_{max} is determined by the accumulated detuning from resonance, i.e., by the requirement that the Rabi coupling be sufficient to access rotational levels that are further detuned from resonance as the excitation proceeds, $J_{\text{max}} \sim \sqrt{\Omega_R / 2B_e}$. A quantitative discussion is given in [169].

A rather similar coherent rotational excitation process takes place at far-off resonant frequencies, well below electronic transition frequencies. In this case a rotationally-broad superposition state is produced via sequential Raman-type ($|\Delta J| = 0, 2$) transitions, (Fig. 34) the system remaining in the ground vibronic state [169].

The qualitative criteria determining the degree of rotational excitation remain as discussed in connection with the near-resonance case. In the case of near-resonance excitation, however, the Rabi coupling is proportional to the laser electric field, whereas in the case of nonresonant excitation it is proportional to the intensity, i.e., to the square of the field, due to the two-photon nature of the cycles. Consequently, much higher intensities are required to achieve a given degree of alignment, as expected for a non-resonant process. On the other hand, much higher intensities can be exerted at non-resonant frequencies, as undesired competing processes scale similarly with detuning from resonance. It is interesting to note that the dynamics of rotation excitation and the wavepacket properties are essentially identical in the near and non-resonance excitation schemes. In fact it is possible to formally transform the equations of motion corresponding to one case into those corresponding to the other [169]. In reality the near- and the non-resonant mechanisms may act simultaneously, with the former typically corresponding to a vibrational resonance [170]. The degree of spatial localization and the time-evolution of the alignment are essentially independent of the frequency regime; they are largely controlled by the temporal characteristics of the laser pulse, as illustrated in the following subsection.

8.2.2. Time evolution. The simplest case scenario is that of alignment in a continuous wave (CW) field, proposed in [171, 172], where dynamical considerations play no role. In practice, intense field experiments are generally carried out in pulsed mode, but, provided that the pulse is long with respect to the rotational period, $\tau_{\text{rot}} = \pi \hbar / B_e$, each eigenstate of the field-free Hamiltonian is guaranteed to evolve adiabatically into the corresponding state of the complete Hamiltonian during the turn-on, returning to the original (isotropic) field-free eigenstate upon turn-off [169]. Formally, the problem is thus reduced to alignment in a CW field of the peak intensity. The latter problem is formally equivalent to alignment of nonpolar molecules in a strong DC field, since the oscillations of the laser field at the light frequency can be eliminated at both near- and non-resonance frequencies [167, 169]. Thus, in the long pulse limit, $\tau_{\text{pulse}} \gg \tau_{\text{rot}}$, laser alignment reduces to an intensively studied problem that is readily understood in classical terms, namely the problem of field-induced pendular states [173, 174]. The Stark shift gives rise to a potential well for the angular motion, which can readily exceed the thermal energy and convert the free rotation of molecules into small amplitude librations about the polarization vector. In this limit, the sole requirement for alignment is that the Rabi coupling be large compared to the rotational energy of the molecules at a given rotational temperature. Intense laser alignment in the CW limit (termed adiabatic alignment) grew out of research on alignment and orientation in DC fields, and is very similar to DC alignment conceptually and numerically. It shares the advantage of DC field alignment of offering an analytical solution in the linear, rigid rotor case [171]. It shares, however, also the main drawback of DC field alignment, namely, the alignment is lost once the laser pulse has been turned off. For applications one desires field-free aligned molecules.

Short-pulse-induced alignment (termed nonadiabatic, or dynamical alignment) was introduced [167] at the same time as the adiabatic counterpart and is similar in application but qualitatively different in concept. This field of research grew out of research on wavepacket dynamics and shares several of the well-studied features of vibrational and electronic wavepackets while exhibiting several unique properties (*vide infra*). A short laser pulse, $\tau_{\text{pulse}} < \tau_{\text{rot}}$, leaves the system in a coherent superposition of rotational levels that is aligned upon turn-off, dephases at a rate proportional to the square of the wavepacket width in J -space, and subsequently revives and dephases periodically in time. As long as coherence is maintained, the alignment is reconstructed at predetermined times and survives for a controllable period. As with other discrete state wavepackets of stable motions, all observables obtained from the wavepacket are periodic in the full revival time, given, in the case of rotational wavepackets, by the rotational period τ_{rot} . Interest-

ingly, under rather general conditions, the alignment is significantly enhanced after turn-off of the laser pulse [168]. The origin of the phenomenon of enhanced field-free alignment is unraveled in [168] by means of an analytical model of the revival structure of rotational wavepackets.

The first experiment to realize the prediction of field-free, post pulse alignment was reported in 2001 [175]. During the past decade, a large number of quantitative experiments that probe and utilize nonadiabatic alignment have been published (see also Section 4 and 7), of which the ones most relevant to laser filamentation are discussed in the following sections. In the ultrashort pulse limit, where the interaction is an impulse as compared to rotations, the dynamics following immediately the laser pulse is again readily understood in classical terms [168]. Here the pulse imparts a “kick” to the molecule, which rapidly transfers a large amount of angular momentum to the system and gives rise to alignment only after the turn-off. The molecule is rotationally frozen during the interaction but the sudden “kick” is encoded in the wavepacket rotational composition and gives rise to alignment upon turn-off. The subsequent long time dynamics, by contrast, exhibit strongly quantum mechanical dephasing and rephasing dynamics that does not have a classical analog. At very low rotational temperatures, the revival structure is rich and dense, differing qualitatively from the generic revival structures of bound state wavepackets [176]. As the rotational temperature increases, however, the structure simplifies drastically. At each multiple of the rotational period the initial alignment is precisely reconstructed. At half the period the molecules align perpendicular to the field. Depending on the spin statistics of the molecule studied, one observes features (termed fractional revivals) also at other fractions of the rotational period.

A third mode of alignment is introduced in [177] in the context of simultaneous alignment and focusing of molecular beams, potentially an approach to nanoscale surface processing [178]. A route to that end is provided by the combination of long turn-on with rapid turn-off of the laser pulse. During the slow turn-on, the isotropic free rotor eigenstate evolves into an eigenstate of the complete Hamiltonian—an aligned many— J superposition—as in the long-pulse limit. Upon rapid turn-off the wavepacket components are phased together to make the full Hamiltonian eigenstate but now evolve subject to the field-free Hamiltonian. The alignment dephases at a rate determined by the rotational level content of the wavepacket (hence the intensity, the pulse duration and the rotational constant), and subsequently revives. At integer multiples of the rotational period, $t = t_0 + n\tau_{\text{rot}}$, t_0 being the pulse turn-off, the fully interacting eigenstate of the complete Hamiltonian attained at the pulse peak is precisely reconstructed and the alignment characterizing the adiabatic limit is transiently available under

field-free conditions. Experimental realization of field-free alignment via the combination of slow turn-on with rapid turn-off was reported in [179].

8.2.3. Molecular orientation. A purely alternating current (AC) electromagnetic field polarized along the (say) space-fixed z -axis preserves the symmetry of the field-free Hamiltonian with respect to $z \rightarrow z$ (by contrast to a DC electric field that defines a direction, as well as an axis, in space); it aligns, but cannot orient molecules. The motivation for augmenting laser alignment to produce orientation comes from the field of stereochemistry, where orientation techniques have proven to make a valuable tool for elucidating reaction mechanisms [180, 181]. Several different methods have been proposed to that end [182, 183], two of which have been also tested in the laboratory [184, 185].

Within the method of [182], an intense laser field is combined with a relatively weak DC electric field, with the former serving to produce a broad superposition of J -levels via the nonlinear polarizability interaction and the latter providing a means of breaking the $z \rightarrow z$ symmetry. This approach is applied in [184] to orient HXeI, and in [186, 187] to orient OCS molecules. An alternative approach, advanced by several groups, takes advantage of the natural asymmetry of half-cycle pulses to orient molecules. Substantial experience has been gained in recent years in optimizing the ensuing orientation and manipulating its temporal characteristics by different control schemes [188–192]. A third method, which likewise received significant attention [185, 193–195], exploits the possibility of breaking the spatial $z \rightarrow z$ symmetry through coherent interference, e.g., by two color phase-locked laser excitation or by combining the fundamental frequency with its second harmonic. (The second harmonic is often taken to be resonant with a vibrational transition but a nonresonant variant of the same procedure has also been suggested [183].)

8.2.4. Alignment in dissipative media. The foregoing discussion has been restricted to the limit of isolated molecules, corresponding to a molecular beam experiment, where collisions do not take place on the time-scale of relevance and coherence is fully maintained. This limit applies to the vast majority of alignment studies reported to date. In a laser filament, however, the pressure is typically significant and hence the molecules suffer collisions and, in the course of time, gradually lose their relative phase relations. Since the time scales of interest are typically short, and since the medium is only mildly dissipative, the isolated molecule description is often qualitatively correct, depending on the experimental parameters. Rigorously, however, dissipation need be considered (see Subsection 8.3).

Alignment subject to dissipative media, where collisions give rise to decoherence and population relaxation on relevant time-scales, is also fundamentally

interesting. First, one can show [196] that the unique coherence properties of rotationally-broad wavepackets provide a sensitive probe of the dissipative properties of the medium. In particular, it is found that the experimental observables of alignment disentangle decoherence from population relaxation effects, providing independent measures of the relaxation and decoherence dynamics that go beyond rate measurements. Second, we expect laser alignment to become a versatile tool in chemistry, once the effects of dissipative media on alignment are properly understood.

Reference [196] explores the evolution of nonadiabatic alignment in dissipative media within a quantum mechanical density matrix approach, illustrating both the sensitivity of rotationally broad wavepackets to the dissipative properties of the medium and the possibility of inhibiting rotational relaxation, so as to prolong the alignment lifetime, by choice of the field parameters. A classical study of alignment in a liquid is provided in [197]. The application of intense laser alignment in solutions to control charge transfer reactions is illustrated in [198]. Experimentally, nonadiabatic, intense pulse alignment in the dense gas environment has been probed in several studies. A particularly quantitative study is provided in [199], which compares the alignment measured in rotationally-cold molecular beam environments with that obtained in the dense gas medium.

Our discussion so far has been limited to linear systems, which are the ones of relevance to laser filamentation studies at present. We note in Subsection 8.5 that the case of nonlinear, in particular asymmetric, rotors offers new and interesting physics; see [200].

8.3. Theoretical and Experimental Methods

In this section we discuss several of the commonly used approaches to observe nonadiabatic laser alignment, experimentally (Subsection 8.3.1) and numerically (Subsection 8.3.2).

8.3.1. Experimental approaches. The most common way to probe nonadiabatic (and adiabatic) molecular alignment is through femtosecond pump-probe Coulomb explosion fragment ion imaging. Nonadiabatic alignment was observed in I_2 , [175] and nonadiabatic orientation was achieved in CO using a 2 color pump laser field and a single color pump field [201]. In a typical experimental scheme to observe nonadiabatic alignment, a first femtosecond laser pulse (pump) prepares a molecular rotational wavepacket. The periodically aligned molecules are then multiply ionized by a second, more intense, time-delayed laser pulse (probe). The doubly- or highly-charged molecular ions then dissociate rapidly through Coulomb explosion and the final momentum of each ionic specie is revealed through a position sensitive time-of-flight ion mass spectrometer. For simple molecules, the molecular configuration of the precu-

rior state (bond lengths and 3D spatial orientation) prior to the dissociation can often be reconstructed from classical mechanics (Coulomb's law), recovering the alignment sense and quality as well as the fascinating femtosecond dynamics of the different ions. A noteworthy example is the ultrafast hydrogen migration studied in [202, 203]. In several laboratories, coincidence detection of ions, imposing the total momentum conservation for the fragments, has been used to make sure that all fragments come from the same molecule and to identify unambiguously competing dissociation pathways [204–206]. For detailed discussions of the state-of-the-art of Cold Target Recoil Ion Momentum Spectroscopy (COLTRIMS) detectors, see [207, 208].

If the medium density is sufficiently high, the refractive index modulation Δn caused by the molecular alignment can be probed by a second short laser pulse in an all-optical measurement. This approach is particularly relevant in the case of filamentation, where the medium pressure is high and hence ion imaging becomes impossible. Thus, instead of measuring ions under ultra-high vacuum conditions, the measurements are performed directly on the light, employing well established optical methods (interferometry, polarization optics, etc.) and photonic detectors such as photomultiplier tubes, CCD cameras and spectrometers. This approach can be used as long as the molecular alignment induces a macroscopic phase modulation $\Delta\phi$ that can be measured. (See Section 4 and Subsection 8.4 for some examples.) The condition is that $\Delta\phi$ should not be vanishingly small compared to π rad. Typically, pressures (p) of a few torrs to a few atmospheres are used for practical interaction lengths L ranging from micrometers to meters. ($\Delta\phi \propto \Delta n L$ and $\Delta n \propto p$). The actual optical phase modulation measurements of a weak probe pulse induced by molecular alignment can be implemented in several ways. For instance, spectral interferometry [209, 210], polarization gating [162, 211], spatial [212] and spectral modulation [86, 83, 165, 213] were used to observe alignment.

A novel approach involving electron diffraction was demonstrated in [214]. In this work, a laser-synchronized 4-ps electron pulse was used to probe selectively aligned $C_2F_4I_2$ molecules undergoing dissociation. By imaging the electron diffraction pattern for several delays between the UV pump and the electron probe pulse, the authors could observe the alignment and its picosecond timescale decay through the azimuthal dependence of the electron diffraction pattern.

Monitoring the laser induced high harmonic emission spectra is also an indirect way to observe adiabatic [215] and nonadiabatic [216] molecular alignment, and one that is compatible with high pressure. High harmonic generation from aligned molecules is a young but intensively studied subject, and its information content remains the topic of scientific debate

[217–219]. It has been illustrated, however, that harmonic signals convey unique information regarding rotational wavepacket dynamics [220].

8.3.2. Numerical approaches. In the isolated molecule limit, nonadiabatic alignment is most commonly described by nonperturbative solution of the time-dependent Schroedinger equation subject to the complete Hamiltonian $H = H_0 + H_{\text{int}}$. Here, H_0 is the field free Hamiltonian and H_{int} is the interaction term. Within the (almost uniformly applied) rigid rotor approximation, H_0 reduces to the rotational Hamiltonian, and in the (most commonly considered) far-off-resonance limit H_{int} is the induced dipole Hamiltonian. In the simplest case scenario of a linear, rigid, isolated molecule subject to a linearly polarized, far-off-resonance field, $H_0 = \hbar B_e \hat{J}^2$ and $H_{\text{int}} = -1/4\epsilon^2(t)\Delta\alpha \cos^2\theta$, where B_e is the rotational constant, \hat{J}^2 is the angular momentum squared operator, $\epsilon(t)$ is the pulse envelope, the polarizability anisotropy is defined in terms of the components of the molecular polarizability tensor as $\Delta\alpha = \alpha_{\parallel} - \alpha_{\perp}$, and θ is the polar Euler angle (the angle between the molecular axis and the field polarization direction in the present context). The general forms of H_0 and H_{int} are derived in [200].

Given the complete Hamiltonian H , the time-dependent Schroedinger equation is typically solved by expanding the wavepacket in the complete set of eigenstates of H_0 ,

$$|\Psi_{J,M}(t)\rangle = \sum_J C_{J,M}^J(t) |JM\rangle, \quad (16)$$

where $\langle\theta, \phi|JM\rangle = Y_{JM}(\theta, \phi)$ are the spherical harmonics, and propagating a set of coupled differential equations for the expansion coefficients $C_{J,M}^J(t)$. In Eq. (16) J is the total angular momentum quantum number, J_i is its initial value, and M is the magnetic quantum number. The azimuthal Euler angle, ϕ , is the angle of rotation about the field vector in the present context. Given the time-dependent wavefunction $\Psi(t)$ as a function of time, all observables of interest can be computed in a nonperturbative, fully quantum mechanical fashion. A common measure of the degree and time-evolution of the alignment is the expectation value of $\cos^2\theta$, computed as $\langle\Psi(t)|\cos^2\theta|\Psi(t)\rangle$. Up to a constant, $\langle\cos^2\theta\rangle$ is proportional to the second moment of the rotational distribution, hence it's common use as a measure of the alignment. We remark, however, that this measure does not convey all the information that is available in the rotational wavepacket and is sensitive only to second order interferences.

In the context of laser filamentation, where the pressure is not negligible and collisions take place on time-scales of relevance, a density matrix approach is

appropriate. Accordingly, we expand the density operator in terms of the rigid rotor eigenstates as $\hat{\rho}(t) = \sum_{J,M,J',M'} \rho_{JM J'M'}(t) |JM\rangle\langle J'M'|$. The time evolution of the elements of the density matrix is given by the quantum Liouville equation, and within a multi-level Bloch model for the dissipative operator, they obey the following equation of motion:

$$\begin{aligned} \frac{d\rho_{JM J'M'}(t)}{dt} = & -\frac{i}{\hbar} \left\{ (\epsilon_J - \epsilon_{J'}) \rho_{JM J'M'}(t) \right. \\ & - \Omega_R(t) \sum_{J_1} [V_{JM J_1 M_1} \rho_{J_1 M_1 J'M'}(t) \delta_{MM_1} \\ & \left. - V_{J_1 M_1 J'M'} \rho_{JM J_1 M_1}(t) \delta_{M'M_1}] \right\} \\ & - \left\{ \sum_{J_1 M_1} \frac{1}{2} (K_{JM J_1 M_1} \rho_{JM J'M'}(t) + K_{J'M' J_1 M_1} \rho_{JM J'M'}(t)) \right. \\ & \left. - \delta_{JJ'} \delta_{MM'} 2K_{J_1 M_1 J M} \rho_{J_1 M_1 J_1 M_1}(t) \right. \\ & \left. + (1 - \delta_{JJ'} \delta_{MM'}) \gamma_{JM J'M'}^{(pd)} \rho_{JM J'M'}(t) \right\}, \end{aligned} \quad (17)$$

where $\Omega_R(t) = 1/4\Delta\alpha\epsilon^2(t)$, $V_{JM J'M'} = \langle JM|\cos^2\theta|J'M'\rangle$, the dependence on the initial rotational quantum number is omitted to avoid cluttering the notation, and we note that optical transitions conserve M . The population transition rates between states $|JM\rangle$ and $|J_1 M_1\rangle$ are given by $K_{JM J_1 M_1}$ with $K_{JM J_1 M_1} = J M_1 = M = 0$ and $\gamma_{JM J'M'}^{(pd)}$ is the rate of pure dephasing of the $|JM\rangle\langle J'M'|$ coherence.

In terms of the reduced density operator, $\hat{\rho}(t)$, the expectation value of $\cos^2\theta$ is given as $\langle\cos^2\theta\rangle = \text{Tr}\{\cos^2\theta \hat{\rho}(t)\}$. We remark that $\langle\cos^2\theta\rangle$ is sensitive only to rotational coherences and rotational relaxation. The diagonality of the operator $\cos^2\theta$ with respect to all quantum numbers except for the angular momentum quantum number J follows from its dependence on a single coordinate, the polar Euler angle θ that is conjugate to J (in a rough sense). It thus disentangles the effects of J -changing collisions from those of purely M -changing collisions, and, in case a rovibronic wavepacket is excited, also from the effects of vibrational and electronic relaxation and decoherence. Numerical examples along with experimental data are given in the next section.

8.4. Nonadiabatic Alignment in the Context of Laser Filamentation

In a filamentation process in gases, there are two major observables as a consequence of the molecular alignment on the laser pulse. First, through non-adia-

batic Raman-type excitation of the different molecular rotational levels (see Subsection 8.2), the driving laser spectrum slowly shifts toward lower frequencies (i.e., to the Stokes side) of the spectrum through propagation [114]. This is a consequence of the energy transfer from the light field to the molecules. Second, the macroscopic refractive index modulation caused by the alignment of molecules with anisotropic polarizability tensors is felt by the tail of the driving laser pulse and/or by a delayed probe pulse. This transient refractive index change has several consequences for the probe pulse propagation. For instance, it can modulate its spectrum [83, 165], spatially split its polarization state through polarization selective guiding/defocusing processes (see Section 7) [91, 162], and strongly affect its divergence properties after the filament zone [83]. A detailed analysis based on numerical propagation simulations was carried out by Calegari et al. [212]. Essentially, all the complicated propagation effects can be explained by the refractive index modulation of the medium, which is a function of both space (namely, the radial cylindrical coordinate r from the propagation axis) and time. (See also Section 4.) Also, one could observe the effect of nonadiabatic field free molecular alignment in the other properties of molecules such as their fluorescence. We could demonstrate the possibility of using the filament behavior as a tool for probing phenomena in laser-molecule interaction that is difficult to study with other means. The next two case studies deal with the effect of field free alignment and revival from inside the filament on the anisotropic changes in the refractive index of a probe pulse and in the nitrogen fluorescence signal.

8.4.1. Case study A: probing filament induced anisotropy in air by measuring refractive index change. In a recent article, Marceau et al. [165] demonstrated a simple way to characterize the degree of alignment through the spectral modulation of the probe pulse and we summarize the main results here. The technique consists of measuring the spectral modulation of a weak ($\sim \mu\text{J}$) co-propagating linearly polarized probe pulse as a function of its delay with respect to the driving, 1.1 mJ, 50 fs, 800 nm linearly polarized pump pulse. In order to distinguish the probe from the pump in the spectrometer, the second harmonic of the Ti-sapphire laser was used.

The centroid of the probe spectrum as a function of the delay is shown in Fig. 35 for air and argon for both parallel (\parallel) and perpendicular (\perp) pump and probe polarization.

The theory can be briefly explained as follows. The nonlinear phase ϕ_{NL} accumulated by the probe pulse is given by [78]:

$$\phi_{NL}(r, t) = -\Delta n(r, t)\omega_0 L/c_0, \quad (18)$$

where r denotes the radial cylindrical coordinate, t is time, Δn is the nonlinear refractive index, c_0 is the speed of light in vacuum, ω_0 is the probe central angu-

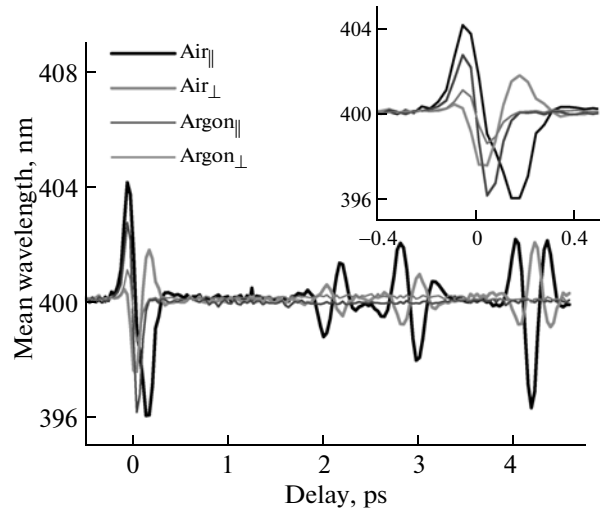


Fig. 35. Centroid wavelength of the probe spectrum as a function of the delay in air and in argon for parallel and perpendicular polarizations of the probe field relative to that of the pump. The initial alignment peaks near delay 0.1 ps. The quarter and half revival of N_2 occur near 2.1 and 4.2 ps, respectively, while the quarter revival of O_2 occurs near 2.9 ps. In argon (atomic gas), spectral modulation only occurs near delay 0 and is attributed to the electronic Kerr effect. Inset: Zoom in around delay 0.

lar frequency and L is the effective interaction length (i.e., the filament length here). The probe angular frequency modulation associated with this time-dependent refractive index modulation is given by:

$$\delta\omega(t) = \frac{d}{dt}\phi_{NL}(t) = -\frac{d}{dt}\Delta n(t)\omega_0 L/c_0. \quad (19)$$

Converting angular frequencies (ω) into wavelengths (λ), in the limit of small spectral modulation ($\Delta\lambda \ll \lambda_0$) and neglecting dispersion ($dn/d\lambda \approx 0$), the spectral modulation is given by:

$$\Delta\lambda(t) \approx \frac{L\lambda_0}{c_0} \frac{d}{dt}\Delta n(t). \quad (20)$$

Here, λ_0 stands for the probe central wavelength (400 nm) and $\Delta\lambda$ is the measured shift (i.e., spectral modulation) in the centroid of the probe pulse spectrum. The refractive index modulation can be computed from this spectral modulation measurement through a simple integral:

$$\Delta n(t) \approx \frac{c_0}{L\lambda_0} \int_{-\infty}^t \Delta\lambda(t') dt'. \quad (21)$$

The integration is from negative infinity up to the particular delay time. The birefringence of the gas medium (air) in the wake of the filament is an obvious consequence of the polarization dependence of the refractive index (see also Section 7). The latter refractive index is obtained from Eq. (21) in which $\Delta\lambda(t)$ for

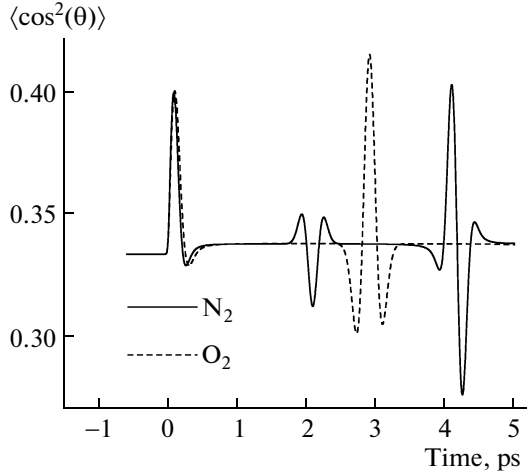


Fig. 36. Calculated alignment factor of N_2 and O_2 due to a 50 fs, 800 nm, 5×10^{13} W/cm 2 Gaussian laser pulse. The initial gas temperature is 295 K.

various polarization is shown in Fig. 35. In fact, for delays >0.1 ps in the case of air, the curves for parallel and perpendicular relative polarizations of the pump and probe are exactly out of phase and the amplitude of the parallel curve is about twice larger than that of the perpendicular curve. This observation agrees well with the theoretical prediction that $\Delta n_{\text{mol},\parallel}(r, t) = -2n_{\text{mol},\perp}(r, t)$ (see below) for a homonuclear diatomic molecule such as N_2 and O_2 [78].

A theoretical calculation of the averaged alignment are shown in Fig. 36 and the refractive index are shown in Fig. 37.

The alignment is computed using the density matrix approach discussed in Subsection 8.3 and the associated refractive index modulation is determined as [78],

$$\Delta n_{\text{mol},x}(r, t) = \frac{2\pi N}{n_0} \Delta\alpha (\langle \cos^2\theta \rangle(r, t) - 1/3), \quad (22)$$

$$\Delta n_{\text{mol},y}(r, t) = -\frac{\pi N}{n_0} \Delta\alpha (\langle \cos^2\theta \rangle(r, t) - 1/3), \quad (23)$$

$$\Delta n_{\text{mol},x}(r, t) = -2\Delta n_{\text{mol},y}(r, t), \quad (24)$$

where N is the medium density, n_0 is the weak field refractive index, $\Delta\alpha$ is the polarizability anisotropy and $\langle \cos^2\theta \rangle(r, t)$ is the most commonly applied measure of alignment, see Subsection 8.3. The refractive index change caused by the electronic Kerr effect is then given as [78],

$$\Delta n_{\text{Kerr},x}(r, t) = 2n_2 I_{\text{pump}}(r, t), \quad (25)$$

$$\Delta n_{\text{Kerr},y}(r, t) = \frac{2}{3} n_2 I_{\text{pump}}(r, t), \quad (26)$$

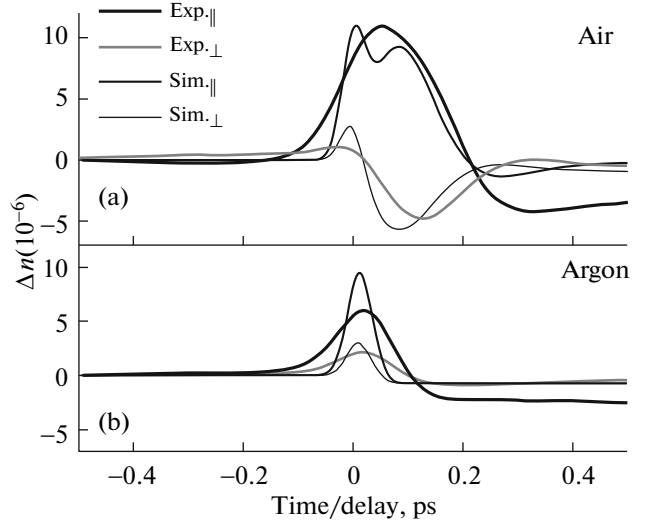


Fig. 37. Transient refractive index modulation (Δn) induced by a filamenting laser pulse and felt by a 400 nm probe pulse in (a) air (b) argon. Simulation (Sim.) and experimental results (Exp.) are shown for both polarization components. Pump pulse conditions for the simulation: 800 nm, 5×10^{13} W/cm 2 , 50 fs Gaussian pulse, 3 cm long filament, plasma density of 10^{16} cm $^{-3}$. The horizontal axis represents the delay between the pulses for the experimental curves and is the time axis for the simulations. There is a small difference between the simulation and the experiment since experimental curves were not deconvoluted for the finite probe pulse duration.

$$\Delta n_{\text{Kerr},x}(r, t) = 3\Delta n_{\text{Kerr},y}(r, t), \quad (27)$$

where n_2 for the case of air is determined empirically in [44] to be 1×10^{-19} cm 2 /W at 800 nm and 40 fs. Finally, the plasma's isotropic contribution to the refractive index is given (in CGS units) by [5]

$$\Delta n_{\text{plasma}}(r, t) = \frac{2\pi e^2 N_e(r, t)}{m_e \omega_0^2}, \quad (28)$$

where e is the elementary charge, N_e is the plasma density and m_e is the electron mass. Good agreement is found between the computed and the measured refractive indices. More interestingly, the calculation illustrates that the measured refractive index responds directly to the rotational wavepacket dynamics.

8.4.2. Case study B: probing filament induced alignment and revival in air by measuring nitrogen fluorescence. In this section, the filament induced alignment and revival can be observed through the behavior of nitrogen fluorescence in a pump-probe experiment; and this in turn reveals an important phenomenon in laser-molecule interaction, namely, population trapping [166]. We studied the fluorescence of two photo-emission bands from inside the filament in air, namely, those of N_2^+ (the first negative band systems ($B^2\Sigma_u^+ \rightarrow X^2\Sigma_g^+$) ($v' = 0 \rightarrow v = 0$) at 391 nm) and

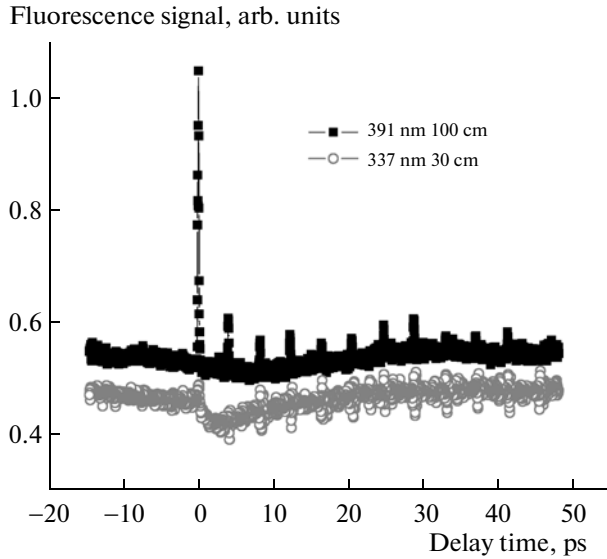


Fig. 38. Fluorescence signal of first negative system of N_2^+ ($B^2\Sigma_u^+ - X^2\Sigma_g^+$ transition) at 391 nm and second positive system of N_2 ($C^3\Pi_u - B^3\Pi_g$) at 337 nm versus delay time with corresponding plan convex lens whose focal lengths are indicated.

neutral N_2 (the second positive band systems ($C^3\Pi_u \rightarrow B^3\Pi_g$) ($v' = 0 \rightarrow v = 0$) at 337 nm). We measured the fluorescence strength versus the delay between the strong fundamental pump and the weak second harmonic probe pulses of the Ti:sapphire laser. The delay time dependence of the fluorescence signal of the 391 nm band using a $f = 100$ cm lens and the 337 nm band using a $f = 30$ cm lens are presented in Fig. 38. There is a strong enhancement at zero time delay. When the probe pulses are behind the pump pulses (positive delay time), periodic weaker enhancement (revival) is observed in the 391 nm band. For the 337 nm band, apart from the decay behavior, an oscillatory structure of the fluorescence signal at the revival positions is observed. Figures 39a and 39b show at a higher resolution the enhancement and the oscillation of the fluorescence signal of ionic and neutral nitrogen molecules at 391 and 337 nm, respectively. The delay time in Fig. 39 is in the vicinity of the full revival period of nitrogen molecules. Figure 39c depicts the rotational parameter of nitrogen obtained from theoretical calculation. The photo-induced alignment dynamics of nitrogen molecules is calculated using a density matrix approach which is explained in Subsections 8.1–8.3. We shall explain the fluorescence signals observed in Fig. 38 through field free alignment and population trapping.

The origin of the fluorescence signals from the 337 and 391 nm bands have been explained in references [52, 221], respectively. Briefly, for the 391 nm band, the strong laser field, through inner valence electron

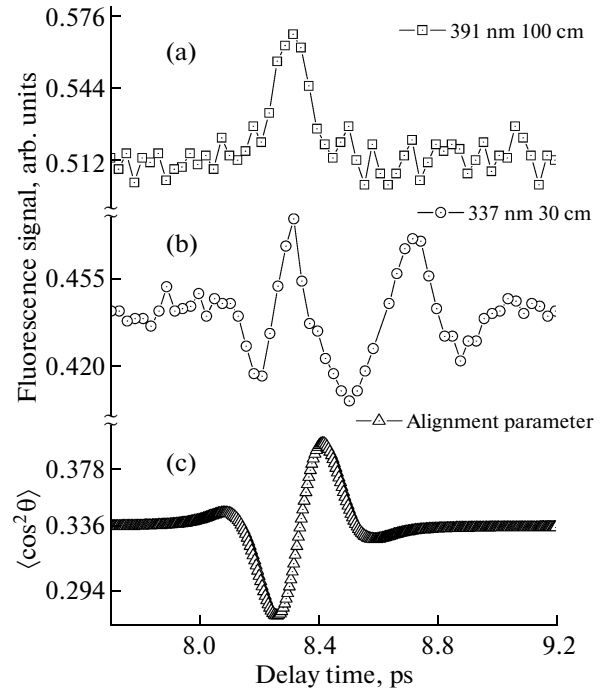


Fig. 39. (a, b) Observed fluorescence signal of ionic and neutral nitrogen molecules and (c) calculated alignment parameter versus delay time in the vicinity of full revival period of nitrogen. One of the parameters influencing fluorescence signal is field free alignment.

excitation, populates the excited $B^2\Sigma_u^+$ ionic band which decays through fluorescence to the ground ionic $X^2\Sigma_g^+$ band. (In this work, we measured only the strongest fluorescence signal from the 0–0 band around 391 nm.) The 337 nm bands is the transition of the neutral nitrogen's $C^3\Pi_u$ band to $B^3\Pi_g$ band, the strongest transition amongst all vibrational transitions from these bands is the 0–0 vibrational transition, around 337 nm. The upper band is dominantly populated by dissociative recombination through the process $N_2^+ + N_2 \rightarrow N_4^+ + e \rightarrow N_2^*(C^3\Pi_u) + N_2$ in atmospheric pressure [52]. That is to say, the 337 nm fluorescence depends very much on the nitrogen ion density.

Besides nonadiabatic field free alignment, there is population trapping (or interference stabilization) [222, 223] induced by the pump pulse. Lowest order perturbation theory (LOPT) predicts that the increase in ion yield versus the laser peak intensity (I) will follow an I^n power law (n being the number of the photons participating in ionization). Stabilization is manifested by a decrease in ion yield with increasing intensity of the laser field. During the interaction, the pump pulse gives rise to population trapping in highly excited (Rydberg) states of nitrogen molecules converging to

both the ground and excited state ions. Such neutral excited molecules can be aligned by the linearly polarized pump pulse at 800 nm and revive periodically.

The arrival of the probe pulse, whose linear polarization is parallel to that of the pump pulse will ionize molecules that are trapped in the highly excited states through one or two photon absorption. Ionization of nitrogen molecules aligned in the polarization direction of the pump is more probable as compared to those molecules perpendicularly aligned [224]. At near zero time delay, enhancement of the fluorescence signals at both wavelengths (391 and 337 nm) occurs. This enhancement includes the effect of two color ionization and alignment enhancement of ionization. At longer delay, ionization is enhanced at the periodic revival times. This results in periodic fluorescence enhancement of the first negative band at 391 nm as it is shown in Fig. 38. Figure 39a shows the same enhancement in higher temporal resolution around the revival period of nitrogen molecule's rotational wave packet. The consequence of this process is that the number of N_2^+ ions is increased, which influences the signal at 337 nm.

The fluorescence signal from the 337 nm band in Fig. 39b, shows a clear oscillatory structure. This fluorescence is the result of collision between neutral and ionic nitrogen molecules as explained above. Another process that influences the signal detection is the anisotropy of the fluorescence with respect to the alignment. The detection direction is perpendicular to the laser propagation axis and parallel to the pump and probe polarization axis. Hence, the detected fluorescence is minimized when the molecules are aligned in the observation direction and maximized when the alignment direction is perpendicular to the observation axis. The result is the oscillation of the fluorescence signal observed at 337 nm. The period corresponds to the periodic revival of the aligned nitrogen molecular wave packet.

In summary, the effect of molecular alignment on the fluorescence signal has been confirmed by theoretical calculations [166]. Population trapping of nitrogen molecules in highly excited states seems to be at the origin of the enhancement. These results show that trapping is an important phenomenon accompanying ionization during ultrafast strong laser field interaction with atoms and molecules.

8.5. Opportunities and Directions

Our goal in this chapter has been to provide a personal view of the role of nonadiabatic alignment in laser filamentation. To that end we first briefly reviewed the essential physics underlying nonadiabatic alignment, the underlying theory and several of the most pertinent observation methods. We next focused on a number of the recently observed consequences of

alignment in femtosecond laser filamentation experiments.

The combination of nonadiabatic alignment with filamentation observables is a very young field of research and several opportunities remain to be realized. On the one hand, alignment can serve as a control tool of filamentation dynamics and enrich the range of applications of laser filaments. On the other, the spectroscopic techniques of filamentation physics offer an easy and efficient way of studying alignment, orientation and wavepacket revivals under high pressure. Although attention so far has been exclusively focused on the constituents of air—rigid diatomic homonuclear molecules, we expect the fundamental interest in oriented polar molecules, in three-dimensionally aligned nonlinear molecules, and in nonrigid systems to further enrich the field in future years.

9. FILAMENTATION ATMOSPHERIC SCIENCE

This section describes some attempts to fulfill some ultimate dreams; i.e., using filamentation to control lightning and rainfalls, remotely measure pollutants and high electric fields and deliver (guiding) high power microwaves onto remote targets. Lightning control experiments have been reviewed previously in some detail [5]. So was remote sensing of pollutants molecules in air using the fluorescence and LIDAR technique [10, 225].

9.1. Lightning Control

Since the beginning of filamentation research, it was already realized that one could use the filament to guide lightning, in principle [226]. A few serious experiments were carried out in high voltage laboratories resulting in the possibility to guide high voltage discharge over a distance of up to a few meters in air [227–240]. The discharge could even go through a shower imitating rain fall [240]. An experiment was done in the field. The French–German Teramobile group moved their terawatt level laser system inside a transportable container (hence, Teramobile) to the Langmuir Laboratory of the New Mexico Tech, on South Baldy peak (3200 m altitude) [241]. Positive results were obtained. According to the authors, we quote [242], “the conducting filaments generated by the laser pointed toward the thundercloud have behaved like a metallic tip directed towards a loaded electrode; they have initiated corona discharges at their tip. Our result provides observable evidence that allows us to optimize the laser parameters in future field campaigns.”

The laser group in CRIEPI (Central Research Institute of Electric Power Industries), Japan, in an attempt to understand why lightning occurs at a very low electric field of the order of 1 kV/cm, has recently studied laser-filament-assisted corona bursts near a high-voltage electrode at both positive and negative

polarities [233, 238, 239]. Filaments were created below a high voltage electrode by focusing 800 nm/60 fs/84 mJ Ti-sapphire laser pulses by a long focal length concave mirror ($f = 10$ m). Using imaging technique, they measured the UV fluorescence from the second positive band of nitrogen molecule ($N_2 : C^3\Pi_u \rightarrow N_2 : B^3\Pi_g$) in and around the filament zone near the high voltage electrode. The position of the UV source moved away from the electrode after the laser filament was formed. The result was correlated with the still images of the corona bursts. The latter image showed that streamer “shot” out away from the electrode up to the position where the electric field was below 5 kV/cm. They analyzed and concluded that the runaway (high energy) electrons’ avalanche would have ignited the corona bursts.

In spite of the strong interest among many scientists, the development of filament induced lightning, so far, has not gone very fast. There are at least two factors that might have slowed down a smooth development of filament lightning control. One is the laser technology on which we shall comment at the end of this review. The other is the detailed physics of filament induced discharge which is still far from being understood. That is to say, lightning control needs to have more fundamental physical studies.

9.2. Remote Detection of Polluting and/or Dangerous Molecules in Air

We shall only discuss a technique that has been proposed and the feasibility demonstrated recently in the laboratory to remotely measure pollutant and/or dangerous molecules. It is the fluorescence coupled to a LIDAR detection system. This is because the physical process involved in this technique reveals some new physics, namely, super-excited states excited by intense fs laser. Another technique will be very briefly discussed. It is based upon stimulated Raman scattering by the pollutant molecules in the path of the filament.

9.2.1. Fluorescence + LIDAR technique. It was proposed by one of us (SLC) that molecules inside a strong fs laser field would emit fluorescence that was characteristic of the molecules; i.e., each molecule would emit a finger print fluorescence [10]. Systematic experiments were carried out in our laboratory and indeed, it was discovered that different molecules, after interaction with the strong laser field inside the filament, would exhibit distinctive finger print fluorescence [10, 225, 243]. However, the fluorescence comes mainly from the fragments of the molecules which are dissociated by the strong laser. An exception is nitrogen molecule which fluoresces from its neutral and ionic states [51, 52]. The claim is that using only one intense (fs) laser, one could remotely detect most if not all pollutants in air [225].

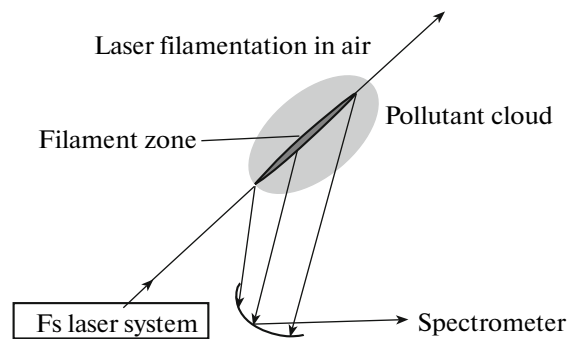


Fig. 40. Experimental scheme to remotely measuring pollutants in air using filamentation induced fluorescence spectroscopy.

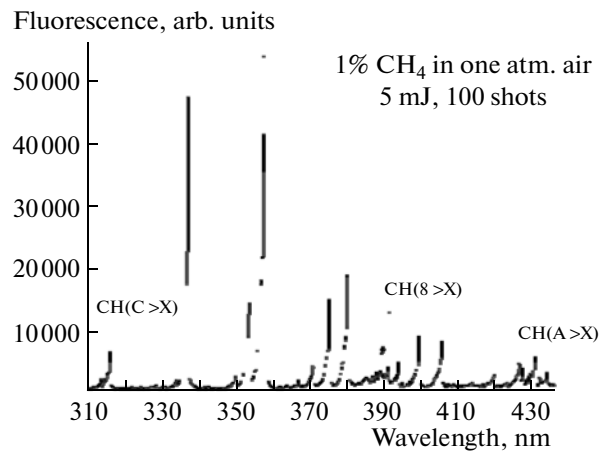


Fig. 41. LIDAR spectrum from inside a filament in 1% CH_4 in air at one atmospheric pressure. The three CH bands are mixed with the normal nitrogen fluorescence.

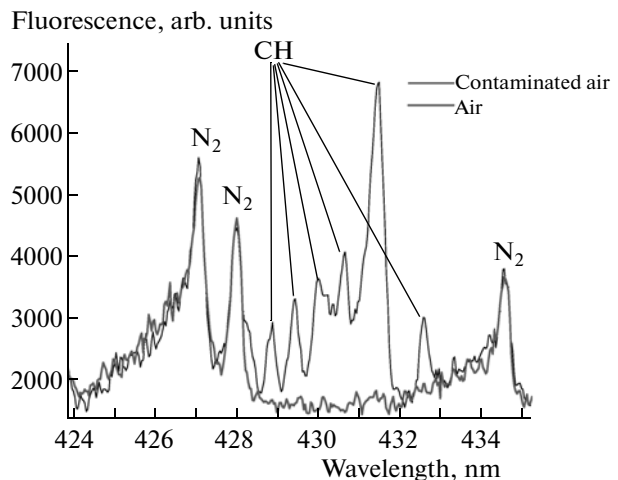


Fig. 42. An enlarged section of the spectrum in Fig. 41 showing that one can resolve the fluorescence of the $CH(A \rightarrow X)$ band from the background nitrogen fluorescence.

So far, we were able to remotely detect fluorescence in the near i.r. through the visible to the near UV spectral ranges where sensitive detectors such as photomultiplier and, in particular, ICCD (intensified CCD) detector exist. The experimental technique is based upon the observation of what we call by clean fluorescence [10, 225]. That is to say, even though plasma exists inside a filament, there is no optical breakdown of air. Only multiphoton/tunnel ionization takes place. The plasma density is very low. In air, it is two to four orders of magnitude lower than the density of air depending on the external focusing condition [27]. Thus, it is the uni-molecular interaction process that leads to the fragmentation and fluorescence. We shall comment on the physics of interaction later. But now, let us dwell upon the experimental observation.

Figure 40 is a schematic drawing of what one would like to do in atmospheric sensing of pollutants. Filamenting fs laser pulses are sent into the atmosphere. Pollutant molecules in the strong field inside the filament zone will be dissociated and the fragments will fluoresce. The back scattered fluorescence is captured by a spectrometer coupled to an ICCD detector. This latter technique is the LIDAR (light detection and ranging) technique.

In the laboratory, the same scheme was used to test this idea except that the laser was shot horizontally through a shorter distance of up to 100m into an interaction chamber where gas mixtures were prepared. Figures 41 and 42 show the spectrum obtained from a mixture of 1% CH₄ in air at one atmospheric pressure [244]. Figure 41 gives the spectrum spanning from the near UV to the blue showing the normal nitrogen fluorescence bands [51, 52] emitted from air filaments as well as the three CH bands from the dissociation of the CH₄ molecules.

Figure 42 is an enlarged section of the spectrum showing that the CH(A → X) band could be resolved from the background nitrogen fluorescence when compared to the spectrum of pure air. This means that one can identify CH₄ in air. Using the LIDAR equation [245], one can estimate the distance at which one could still measure the signal down to three times the root-mean-square noise level (3σ level). Under the experimental conditions in our laboratory (up to ~1 TW peak power), the distance could be as far as a few hundred meters to one or two km. This distance could be easily extended by increasing the peak power and other parameters of the laser pulse, in principle. More will be discussed on the current challenge of the laser technology later.

We have tested the feasibility of remotely (up to 100 m) detecting many gaseous, aerosols, biological and solid targets inside the laboratory environment. (In the case of solids, the targets are placed in the path of the filament zone (Fig. 40). They are: CH₄, C₂H₂ (gases), ethanol (vapor), powders of egg white and yeast, grain dusts of barley, corn and wheat, water

aerosols containing multiple solutes (NaCl, PbCl₂, CuCl₂ and FeCl₂), smoke from mosquito repellent and metallic targets (lead, copper and aluminum). The technique for the detection of solid targets is called femtosecond laser induced breakdown spectroscopy (FIBS) and is the same as the popular LIBS (laser induced breakdown spectroscopy) except that the latter usually uses nanosecond laser pulses to interact with the target. All targets show finger print fluorescence and are scalable to long distance detection [225].

9.2.2. Physics of fluorescence from pollutant targets. The interaction physics and chemistry of pollutants inside the filament (relatively high intensity) yielding fluorescence have not been sufficiently studied yet. They cover a vast range of subjects. Much of these are seemingly well known physics; however, they sometime would yield surprisingly new physics and chemistry when fs time scale is involved. In this subsection, we shall focus on the interaction of the high field inside the filament with molecules in the gas phase while giving some comments on the interaction with aerosols.

In the case of “dry” aerosol such as the [246] smoke coming from burning mosquito coil (repellent), the interaction physics is not known. In the case of water droplet aerosol containing chemical salts, experimental observation indicates that the water droplets were exploded and later end up as neutral atomic fluorescing species. Fluorescence from atomic Na, Fe, Cu, and Al as well as the hydrogen atomic fluorescence were all observed when the filament interacts with water aerosols containing salts of these atoms [247]. Since hydrogen atomic lines were also observed, the water droplets might have been exploded through a yet unknown process yielding excited hydrogen atoms.

The interaction of the high field inside the filament with gas phase molecules reveals some hitherto unsuspected intense field physics and chemistry. The case of nitrogen molecules is discussed in the section on population trapping, molecular alignment and revival. For oxygen molecule and polyatomic molecules, excitation of super-excited states was observed [248–251] and reviewed [10]. So, we shall be brief.

Super-excited states were known to chemists who use the XUV Synchrotron radiation to excite molecules into some highly excited states whose total energy is above the first ionization energy. According to Hatano [252, 253], “most observed SESs are assigned to Rydberg states that are vibrationally (or/and rotationally), doubly, or inner core excited and converge to each of ion states.” Such single photon (low field) excitation could be extended to multiphoton (high field) excitation when the laser field is strong. Indeed, this is how we explain our observation of super-excited states [10, 248–251] using a pump probe technique.

After multiphoton excitation, the super-excited states would decay quickly into various channels one of which is the neutral dissociation of the parent molecule into neutral excited fluorescing fragments. The fluorescence coming from the neutral fragments of the molecules such as that shown in Fig. 42 is the result of the fast decay from the super-excited states into the fragmentation channel. In the case of oxygen molecules, the super-excited states were assigned to the various Rydberg states converging to various excited ionic states. There are many fluorescence lines coming from the dissociated neutral oxygen atoms. By monitoring the fluorescence using a fs pump-probe scheme, the life time (fast decay time) of the super-excited states could be measured. The physical process is such that before the super-excited states decay into the fragmentation and fluorescence channels, the fs probe pulse would de-excite the super-excited state “cutting” the route towards the fragmentation and fluorescence channel. This would result in the decrease in the fluorescence signal. The very short decay time could thus be measured by changing the delay between the pump and probe pulses. For the super-excited state in CH_4 decaying into the various CH fluorescence, the life time is about 200 fs [248, 250]. For oxygen molecules, it is also of the order of 200 fs [251].

9.2.3. Filamentation Raman detection of pollutants.

Another technique used by the group of Levis to remotely detect pollutants is based upon stimulated Raman spectroscopy inside the filament. Both gas and liquid phase targets [254–257] as well as solid targets [258, 255] were studied. By superposing a supercontinuum (SC) pulse with another ultrafast laser pulse, stimulated Raman transition was measured. For example, in the case of acetone and methanol (liquid), the ultrafast pulse is a 400 nm/fs pump pulse [254]. In the case of gas phase target such as N_2 , O_2 , CO_2 , H_2 , toluene, ammonia, and chloroform, the SC pulse came from a filamenting 1.9 mJ/40 fs Ti-sapphire laser pulse focused by a 2 m lens in air resulting in the SC pulse with self-pulse compression. It superposed with the ~ 0.5 mJ/40 fs Ti-sapphire laser pulse resulting in the stimulated Raman signatures [255–257]. Solid targets were studied using fs LIBS spectroscopy on graphite samples, for example [258, 250].

9.3. Filament Induced Water Condensation in Air

The dream of rain making through filamentation should start from the first step of filament induced condensation. In the first review published by one of us (SLC) and coworkers in 2005 [5], we mentioned this possibility. We quote the following from [5].

“An experiment by the Teramobile group [259] shows that filamentation inside a cloud chamber can induce nucleation of the supersaturated water vapor. The physics is similar to the standard nuclear physics experiment in which ion tracks are left behind by

Gamma rays, for example, and water molecules would nucleate around such ions resulting in water droplets formation. Ionization inside the filaments would have similar consequence. We could now stretch our imagination and ask if this observation could be applied to artificial rain making by generating filaments inside a rain cloud containing supersaturated water vapor.”

Since then, not much was published until this year when the same Teramobile group repeated and further advanced this experiment [242, 260]. They found that even sub-saturated water vapor could be condensed by the Ti-sapphire fs laser filament. They attribute this to the generation of acid such as HNO_3 through the creation of NO , NO_2 inside the filament. They also shot the multi-TW pulses into a humid sky in Berlin and could measure the increase of scattering of a ns probe laser pulse by the filament generated condensation (water droplets). The door is now opened for more research because efficient rain making would certainly help in relieving draught, cooling down cities during hot and humid summers, etc. The challenge is to fully understand the physics and chemistry of both natural rain fall and filament induced rain fall.

9.4. Guiding Microwaves

If one could create a sheath of filaments, it would be similar to an “instantaneous” and flying conducting sheath. Microwave could thus be guided through the sheath overcoming its natural large divergence over a long distance while maintaining a high energy density. Since filaments in principle could be both long and projected to long distances, a filament sheath could guide intense microwave to a distant target for any appropriate application. At least one experimental paper was published showing positive results [261].

A deformable mirror was used to spatially shape 10 Hz/27 fs/1.5 J linearly polarized Ti-sapphire laser pulses (diameter; 95 mm) into a ring in air. The ring-shaped pulse generated more than 1000 closely spaced filaments resulting in a plasma hollow cylindrical zone with a diameter of about 45 mm. This plasma zone would be able to guide through internal reflection electromagnetic waves whose frequency is lower than the plasma frequency which in the case of filament-plasma is limited to about 300 GHz [262]. In this work, 10 GHz microwave was guided by the filament wave guide over a distance of 16 cm. The detected guided signal was increased by a factor of greater than 6 compared to the free propagation of the microwave radiations.

9.5. Filament Assisted Remote Measurement of High Static Electric Field

There is a practical need to measure high voltage remotely. For example, in high voltage (~ 1000 kV) electric power transmission lines and similar facilities, it is necessary to measure the high voltage for diagnos-

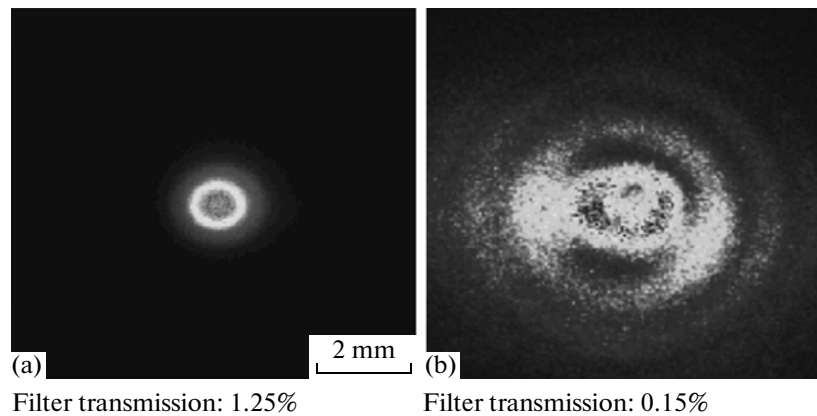


Fig. 43. Beam patterns measured after the ionization segment using bandpass filters at (a) 850 and (b) 800 nm at 16 m from the compressor. The former shows the red-shifted post-filament core and the latter the energy reservoir which suffered from diffraction of the plasma filament.

tics. During a thunder storm, it is desirable to know the high electric field at the tip of lightning rods for better prevention of lightning strike on buildings. It is also desirable to measure the electric field distribution in air under a thunder cloud. Thus, in parallel to their study of filament assisted corona bursts, the CRIEPI group studied remote measurement of high electric field through measuring the UV fluorescence from nitrogen molecules at 337.1 nm; the latter corresponds to the strongest emission of the second positive band of nitrogen molecules ($N_2 : C^3\Pi_u \rightarrow N_2 : B^3\Pi_g$) [238, 239].

Ti-sapphire laser pulses (800 nm, 50–60 fs, 4 mJ) were focused by a 10 m focal length concave mirror generating a long plasma filament at various positions below a high voltage electrode in open air. Two sets of high voltage spherical electrodes (radii: 60 and 250 mm) were used so as to observe interaction in different electric fields. The 337.1 nm fluorescence from inside the filament was measured as a function of electric field. The fluorescence strength increased as the electric field increased. The explanation is the increase of electron avalanche ionization in the high electric field resulting in more electron-ion recombination, hence, more fluorescence from excited nitrogen molecules. This measurement paved the way towards remote measurement of electric field for practical purposes such as those mentioned above.

10. NON-IONIZING FILAMENT AND HIGHER ORDER KERR CONTRIBUTION

The question of non-ionizing filaments has been a subject of debate in the mid-2000 [5, 263]. Up until recently, it seems to have been settled; i.e., a non-ionizing filament is essentially the prolongation of the propagation after the end of the plasma filament [264]. That is to say, after the end of a filament when plasma generation has stopped, the intensity in the filament

core of the pulse is still high but not so high as to ionize the medium (air). Thus, self-focusing through the Kerr term $n_2 I$ is still significant but diffraction is now stronger. This would result in a slowly diverging beam core in which the intensity is still respectable over a rather long distance without ionization and is considered to be the non-ionizing filaments observed in ref. [263].

Recently, the group of one of us (SLC) has performed a systematic experiment to check this point. Indeed, we found that the divergence of the filament core after the ionization zone is more than one order of magnitude smaller than the linear divergence of the same pulse over a long distance [265]. The experiment was done using short laser pulses (800 nm/45 fs/5 mJ) emitted at a 10 Hz repetition rate from a typical Ti:sapphire amplifier. The initial beam diameter after the pulse compressor was elliptical in shape with major and minor axes at FWHM of 4.2 and 3.9 mm, respectively. The laser pulses formed a single filament 10–15 m after the pulse compressor and their post-filamentation propagation was rigorously investigated up to 50 m. In order to avoid any damage to the equipment, a weak reflection from the original pulse incident on fused silica a wedge was sent to a white diffuser. A CCD camera protected with a bandpass filter at 800 nm and appropriate ND filters was used to capture the images.

Figure 43 presents beam patterns measured after the ionization zone (16 m from the compressor) using bandpass filters with 10 nm transmission window centered at 850 (a) and 800 nm (b). Figure 43a shows the perfectly circular Raman red-shifted post-filament core [24, 114]. The measured beautiful beam pattern is the result of spatial filtering during filamentation caused by the self-focusing of the beam's fundamental mode into the filament core [24, 25, 266]. The Raman frequency red shift (see Subsection 5.1) phenomenon, occurs only in the high intensity core at the front part

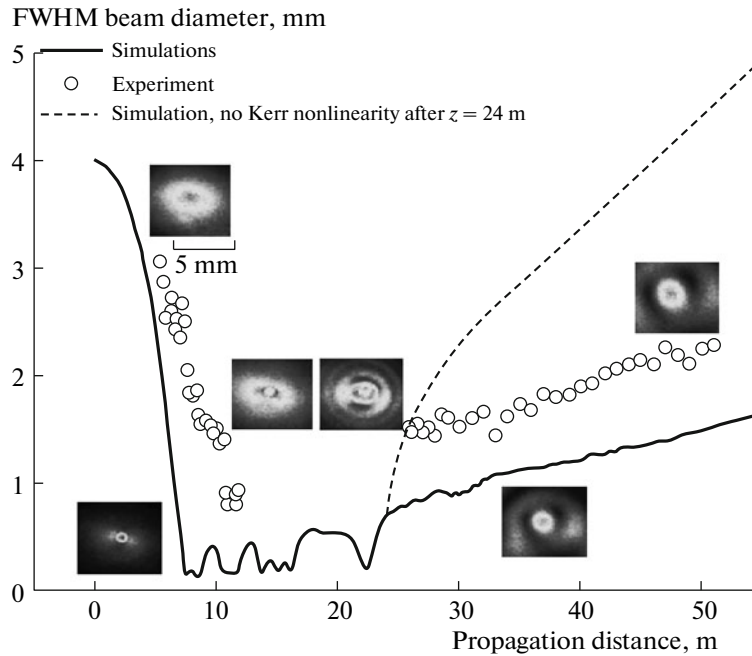


Fig. 44. Full width at half maximum beam diameter of 800 nm radiation measured along the propagation direction in the experiment (circles) and the simulations (solid line). In the experiment no data points were placed between 12–25 m because a clear axial hot spot could not be observed due to strong diffraction. The dashed curve is obtained if the nonlinear contribution to the Kerr nonlinearity $\Delta n_k = 0$ (see Eq. (2)) at $z \geq 24$ m. The inserted beam patterns correspond to characteristic events of the pulse's propagation.

of the pulse; hence, it does not encounter any plasma and is perfectly circular. However, the pattern in Fig. 43b is the result of the diffraction of the back part of the pulse including the background reservoir [17] by the cylindrical plasma filament left behind by the front part of the pulse. Even though the core profile around 850 nm (Fig. 43a) is of excellent quality, its energy content is rather weak. For comparison, we need to use a higher filter transmission (1.25%) to obtain the picture in Fig. 43a while in Fig. 43b, the filter transmission was lower (0.15%).

It was demonstrated numerically that in the far field, diffraction on a circular opaque obstacle [267] (plasma), develops into an intense axial spike surrounded by weak Bessel-like rings. Because of its high energy content, the formation of this axial spike, also known as Arago's spot, is present everywhere along the propagation axis in the exact center of the dark shadow [267]. It is at the source of intense ionization-free light channels. However, as described in the following paragraphs, diffraction only cannot explain the low divergence observed in the experiment.

Figure 44 shows the evolution of the beam diameter vs propagation distance measured using the beam patterns at 800 nm through a filter of 10 nm bandwidth. The beam patterns inserted present characteristic events during the propagation of the laser pulses measured at 800 nm. The laser pulses first underwent filamentation giving rise to the minimum zone between

12 and 25 m where plasma was generated [268]. In this zone, diffraction of the back part of the pulse by the plasma generated by the peak of the pulse (as discussed above in Fig. 43) prohibited us to measure the core diameter correctly. The axial hot spot could not be observed due to strong diffraction effects such that no data points were placed in this range. However, beyond 25 m, the Bessel-like pattern evolved into a central spike with extremely good spatial mode and a low divergence of 0.03 mrad. 51 m after the pulse compressor, the channel's intensity was estimated to be 0.5 TW/cm² which could not ionize air, but could induce sufficiently high self-focusing to reduce linear diffraction over a long distance. The solid line in Fig. 44 shows the evolution of the simulated FWHM diameter of the radiation filtered at 800 nm. The filament starts 3 m earlier in the simulations as compared to the experiment (filled circles in Fig. 44) due to the purely Gaussian and not elliptical initial intensity distribution used for the calculation. In addition, the larger post-filament diameter observed in the experiment was caused by the weak reflected pulse which suffered diffraction during its propagation between the wedge and the CCD. At the same time the divergence angle after the end of the filament is in quantitative agreement with the experimental one. The physical reason for the slow divergence is the $\chi^{(3)}$ Kerr nonlinearity of the neutral air molecules, which prevents the post-filament beam to diverge. In fact, the dashed curve in Fig. 44 corresponds to the simulated evolution of the

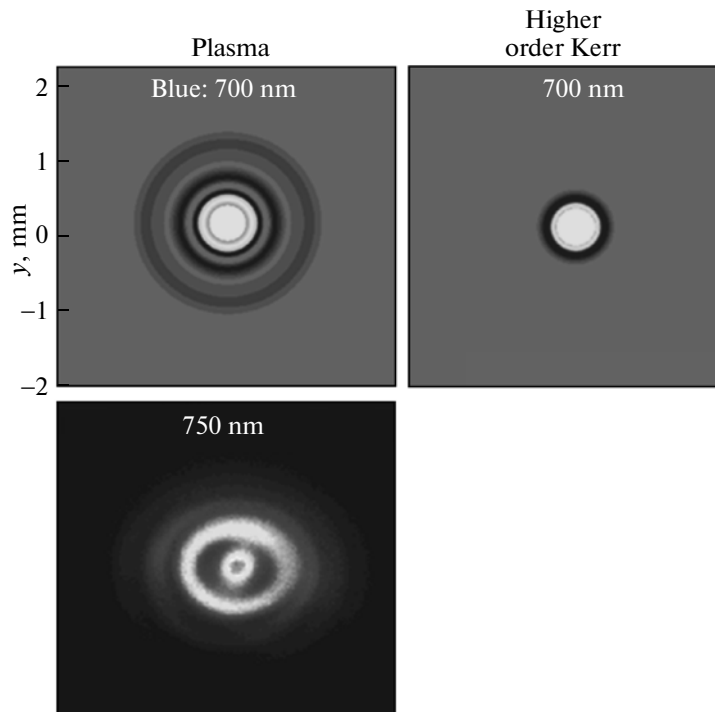


Fig. 45. Beam patterns in the middle of the filament in air during the filamentation of a Ti-sapphire laser at 800 nm/45 fs/5 mJ. Bottom: experimentally obtained pattern through a filter at 750 nm (bandwidth: 10 nm). Top row: simulated beam patterns; left, first order Kerr term plus plasma generation; all Kerr terms without plasma generation.

pulse if the Kerr non-linearity were switched off for distances larger than 24 m. Consequently, self-focusing must have played a dominant role to maintain a small diameter over long distances.

Another experiment was performed using low peak power pulses (low energy long ~ 300 ps uncompressed pulses) to measure the divergence in the linear regime under the same propagation conditions. It was found that the divergence started to decrease from ~ 1 MW peak power onwards. That is to say, nonlinear regime starts at around 1 MW under our experimental condition. This shows that non-ionizing filaments are indeed the slowly diverging post-ionization core. According to this observation, one could also conclude that non-ionizing filament could be defined as any beam with divergence smaller than linear divergence due to weak self-focusing. It could be generated without prior ionization. In our case, so long as the peak power is higher than 1 MW, the beam could be considered as a nonionizing filament.

A new development occurred in the past year. Lorient et al. [269] measured quantitatively the higher order terms of the Kerr nonlinear index of refraction of air in a series expansion with alternate positive and negative signs. B ejot et al. [270] calculated the formation of filament in air by including these higher order Kerr terms. The simulated result of the latter showed some very interesting results. They found that even without including the ionization term in the wave

equation, the higher order terms, which together are negative, are strong enough to stop the self-focusing due to the first Kerr term $n_2 I$. Thus, according to the authors of [244], any filamentation would not involve ionization. The plasma generation in all experiments so far is simply considered by them as a side effect [270].

To confront this new development, a comparative analysis was performed recently by one of us (Olga Kosareva of Moscow State University and her group) in the simulation of conical emission using the conventional model and the higher order model. The results of the simulation were compared with experiments from the group of one of us (SLC) in Laval University [19]. It was found that in the experiment, conical emission is evident in the anti-Stokes side of the supercontinuum. In the simulation, only the conventional model reveals conical emission while the new higher order model does not. Figure 45 shows such a comparison.

It is evident that the simulated pattern using the usual first Kerr term and plasma generation looks similar to the experimental result; i.e., with ring structure (diffraction by the plasma). The pattern with all the Kerr terms without plasma does not show such diffraction rings.

We shall not draw a conclusion on this matter at this stage of development yet. Comparison with other experiments is being carried out by other groups. It

probably will take another year or so before a definitive comment could be made on this interesting subject.

11. CHALLENGES AHEAD

The field of intense fs laser filamentation *in air* has aroused a lot of attention in recent years probably because of the prospect of projecting the pulse to long distances at high intensity, a characteristic that no other laser possesses. This, *in principle*, would open up a lot of possibilities to do remote sensing, remote interaction, remote high laser field applications, remote nonlinear optics, etc. We have talked about lightning control, rain making, THz generation, remote sensing of pollutants, remote measurement of high electric field, etc. However, it is precisely the word “remote” that is challenging us. How far away could we really project the pulse and obtain real filamentation with high energy at high (clamped) intensity?

Most of the past and current research work is still being carried out in the laboratory. The possibility to carry out the so-called “remote” experiment is mostly extrapolation of laboratory results (see for example, ref. [225] in the case of “remote” detection of pollutants). Limited success was achieved in the field with the very few mobile TW laser systems such as the European Teramobile and the Canadian T&T system, the latter being mainly reserved for defense related work. There are other TW level mobile laser systems but the number, the where-about and the results are unknown because they are classified. Yet, there is a need to carry out more systematic field tests after laboratory demonstration of the feasibility of a certain application.

A practical difficulty is related to the cost of the currently available fs high power laser system; it is far too expensive. When applying the fruit of the research to application in the commercial market, it would become too expensive for any investor to seriously consider putting money into developing a product using multi-TW lasers. The cost of the laser system would most probably go down in the future when more commercializable applications are demonstrated.

To the best of our knowledge, classified or not, current high power fs laser system could not properly deliver very high energy, high (clamped) intensity plasma filaments to distances of a few km or more away. In the open literature, the longest is a few hundred meters [263]. Since any practical application would need to deliver much energy and high (clamped) intensity at targets situated at longer distances, we should question why it is so difficult to achieve this goal since, *in principle*, there should have no difficulty.

The difficulty is twofold. One is multiple filament competition and the other is beam quality. The two of them are closely related. Bad beam quality with irreg-

ular intensity distribution across the wave front would lead to multiple filaments. For long distance propagation, it is necessary to increase the beam diameter. If it is under free propagation condition, multiple filament competition is unavoidable reducing the efficient conversion of the laser energy into useful filament energy. One could use a focusing lens to focus the large diameter beam to a predetermined distance so that only near the geometrical focusing zone will there be filament formed [150]. Under this condition, only filament cooperation occurs in the external focal region where the diameter is small. Multiple filaments under this condition of small diameter will be cooperative as discussed in Section 2. This technique is successful up to 100 m or so. For longer distances, the geometrical focal diameter becomes larger and multiple filaments competition occurs. Using deformable mirror would correct the wave front aberration but not the intensity distribution. Hence, the success is limited [271]. The key correction scheme, in our opinion, is to improve the beam quality. Until this happens, real long distance filamentation (1 km or more) would have to be patient. All current TW to multi-TW level lasers (mostly Ti:sapphire laser) use multi-pass “bowtie” configuration along with a non-uniform pumping. Hot spots/zones in the pulse front are unavoidable. These are the sources of multiple filaments.

On the theory side, there is a need to have a fully quantitative 3D model to accurately predict any experimental outcome. So far, this has not yet happen.

ACKNOWLEDGMENTS

The authors from Laval University acknowledge the financial support of the Natural Sciences and Engineering Research Council of Canada (NSERC), Defence Research Development Canada-Valcartier, Canada Research Chairs, le Fonds Québécois pour la Recherche en Nature et Technologie (FQRNT), the Canada Foundation for Innovation (CFI) and the Canadian Institute for Photonics Innovation (CIPI). They thank the contributions from Yousef Kamali, Jens Bernhardt, Sima Hosseini, Patrick Simard, Abdulsamad Talebpour and Huailiang Xu as well as the technical support from Mario Martin. H.Z. and J.W. acknowledge the financial support by the National Natural Science Fund, National Key Project for Basic Research, and Projects from Shanghai Science and Technology Commission. Contributions from H. Z.’s group members and students (H. Cai, X. Yang, J. Ding, and H. Pan) and from Profs. Z. Xu and L. Ding are highly appreciated. H.Z. and J.W. thank Dr. A. Couairon for valuable discussions. T. Seideman would like to acknowledge the US Department of Energy (grant no. DE-FG02-04ER15612). O.G. Kosareva and N.A. Panov acknowledge the support from Russian Foundation for Basic Research, grant no. 09-02-01200a, RFASI

no. 02.740.11.0223, the President of the RF grant MK-2213.2010.2.

REFERENCES

1. R. Y. Chiao, E. Garmire, and C. H. Townes, *Phys. Rev. Lett.* **13**, 479 (1964).
2. M. Hercher, *J. Opt. Soc. Am.* **54**, 563 (1964).
3. J. H. Marburger, *Prog. Quantum Electron.* **4**, 35 (1975).
4. A. Braun, G. Korn, X. Liu, D. Du, J. Squier, and G. Mourou, *Opt. Lett.* **20**, 73 (1995).
5. S. L. Chin, S. A. Hosseini, W. Liu, Q. Luo, F. Théberge, N. Aközbek, A. Becker, V. P. Kandidov, O. G. Kosareva, and H. Schroeder, *Can. J. Phys.* **83**, 863 (2005).
6. A. Couairon and A. Mysyrowicz, *Phys. Rep.* **44**, 47 (2007).
7. L. Bergé, S. Skupin, R. Nuter, J. Kasparian, and J.-P. Wolf, *Rep. Prog. Phys.* **70**, 1633 (2007).
8. J. Kasparian and J.-P. Wolf, *Opt. Express* **16**, 466 (2008).
9. V. P. Kandidov, S. A. Shlenov, and O. G. Kosareva, *Quantum Electron.* **39**, 205 (2009).
10. S. L. Chin, *Femtosecond Laser Filamentation*, Monography, Springer series on Atomic, Optical, and Plasma Physics, Vol. 55 (Springer Sci. Business Media, New York, 2010).
11. *Self-Focusing: Past and Present*, Ed. by R. W. Boyd, S. G. Lukishova, and Y. R. Shen (Springer, New York, 2009).
12. P. Di Trapani, G. Valiulis, A. Piskarskas, O. Jedrkiewicz, J. Trull, C. Conti, and S. Trillo, *Phys. Rev. Lett.* **91**, 093904 (2003).
13. M. Kolesik, E. M. Wright, and J. V. Moloney, *Phys. Rev. Lett.* **92**, 253901 (2004).
14. A. Couairon, E. Gaižauskas, D. Faccio, A. Dubietis, and P. Di Trapani, *Phys. Rev. E* **73**, 016608 (2006).
15. S. L. Chin, "From Multiphoton to Tunnel Ionization," in *Advances in Multiphoton Processes and Spectroscopy*, Ed. by S. H. Lin, A. A. Villaeys, and Y. Fujimura, Vol. 16 (World Sci., Singapore, 2004), pp. 273–306.
16. D. Strickland and G. Mourou, *Opt. Commun.* **56**, 219 (1985).
17. M. Mlejnek, E. M. Wright, and J. V. Moloney, *Opt. Lett.* **23**, 382 (1998).
18. G. Fibich, Y. Sivan, Y. Ehrlich, E. Louzon, M. Fraenkel, S. Eisenmann, Y. Katzir, and A. Zigler, *Opt. Express* **14**, 4946 (2006).
19. O. Kosareva, J.-F. Daigle, N. Panov, T.-J. Wang, S. Hosseini, S. Yuan, G. Roy, V. Makarov, and S. L. Chin, *Opt. Lett.* **36**, 1035 (2011).
20. J. Kasparian, R. Sauerbrey, and S. L. Chin, *Appl. Phys. B* **71**, 877 (2000).
21. A. Becker, N. Aközbek, K. Vijayalakshmi, E. Oral, C. M. Bowden, and S. L. Chin, *Appl. Phys. B* **73**, 287 (2001).
22. W. Liu, S. Petit, A. Becker, N. Aközbek, C. M. Bowden, and S. L. Chin, *Opt. Commun.* **202**, 189 (2002).
23. M. B. Gaarde and A. Couairon, *Phys. Rev. Lett.* **103**, 043901 (2009).
24. W. Liu and S. L. Chin, *Phys. Rev. A* **76**, 013826 (2007).
25. F. Théberge, N. Aközbek, W. Liu, A. Becker, and S. L. Chin, *Phys. Rev. Lett.* **97**, 023904 (2006).
26. D. Shwa, S. Eisenmann, G. Marcus, and A. Zigler, *Opt. Express* **17**, 6451 (2009).
27. F. Théberge, W. Liu, P. Tr. Simard, A. Becker, and S. L. Chin, *Phys. Rev. E* **74**, 036406 (2006).
28. M. Mlejnek, M. Kolesik, J. V. Moloney, and E. M. Wright, *Phys. Rev. Lett.* **83**, 2938 (1999).
29. Q. Luo, S. A. Hosseini, W. Liu, J.-F. Gravel, O. G. Kosareva, N. A. Panov, N. Aközbek, V. P. Kandidov, G. Roy, and S. L. Chin, *Appl. Phys. B* **80**, 35 (2005).
30. O. G. Kosareva, N. A. Panov, N. Aközbek, V. P. Kandidov, Q. Luo, S. A. Hosseini, W. Liu, J.-F. Gravel, G. Roy, and S. L. Chin, *Appl. Phys. B* **82**, 111 (2006).
31. S. A. Hosseini, Q. Luo, B. Ferland, W. Liu, N. Aközbek, G. Roy, and S. L. Chin, *Appl. Phys. B* **77**, 697 (2003).
32. S. A. Hosseini, Q. Luo, B. Ferland, W. Liu, S. L. Chin, O. G. Kosareva, N. A. Panov, N. Aközbek, and V. P. Kandidov, *Phys. Rev. A* **70**, 033802 (2004).
33. C. P. Hauri, J. Gautier, A. Trisorio, E. Papalazarou, and P. Zeitoun, *Appl. Phys. B* **90**, 391 (2008).
34. P. Rohwetter, M. Queisser, K. Stelmaszczyk, M. Fechner, and L. Woste, *Phys. Rev. A* **77**, 013812 (2008).
35. M. Hentschel, R. Kienberger, Ch. Spielmann, G. A. Reider, N. Milosevic, T. Brabec, P. Corkum, U. Heinzmann, M. Drescher, and F. Krausz, *Nature* **414**, 509 (2001).
36. G. Sansone, E. Benedetti, F. Galegari, C. Vozzi, L. Avaldi, R. Flammini, L. Poletto, P. Villoresi, C. Altucci, R. Velotta, S. Stagira, S. De Silvestri, and M. Nisoli, *Science* **314**, 443 (2008).
37. C. P. Hauri, W. Kornelis, F. W. Helbing, A. Heinrich, A. Couairon, A. Mysyrowicz, J. Biegert, and U. Keller, *Appl. Phys. B* **79**, 673 (2004).
38. M. Nisoli, S. D. Silvestri, and O. Svelto, *Appl. Phys. Lett.* **68**, 2793 (1996).
39. X. Chen, X. Li, J. Liu, P. Wei, X. Ge, R. Li, and Z. Xu, *Opt. Lett.* **32**, 2402 (2007).
40. D. Uryupina, M. Kurilova, A. Mazhorova, N. Panov, R. Volkov, S. Gorgutsa, O. Kosareva, A. Savel'ev, and S. L. Chin, *J. Opt. Soc. Am. B* **27**, 667 (2010).
41. M. Ghotbi, P. Trabs, and M. Beutler, *Opt. Lett.* **36**, 463 (2011).
42. O. D. Mücke, S. Ališauskas, A. J. Verhoef, A. Pugzlys, A. Baltuška, V. Smilgevičius, J. Pocius, L. Giniūnas, R. Danielius, and N. Forget, *Opt. Lett.* **34**, 2498 (2009).
43. J. Bernhardt, W. Liu, S. L. Chin, and R. Sauerbrey, *Appl. Phys. B* **91**, 45 (2008).
44. W. Liu and S. L. Chin, *Opt. Express* **13**, 5750 (2005).
45. O. G. Kosareva, W. Liu, N. A. Panov, J. Bernhardt, Z. Ji, M. Sharifi, R. Li, Z. Xu, J. Liu, Z. Wang, J. Ju, X. Lu, Y. Jiang, Y. Leng, X. Liang, V. P. Kandidov, and S. L. Chin, *Laser Phys.* **19**, 1776 (2009).

46. Z. G. Ji, J. S. Liu, Z. X. Wang, J. Ju, X. M. Lu, Y. H. Jiang, Y. X. Leng, X. Y. Liang, W. Liu, S. L. Chin, R. X. Li, and Z. Z. Xu, *Laser Phys.* **20**, 886 (2010).
47. J. Bernhardt, W. Liu, F. Théberge, H. L. Xu, J. F. Daigle, M. Châteauneuf, J. Dubois, and S. L. Chin, *Opt. Commun.* **281**, 1268 (2008).
48. J. Muth-Boehm, A. Becker, and F. H. M. Faisal, *Phys. Rev. Lett.* **85**, 2280 (2000).
49. A. Jaron-Becker, A. Becker, and F. H. M. Faisal, *Phys. Rev. A* **69**, 023410 (2004).
50. A. Talebpour, S. Petit, and S. L. Chin, *Opt. Commun.* **171**, 285 (1999).
51. A. Talebpour, M. Abdel-Fattah, and S. L. Chin, *Opt. Commun.* **183**, 479 (2000).
52. H. L. Xu, A. Azarm, J. Bernhardt, Y. Kamali, and S. L. Chin, *Chem. Phys.* **360**, 171 (2009).
53. A. Talebpour, J. Yang, and S. L. Chin, *Opt. Commun.* **163**, 29 (1999).
54. S. Q. Xu, Y. B. Zheng, Y. Liu, and W. Liu, *Laser Phys.* **20**, 1968 (2010).
55. X. Lu, X. L. Liu, T. T. Xi, X. Liu, and J. Zhang, in *Proceedings of the 3rd International Symposium on Filamentation (COFIL 2010), Iraklion, Greece, May 31–June 5, 2010*, p. 73.
56. D. J. Mitchell, A. W. Snyder, and L. Poladian, *Phys. Rev. Lett.* **77**, 271 (1996).
57. V. Tikhonenko, J. Christou, and B. Luther-Davies, *Phys. Rev. Lett.* **76**, 2698 (1996).
58. M.-F. Shih, M. Segev, and G. Salamo, *Phys. Rev. Lett.* **78**, 2551 (1997).
59. W. Krolikowski and S. Holmstrom, *Opt. Lett.* **22**, 369 (1997).
60. G. I. Stegeman and M. Segev, *Science* **286**, 1518 (1999).
61. A. C. Bernstein, M. McCormick, G. M. Dyer, J. C. Sanders, and T. Ditmire, *Phys. Rev. Lett.* **102**, 123902 (2009).
62. Y. Liu, M. Durand, S. Chen, A. Houard, B. Prade, B. Forestier, and A. Mysyrowicz, *Phys. Rev. Lett.* **105**, 055003 (2010).
63. X. Yang, J. Wu, Y. Peng, S. Yuan, and H. Zeng, in *Proceedings of the CLEO* (2008), paper CTuE6; X. Yang, J. Wu, Y. Peng, Y. Tong, P. Lu, L. Ding, Z. Xu, and H. Zeng, *Opt. Lett.* **34**, 3806 (2009).
64. X. Yang, J. Wu, Y. Peng, Y. Tong, S. Yuan, L. Ding, Z. Xu, and H. Zeng, *Appl. Phys. Lett.* **95**, 111103 (2009).
65. T. Xi, X. Lu, and J. Zhang, *Opt. Commun.* **282**, 3140 (2009).
66. N. Aközbek, A. Iwasaki, A. Becker, M. Scalora, S. L. Chin, and C. M. Bowden, *Phys. Rev. Lett.* **89**, 143901 (2002).
67. R. A. Ganeev, H. Singhal, P. A. Naik, J. A. Chakera, M. Kumar, and P. D. Gupta, *Phys. Rev. A* **82**, 043812 (2010).
68. P. Rohwetter, M. Queisser, K. Stelmasczyk, M. Fechner, and L. Woste, *Phys. Rev. A* **77**, 013812 (2008).
69. H. Stapelfeldt and T. Seideman, *Rev. Mod. Phys.* **75**, 543 (2003).
70. H. Cai, J. Wu, P. Lu, X. Bai, L. Ding, and H. Zeng, *Phys. Rev. A* **80**, 051802(R) (2009).
71. P. Béjot, Y. Petit, L. Bonacina, J. Kasparian, M. Morétand, and J.-P. Wolf, *Opt. Express* **16**, 7564 (2008).
72. J. Wu, H. Cai, P. Lu, X. Bai, L. Ding, and H. Zeng, *Appl. Phys. Lett.* **95**, 221502 (2009).
73. J. Wu, Y. Tong, X. Yang, H. Cai, P. Lu, H. Pan, and H. Zeng, *Opt. Lett.* **34**, 3211 (2009).
74. T. Xi, X. Lu, and J. Zhang, *Phys. Rev. Lett.* **96**, 025003 (2006).
75. B. Shim, S. E. Schrauth, C. J. Hensley, L. T. Vuong, P. Hui, A. A. Ishaaya, and A. L. Gaeta, *Phys. Rev. A* **81**, 061803(R) (2010).
76. J. Wu, H. Cai, Y. Peng, Y. Tong, A. Couairon, and H. Zeng, *Laser Phys.* **19**, 1759 (2009).
77. H. Cai, J. Wu, P. Lu, Y. Tong, X. Yang, X. Bai, H. Pan, H. Li, and H. Zeng, *Sci. China: Phys. Mech. Astron.* **53**, 1036 (2010).
78. R. Boyd, *Nonlinear Optics*, 2nd ed. (Academic, New York, 2003).
79. V. Renard, O. Faucher, and B. Lavorel, *Opt. Lett.* **30**, 70 (2005).
80. H. Cai, J. Wu, A. Couairon, and H. Zeng, *Opt. Lett.* **34**, 827 (2009).
81. J. Wu, H. Cai, Y. Tong, and H. Zeng, *Opt. Express* **17**, 16300 (2009).
82. J. Wu, H. Cai, A. Couairon, and H. Zeng, *Phys. Rev. A* **79**, 063812 (2009).
83. F. Calegari, C. Vozzi, S. Gasilov, E. Benedetti, G. Sansone, M. Nisoli, S. De Silvestri, and S. Stagira, *Phys. Rev. Lett.* **100**, 123006 (2008).
84. S. Varma, Y.-H. Chen, and H. M. Milchberg, *Phys. Rev. Lett.* **101**, 205001 (2008).
85. J. Itatani, J. Levesque, D. Zeidler, H. Niikura, H. Pépin, J. Kieffer, P. B. Corkum, and D. Villeneuve, *Nature* **432**, 867 (2004).
86. R. Bartels, T. Weinacht, N. Wagner, M. Baertschy, C. Greene, M. Murnane, and H. Kapteyn, *Phys. Rev. Lett.* **88**, 013903 (2002).
87. J. Wu, H. Cai, H. Zeng, and A. Couairon, *Opt. Lett.* **33**, 2593 (2008).
88. J. Wu, H. Cai, A. Couairon, and H. Zeng, *Phys. Rev. A* **80**, 013828 (2009).
89. T. Kanai, S. Minemoto, and H. Sakai, *Nature* **435**, 470 (2005).
90. J. Wu, H. Qi, and H. Zeng, *Phys. Rev. A* **77**, 053412 (2008).
91. Y. Chen, C. Marceau, F. Théberge, M. Châteauneuf, J. Dubois, and S. L. Chin, *Opt. Lett.* **33**, 2731 (2008).
92. D. Faccio, A. Averchi, A. Lotti, P. D. Trapani, A. Couairon, D. Papazoglou, and S. Tzortzakis, *Opt. Express* **16**, 1565 (2008).
93. H. Zeng, J. Wu, H. Xu, K. Wu, and E. Wu, *Phys. Rev. Lett.* **92**, 143903 (2004); H. Zeng, K. Wu, H. Xu, and J. Wu, *Appl. Phys. Lett.* **87**, 061102 (2005); H. Zeng, J. Wu, H. Xu, and K. Wu, *Phys. Rev. Lett.* **96**, 083902 (2006).
94. H. Xu and H. Zeng, *Opt. Lett.* **32**, 1944 (2007); H. Xu and H. Zeng, *Opt. Lett.* **32**, 820 (2007); W. Lei, J. Wu, H. Cai, and H. Zeng, *Opt. Lett.* **34**, 166 (2009).

95. X. Yang, J. Wu, Y. Tong, L. Ding, Z. Xu, and H. Zeng, *Appl. Phys. Lett.* **97**, 071108 (2010).
96. F. Théberge, N. Aközbek, W. Liu, J. Filion, and S. L. Chin, *Opt. Commun.* **276**, 298 (2007).
97. X. Yang, J. Wu, Y. Peng, Y. Tong, S. Yuan, L. Ding, Z. Xu, and H. Zeng, *Appl. Phys. Lett.* **95**, 111103 (2009).
98. J. Yu, D. Mondelain, G. Ange, R. Volk, S. Niedermeier, J. P. Wolf, J. Kasparian, and R. Sauerbrey, *Opt. Lett.* **26**, 533 (2001).
99. H. Cai, J. Wu, Y. Peng, and H. Zeng, *Opt. Express* **17**, 5822 (2009).
100. J. Wu, H. Cai, Y. Peng, and H. Zeng, *Phys. Rev. A* **79**, 041404(R) (2009).
101. F. A. Ilkov, L. Sh. Ilkova, and S. L. Chin, *Opt. Lett.* **18**, 681 (1993).
102. H. Cai, J. Wu, X. Bai, H. Pan, and H. Zeng, *Opt. Lett.* **35**, 49 (2010).
103. J. Wu, H. Zeng, and C. Guo, *Phys. Rev. A* **75**, 043402 (2007).
104. H. Cai, J. Wu, H. Li, X. Bai, and H. Zeng, *Opt. Express* **17**, 21060 (2009).
105. Y. Wang, X. Dai, J. Wu, L. Ding, and H. Zeng, *Appl. Phys. Lett.* **96**, 031105 (2010).
106. S. L. Chin, F. Théberge, and W. Liu, *Appl. Phys. B* **86**, 477 (2007).
107. F. Théberge, Q. Luo, W. Liu, S. A. Hosseini, M. Sharifi, and S. L. Chin, *Appl. Phys. Lett.* **87**, 081108 (2005).
108. L. Berge, S. Skupin, G. Mejean, J. Kasparian, J. Yu, S. Frey, E. Salmon, and J. P. Wolf, *Phys. Rev. E* **71**, 016602 (2005).
109. F. Théberge and S. L. Chin, Patent US No. 7729044 B2 (2010).
110. T. Fuji, T. Horio, and T. Suzuki, *Opt. Lett.* **32**, 2481 (2007).
111. T. Fuji, T. Suzuki, E. E. Serebryannikov, and A. Zheltikov, *Phys. Rev. A* **80**, 063822 (2009).
112. F. Théberge, M. Châteauneuf, V. Ross, P. Mathieu, and J. Dubois, *Opt. Lett.* **33**, 2515 (2008).
113. F. Théberge, M. Châteauneuf, G. Roy, P. Mathieu, and J. Dubois, *Phys. Rev. A* **81**, 033821 (2010).
114. Y. Chen, F. Théberge, C. Marceau, H. Xu, N. Aközbek, O. Kosareva, and S. L. Chin, *Appl. Phys. B* **91**, 219 (2008).
115. F. M. Mitschke and L. F. Mollenauer, *Opt. Lett.* **11**, 659 (1986).
116. J. P. Gordon, *Opt. Lett.* **11**, 662 (1986).
117. X. Liu, C. Xu, W. H. Knox, J. K. Chandalia, B. J. Eggleton, S. G. Kosinski, and R. S. Windeler, *Opt. Lett.* **26**, 358 (2001).
118. G. P. Agrawal, *Nonlinear Fiber Optics* (Academic, San Diego, CA, 2001).
119. D. Faccio, A. Averchi, A. Couairon, M. Kolesik, J. V. Moloney, A. Dubietis, G. Tamosauskas, P. Polesana, A. Piskarskas, and P. Di Trapani, *Opt. Express* **15**, 13077 (2007).
120. H. Hamster, A. Sullivan, S. Gordon, W. White, and R. W. Falcone, *Phys. Rev. Lett.* **71**, 2725 (1993).
121. H. Hamster, A. Sullivan, S. Gordon, and R. W. Falcone, *Phys. Rev. E* **49**, 671 (1994).
122. T. Löffler, F. Jacob, and H. G. Roskos, *Appl. Phys. Lett.* **77**, 453 (2000).
123. T. Löffler and H. G. Roskos, *J. Appl. Phys.* **91**, 2611 (2002).
124. D. J. Cook and R. M. Hochstrasser, *Opt. Lett.* **25**, 1210 (2000).
125. M. Kress, T. Löffler, S. Eden, M. Thomson, and H. G. Roskos, *Opt. Lett.* **29**, 1120 (2004).
126. T. Bartel, P. Gaal, K. Reimann, M. Woerner, and T. Elsaesser, *Opt. Lett.* **30**, 2805 (2005).
127. X. Xie, J.-M. Dai, and X.-C. Zhang, *Phys. Rev. Lett.* **96**, 075005 (2006).
128. M. D. Thomson, M. Kreß, T. Löffler, and H. G. Roskos, *Laser Photon. Rev.* **1**, 349 (2007).
129. J. Dai, X. Xie, and X.-C. Zhang, *Appl. Phys. Lett.* **91**, 211102 (2007).
130. M.-K. Chen, J. H. Kirn, C.-E. Yang, S. S. Yin, R. Hui, and P. Ruffin, *Appl. Phys. Lett.* **93**, 231102 (2008).
131. A. Houard, Y. Liu, B. Prade, and A. Mysyrowicz, *Opt. Lett.* **33**, 1195 (2008).
132. Y. Zhang, Y. Chen, S. Xu, H. Lian, M. Wang, W. Liu, S. L. Chin, and G. Mu, *Opt. Lett.* **34**, 2841 (2009).
133. D. Dietze, J. Darmo, S. Roither, A. Pugzlys, J. N. Heyman, and K. Unterrainer, *J. Opt. Soc. Am. B* **26**, 2016 (2009).
134. K. Y. Kim, J. H. Glowonia, A. J. Taylor, and G. Rodriguez, *Opt. Express* **15**, 4577 (2007).
135. K. Y. Kim, A. J. Taylor, J. H. Glowonia, and G. Rodriguez, *Nature Photon.* **2**, 605 (2008).
136. X.-Y. Peng, C. Li, M. Chen, T. Toncian, R. Jung, O. Willi, Y.-T. Li, W.-M. Wang, S.-J. Wang, F. Liu, A. Pukhov, Z.-M. Sheng, and J. Zhang, *Appl. Phys. Lett.* **94**, 101502 (2009).
137. N. Kaipowicz and X.-C. Zhang, *Phys. Rev. Lett.* **102**, 093001 (2009).
138. J. Dai, N. Karpowicz, and X.-C. Zhang, *Phys. Rev. Lett.* **103**, 023001 (2009).
139. H. Wen and A. M. Lindenberg, *Phys. Rev. Lett.* **103**, 023902 (2009).
140. F. Blanchard, G. Sharma, X. Ropagnol, L. Razzari, R. Morandotti, and T. Ozaki, *Opt. Express* **17**, 6044 (2009).
141. J.-M. Manceau, A. Averchi, F. Bonaretti, D. Faccio, P. Di Trapani, A. Couairon, and S. Tzortzakis, *Opt. Lett.* **34**, 2165 (2009).
142. C. D'Amico, A. Houard, M. Franco, B. Prade, A. Mysyrowicz, A. Couairon, and V. T. Tikhonchuk, *Phys. Rev. Lett.* **98**, 235002 (2007).
143. Y. Chen, C. Marceau, W. Liu, Z.-D. Sun, Y. Zhang, F. Théberge, M. Châteauneuf, J. Dubois, and S. L. Chin, *Appl. Phys. Lett.* **93**, 231116 (2008).
144. Y. Zhang, Y. Chen, C. Marceau, W. Liu, Z.-D. Sun, S. Xu, F. Théberge, M. Châteauneuf, J. Dubois, and S. L. Chin, *Opt. Express* **16**, 15483 (2008).
145. A. Houard, Y. Liu, B. Prade, V. T. Tikhonchuk, and A. Mysyrowicz, *Phys. Rev. Lett.* **100**, 255006 (2008).

146. Y. Chen, T.-J. Wang, C. Marceau, F. Théberge, M. Châteauneuf, J. Dubois, O. Kosareva, and S. L. Chin, *Appl. Phys. Lett.* **95**, 101101 (2009).
147. Y. Liu, A. Houard, B. Prade, A. Mysyrowicz, A. Diaw, and V. T. Tikhonchuk, *Appl. Phys. Lett.* **93**, 051108 (2008).
148. Y. Liu, A. Houard, B. Prade, S. Akturk, A. Mysyrowicz, and V. T. Tikhonchuk, *Phys. Rev. Lett.* **99**, 135002 (2007).
149. T.-J. Wang, Y. Chen, C. Marceau, F. Théberge, M. Châteauneuf, J. Dubois, and S. L. Chin, *Appl. Phys. Lett.* **95**, 131108 (2009).
150. W. Liu, F. Théberge, J.-F. Daigle, P. T. Simard, S. M. Sarifi, Y. Kamali, H. L. Xu, and S. L. Chin, *Appl. Phys. B* **85**, 55 (2006).
151. J.-M. Manceau, M. Massauti, and S. Tzortzakis, *Opt. Exp.* **18**, 18894 (2010).
152. T.-J. Wang, C. Marceau, Y. Chen, S. Yuan, F. Théberge, M. Châteauneuf, J. Dubois, and S. L. Chin, *Appl. Phys. Lett.* **96**, 211113 (2010).
153. M. Durand, Y. Liu, A. Houard, and A. Mysyrowicz, *Opt. Lett.* **35**, 1710 (2010).
154. J. Wu, Y. Tong, M. Li, H. Pan, and H. Zeng, *Phys. Rev. A* **82**, 053416 (2010).
155. T.-J. Wang, S. Yuan, Z.-D. Sun, C. Marceau, Y. Chen, F. Théberge, M. Châteauneuf, J. Dubois, and S. L. Chin, *Laser Phys. Lett.* **8**, 295 (2011).
156. J. M. Dai, X. F. Lu, J. Liu, I. C. Ho, N. Karpowicz, and X.-C. Zhang, *THz Sci. Technol.* **2**, 131 (2009).
157. T.-J. Wang, S. Yuan, Y. Chen, J.-F. Daigle, C. Marceau, F. Théberge, M. Châteauneuf, J. Dubois, and S. L. Chin, *Appl. Phys. Lett.* **97**, 111108 (2010).
158. T.-J. Wang, J.-F. Daigle, Y. Chen, C. Marceau, F. Théberge, M. Châteauneuf, J. Dubois, and S. L. Chin, *Laser Phys. Lett.* **7**, 517 (2010).
159. T.-J. Wang, C. Marceau, S. Yuan, Y. Chen, Q. Wang, F. Théberge, M. Châteauneuf, J. Dubois, and S. L. Chin, *Laser Phys. Lett.* **8**, 57 (2011).
160. J. Liu and X.-C. Zhang, *Phys. Rev. Lett.* **103**, 235002 (2009); *IEEE J. Sel. Top. Quantum Electron.* **17**, 229 (2011).
161. J. Liu, J. Dai, S. L. Chin, and X.-C. Zhang, *Nature Photon.* **4**, 627 (2010).
162. C. Marceau, Y. Chen, F. Théberge, M. Châteauneuf, J. Dubois, and S. L. Chin, *Opt. Lett.* **34**, 1417 (2009).
163. S. Yuan, T.-J. Wang, O. Kosareva, N. Panov, V. A. Makarov, H. Zeng, and S. L. Chin, in preparation (2011).
164. O. Kosareva, N. Panov, V. Makarov, I. Perezhogin, C. Marceau, Y. Chen, S. Yuan, T.-J. Wang, H. Zeng, A. Savel'ev, and S. L. Chin, *Opt. Lett.* **35**, 2904 (2010).
165. C. Marceau, S. Ramakrishna, S. Génier, T.-J. Wang, Y. Chen, F. Théberge, M. Châteauneuf, J. Dubois, T. Seideman, and S. L. Chin, *Opt. Commun.* **283**, 2732 (2010).
166. A. Azarm, S. Ramakrishna, A. Talebpour, S. Hosseini, Y. Teranishi, H. L. Xu, Y. Kamali, J. Bernhardt, S. H. Lin, T. Seideman, and S. L. Chin, *J. Phys. B* **43**, 235602 (2010).
167. T. Seideman, *J. Chem. Phys.* **103**, 7887 (1995).
168. T. Seideman, *Phys. Rev. Lett.* **83**, 4971 (1999).
169. T. Seideman, *J. Chem. Phys.* **115**, 5965 (2001).
170. C. M. Dion, A. Keller, O. Atabek, and A. D. Bandrauk, *Phys. Rev. A* **59**, 1382 (1999).
171. B. Friedrich and D. Herschbach, *Phys. Rev. Lett.* **74**, 4623 (1995).
172. B. A. Zon and B. G. Katsnel'son, *Sov. Phys. JETP* **42**, 595 (1976).
173. H. Loesch and J. Moller, *Faraday Discuss.* **113**, 241 (1999).
174. P. A. Block, E. J. Bohac, and R. E. Miller, *Phys. Rev. Lett.* **68**, 1303 (1992).
175. F. Rosca-Pruna and M. J. J. Vrakking, *Phys. Rev. Lett.* **87**, 153902 (2001).
176. C. Leichtle, I. S. Averbukh, and W. P. Schleich, *Phys. Rev. A* **54**, 5299 (1996).
177. Z.-C. Yan and T. Seideman, *J. Chem. Phys.* **111**, 4113 (1999).
178. T. Seideman, *Phys. Rev. A* **56**, R17 (1997).
179. J. G. Underwood, M. Spanner, M. Y. Ivanov, J. Motterhead, B. J. Sussman, and A. Stolow, *Phys. Rev. Lett.* **90**, 223001 (2003).
180. T. P. Rakitzis, A. J. van den Brom, and M. H. M. Janssen, *Science* **303**, 1852 (2004).
181. V. Aquilanti, M. Bartolomei, F. Pirani, D. Cappelletti, Vecchiocattivi, Y. Shimizu, and T. Ka-sai, *Phys. Chem. Chem. Phys.* **7**, 291 (2005).
182. B. Friedrich and D. Herschbach, *J. Phys. Chem. A* **103**, 10280 (1999).
183. T. Kanai and H. Sakai, *J. Chem. Phys.* **115**, 5492 (2001).
184. R. Baumfalk, N. H. Nahler, and U. Buck, *J. Chem. Phys.* **114**, 4755 (2001).
185. H. Ohmura and T. Nakanaga, *J. Chem. Phys.* **120**, 5176 (2004).
186. H. Sakai, S. Minemoto, H. Nanjo, H. Tanji, and T. Suzuki, *Phys. Rev. Lett.* **90**, 083001 (2003).
187. H. Sakai, S. Minemoto, H. Nanjo, H. Tanji, and T. Suzuki, *Eur. Phys. J. D* **26**, 33 (2003).
188. A. Matos-Abiague and J. Berakdar, *Phys. Rev. A* **68**, 063411 (2003).
189. A. Matos-Abiague and J. Berakdar, *Chem. Phys. Lett.* **382**, 475 (2003).
190. D. Sugny, A. Keller, O. Atabek, D. Daems, C. M. Dion, S. Guérin, and H. R. Jauslin, *Phys. Rev. A* **69**, 033402 (2004).
191. D. Sugny, A. Keller, O. Atabek, D. Daems, S. Guérin, and H. R. Jauslin, *Phys. Rev. A* **69**, 043407 (2004).
192. M. Spanner, E. A. Shapiro, and M. Ivanov, *Phys. Rev. Lett.* **92**, 093001 (2004).
193. C. M. Dion, A. D. Bandrauk, O. Atabek, A. Keller, H. Umeda, and Y. Fujimura, *Chem. Phys. Lett.* **302**, 215 (1999).
194. S. Guérin, L. P. Yatsenko, H. R. Jauslin, O. Faucher, and B. Lavorel, *Phys. Rev. Lett.* **88**, 233601 (2002).
195. O. Atabek, C. M. Dion, and A. B. H. Yedder, *J. Phys. B: At. Mol. Opt. Phys.* **36**, 4667 (2003).
196. S. Ramakrishna and T. Seideman, *Phys. Rev. Lett.* **95**, 113001 (2005).

197. J. Ohkubo, T. Kato, H. Kono, and Y. Fujimura, *J. Chem. Phys.* **120**, 9123 (2004).
198. S. Ramakrishna and T. Seideman, *Phys. Rev. Lett.* **99**, 103001 (2007).
199. V. Renard, M. Renard, S. Guérin, Y. T. Pashayan, B. Lavorel, O. Faucher, and H. R. Jauslin, *Phys. Rev. Lett.* **90**, 153601 (2003).
200. T. Seideman and E. Hamilton, *Ad. At. Mol. Opt. Phys.* **52**, 289 (2006).
201. S. De, I. Znakovskaya, D. Ray, F. Anis, N. G. Johnson, I. A. Bocharova, M. Magrakvelidze, B. D. Esry, C. L. Cocke, I. V. Litvinyuk, and M. F. Kling, *Phys. Rev. Lett.* **103**, 153002 (2009).
202. A. Hishikawa, H. Hasegawa, and K. Yamanouchi, *Phys. Scripta T* **110**, 108 (2004).
203. T. Okino, Y. Furukawa, P. Liu, T. Ichikawa, R. Itakura, K. Hoshina, K. Yamanouchi, and H. Nakano, *Chem. Phys. Lett.* **423**, 220 (2006).
204. H. Hasegawa, A. Hishikawa, and K. Yamanouchi, *Chem. Phys. Lett.* **349**, 57 (2001).
205. F. Légaré, K. F. Lee, I. V. Litvinyuk, P. W. Dooley, A. D. Bandrauk, D. M. Villeneuve, and P. B. Corkum, *Phys. Rev. A* **72**, 052717 (2005).
206. J. Gagnon, K. F. Lee, D. M. Rayner, P. B. Corkum, and V. R. Bhardwaj, *J. Phys. B.: At. Mol. Opt. Phys.* **41**, 215104 (2008).
207. R. Dörner, V. Mergel, O. Jagutzki, L. Spielberger, J. Ullrich, R. Moshhammer, and H. Schmidt-Böcking, *Phys. Rep.* **330**, 95 (2000).
208. E. Gagnon, A. S. Sandhu, A. Paul, K. Hagen, A. Czausch, T. Jahnke, P. Ranitovic, C. L. Cocke, B. Walker, M. M. Murnane, and H. C. Kapteyn, *Rev. Sci. Instrum.* **79**, 063102 (2008).
209. Y.-H. Chen, S. Varma, I. Alexeev, and H. M. Milchberg, *Opt. Express* **15**, 7458 (2007).
210. Y.-H. Chen, S. Varma, and H. M. Milchberg, *J. Opt. Soc. Am. B* **25**, B122 (2008).
211. V. Renard, M. Renard, A. Rouzée, S. Guérin, H. R. Jauslin, B. Lavorel, and O. Faucher, *Phys. Rev. A* **70**, 033420 (2004).
212. F. Calegari, C. Vozzi, and S. Stagira, *Phys. Rev. A* **79**, 023827 (2009).
213. J.-F. Ripoche, G. Grillon, B. Prade, M. France, E. Nibbering, R. Lange, and A. Mysyrowicz, *Opt. Commun.* **135**, 310 (1997).
214. P. Reckenthaeler, M. Centurion, W. F. F. S. A. Trushin, F. Krausz, and E. E. Fill, *Phys. Rev. Lett.* **102**, 213001 (2009).
215. R. Velotta, N. Hay, M. B. Mason, M. Castillejo, and J. P. Marangos, *Phys. Rev. Lett.* **87**, 183901 (2001).
216. Y. Mairesse, D. Zeidler, N. Dudovich, M. Spanner, J. Levesque, D. M. Villeneuve, and P. B. Corkum, *Phys. Rev. Lett.* **100**, 143903 (2008).
217. Y. Mairesse, J. Levesque, N. Dudovich, P. B. Corkum, and D. M. Villeneuve, *J. Mod. Opt.* **55**, 2591 (2008).
218. B. K. McFarland, J. P. Farrell, P. H. Bucksbaum, and M. Gühr, *Science* **322**, 1232 (2008).
219. N. Kajumba, R. Torres, J. G. Underwood, J. S. Robinson, S. Baker, J. W. G. Tisch, R. de Nalda, W. A. Bryan, R. Velotta, C. Altucci, I. Procino, I. C. E. Turcu, and J. P. Marangos, *New J. Phys.* **10**, 025008 (2008).
220. S. Ramakrishna and T. Seideman, *Phys. Rev. Lett.* **99**, 113901 (2007).
221. A. Talebpoor, M. Abdel-Fattah, A. D. Bandrauk, and S. L. Chin, *Laser Phys.* **11**, 68 (2001).
222. M. V. Fedorov and A. M. Movsesian, *J. Phys. B: At. Mol. Opt. Phys.* **21**, L155 (1988).
223. M. V. Fedorov, in *Progress Inultrafast Intense Laser Science*, Ed. by K. Yamanouchi, P. Agostini, L. Chin, and G. Farante, Vol. 1 (Springer, Berlin, 2006), pp. 1–18.
224. I. V. Litvinyuk, K. F. Lee, P. W. Dooley, D. M. Rayner, D. M. Villeuneuve, and P. B. Corkum, *Phys. Rev. Lett.* **90**, 233003 (2003).
225. S. L. Chin, H. L. Xu, Q. Luo, F. Théberge, W. Liu, J. F. Daigle, Y. Kamali, P. T. Simard, J. Bernhardt, S. A. Hosseini, M. Sharifi, G. Méjean, A. Azarm, C. Marceau, O. Kosareva, V. P. Kandidov, N. Aközbek, A. Becker, G. Roy, P. Mathieu, J. R. Simard, M. Châteauneuf, and J. Dubois, *Appl. Phys. B* **95**, 1 (2009).
226. S. L. Chin and K. Miyazaki, *Jpn. J. Appl. Phys.* **38**, 2011 (1999).
227. X. M. Zhao, J.-C. Diel, C. Y. Wang, and J. M. Elizondo, *IEEE J. Quantum. Electron.* **31**, 599 (1995).
228. S. Tzortzakis, B. Prade, M. Franco, A. Mysyrowicz, S. Hüller, and P. Mora, *Phys. Rev. E* **64**, 57401 (2001).
229. B. L. Fontaine, F. Vidal, D. Comtois, C.-Y. Chien, A. Desparois, T. W. Johnston, J.-C. Keffer, H. P. Mercure, H. Pépin, and F. A. M. Rizk, *IEEE Trans. Plasma Sci.* **27**, 688 (1999).
230. F. Vidal, D. Comtois, C. Y. Chien, A. Desparois, B. La Fontaine, T. W. Johnston, J. C. Kieffer, H. Mercure, H. Pépin, and F. A. Rizk, *IEEE Trans. Plasma Sci.* **28**, 418 (2000).
231. H. Pépin, D. Comtois, F. Vidal, C. Y. Chien, A. Desparois, T. W. Johnston, J. C. Kieffer, B. La Fontaine, F. Martin, F. A. M. Rizk, C. Potvin, P. Couture, H. P. Mercure, A. Bondiou-Clergerie, P. Lalande, and I. Gallimberti, *Phys. Plasma* **8**, 2532 (2001).
232. D. Comtois, H. Pépin, F. Vidal, F. A. M. Rizk, C. Y. Chien, T. Y. Johnston, J.-C. Kieffer, B. La Fontaine, F. Martin, C. Potvin, P. Couture, H. P. Mercure, A. Bondiou-Clergerie, P. Lalande, and Ivo Gallimberti, *IEEE Trans. Plasma Sci.* **31**, 377 (2003); *IEEE Trans. Plasma Sci.* **31**, 387 (2003).
233. T. Fujii, M. Miki, N. Goto, A. Zhidkov, T. Fukuchi, Y. Oishi, and K. Nemoto, *Phys. Plasma* **15**, 013107 (2008).
234. T. Fujii, N. Goto, M. Miki, T. Nayuki, T. Shindo, and K. Nemoto, *Trans. Inst. Electr. Eng. Jpn. A* **125**, 765 (2005).
235. N. Goto, M. Miki, T. Fujii, T. Nayuki, T. Sekiya, T. Shindo, and K. Nemoto, *Trans. Inst. Electr. Eng. Jpn. A* **125**, 1059 (2005).
236. M. Rodriguez, R. Sauerbrey, H. Wille, L. Wöste, T. Fuji, Y.-B. Andr, A. Mysyrowicz, L. Klingbeil, K. Rethmeier, W. Kalkner, J. Kasparian, E. Salmon, J. Yu, and J.-P. Wolf, *Opt. Lett.* **27**, 772 (2002).

237. D. F. Gordon, A. Ting, R. F. Hubbard, E. Briscoe, C. Manka, S. P. Slinker, A. P. Baronavski, H. D. Ladouceur, P. W. Grounds, and P. G. Girardi, *Phys. Plasma* **10**, 4530 (2003).
238. K. Sugiyama, T. Fujii, M. Miki, M. Yamaguchi, A. Zhidkov, E. Hotta, and K. Nemoto, *Opt. Lett.* **34**, 2964 (2009).
239. K. Sugiyama, T. Fujii, M. Miki, A. Zhidkov, M. Yamaguchi, E. Hotta, and K. Nemoto, *Phys. Plasma* **17**, 043108 (2010).
240. R. Ackermann, A. K. Stelmaszczyk, P. Rohwetter, G. Mejean, E. Salmon, J. Yu, J. Kasparian, G. Méchain, V. Bergmann, S. Schaper, B. Weise, T. Kumm, K. Rethmeier, and W. Kalkner, L. Woeste, and J. P. Wolf, *Appl. Phys. Lett.* **85**, 5781 (2004).
241. J. Kasparian, R. Ackermann, Y.-B. André, G. Méchain, G. Méjean, B. Prade, P. Rohwetter, E. Salmon, K. Stelmaszczyk, J. Yu, A. Mysyrowicz, R. Sauerbrey, L. Woeste, and J.-P. Wolf, *Opt. Express* **16**, 5757 (2008).
242. J. Kasparian, L. Woeste, and J. P. Wolf, *OPN Opti. Photon. News* **21**, 22 (July/Aug., 2010).
243. S. L. Chin, US Patent No. 7184143 B2 (2007).
244. Y. Kamali, Q. Sun, J.-F. Daigle, A. Azarm, J. Bernhardt, and S. L. Chin, *Opt. Commun.* **282**, 950 (2009).
245. R. M. Measures, *Laser Remote Sensing, Fundamentals and Applications* (Krieger, Malabar, Florida, 1992).
246. J.-F. Daigle, Y. Kamali, G. Roy, and S. L. Chin, *Appl. Phys. B* **93**, 759 (2008).
247. J.-F. Daigle, G. Méjean, W. Liu, F. Théberge, H. L. Xu, Y. Kamali, J. Bernhardt, A. Azarm, Q. Sun, P. Mathieu, G. Roy, J.-R. Simard, and S. L. Chin, *Appl. Phys. B* **87**, 749 (2007).
248. F. Kong, Q. Luo, H. L. Xu, M. Sharifi, D. Song, and S. L. Chin, *J. Chem. Phys.* **125**, 133320 (2006).
249. F. Kong, and S. L. Chin, in *Progress in Ultrafast Intense Laser Science III*, Ed. by K. Yamanouchi, S. L. Chin, P. Agostini, and G. Ferrante (Springer, Berlin, 2008), vol. 3, Ch. 6, p. 113.
250. A. Azarm, H. L. Xu, Y. Kamali, J. Bernhardt, D. Song, A. Xia, Y. Teranishi, S. H. Lin, F. Kong, and S. L. Chin, *J. Phys. B* **41**, 225601 (2008).
251. D. Song, A. Azarm, Y. Kamali, K. Liu, A. Xia, Y. Teranishi, S. Lin, F. Kong, and S. L. Chin, *J. Phys. Chem. A* **114**, 3087 (2010).
252. Y. Hatano, *Radiat. Environ. Biophys.* **38**, 239 (1999).
253. Y. Hatano, *Phys. Rep.* **313**, 109 (1999).
254. M. Plewicky and R. J. Levis, *J. Opt. Soc. Am. B* **25**, 1714 (2008).
255. G. Heck, E. J. Judge, J. Odnher, M. Plewicky, and R. J. Levis, in *Remote Sensing via Femtosecond Filament Based Technologies, Proceedings of the 43th Annual GomaticTech Conference, Orlando, FL, USA, 16–19 March 2009*, session 22-Laser sensing.
256. J. H. Odnher, D. A. Romanov, and R. J. Levis, *SPIE Photon. West Conf.* **758**, 75820M (2010).
257. J. H. Odnher, D. A. Romanov, and R. J. Levis, *Phys. Rev. Lett.* **103**, 075005 (2009).
258. E. J. Judge, G. Heck, E. Cerkez Bader, and R. J. Levis, *Anal. Chem.* **81**, 2658 (2009).
259. J. Kasparian, M. Rodriguez, G. Méjean, J. Yu, E. Salmon, H. Wille, R. Bourayou, S. Frey, Y.-B. André, A. Mysyrowicz, R. Sauerbrey, J.-P. Wolf, and L. Woeste, *Science* **301**, 61 (2003).
260. P. Rohwetter, J. Kasparian, K. Stelmaszczyk, Z. Hao, S. Henin, N. Lascoux, W. M. Nakaema, Y. Petit, M. Queiér, R. Salamé, E. Salmon, L. Woestel, and J.-P. Wolf, *Nature Photon.* **4**, 451 (2010).
261. M. Châteauneuf, S. Payeur, J. Dubois, and J.-C. Kieffer, *Appl. Phys. Lett.* **92**, 091104 (2008).
262. A. E. Dormidonov, V. V. Valuev, V. L. Dmitriev, S. A. Shlenov, and V. P. Kandidov, *Proc. SPIE* **6733**, 67332S (2007).
263. G. Méchain, A. Couairon, Y.-B. Andre, C. D'Amico, M. Franco, B. Prade, S. Tzortzakis, A. Mysyrowicz, and R. Sauerbrey, *Appl. Phys. B* **79**, 379 (2004).
264. S. L. Chin, Y. Chen, O. Kosareva, V. P. Kandidov, and F. Théberge, *Laser Phys.* **18**, 962 (2008).
265. J.-F. Daigle, O. Kosareva, N. Panov, T.-J. Wang, S. Hosseini, S. Yuan, G. Roy, and S. L. Chin, *Opt. Commun.* (2011, in press).
266. B. Prade, M. Franco, A. Mysyrowicz, A. Couairon, H. Buersing, B. Eberle, M. Krenz, D. Seiffer, and O. Vasseur, *Opt. Lett.* **31**, 2601 (2006).
267. A. E. Siegman, *Lasers* (Univ. Sci. Books, Mill Valley, CA, 1986).
268. Y. Chen, F. Théberge, O. Kosareva, N. Panov, V. P. Kandidov, and S. L. Chin, *Opt. Lett.* **32**, 3477 (2007).
269. V. Lorient, E. Hertz, O. Faucher, and B. Lavorel, *Opt. Express* **17**, 13429 (2009); *Opt. Express* **18**, 3011 (2010).
270. P. Béjot, J. Kasparian, S. Henin, V. Lorient, T. Vieillard, E. Hertz, O. Faucher, B. Lavorel, and J.-P. Wolf, *Phys. Rev. Lett.* **104**, 103903 (2010).
271. J.-F. Daigle, Y. Kamali, J. Bernhardt, W. Liu, C. Marceau, A. Azarm, and S. L. Chin, *Opt. Commun.* **281**, 3327 (2008).